O.K.

Scuola Internazionale Superiore di Studi Avanzati - Trieste

AGN Outflows and Galaxy Formation

Thesis submitted for the degree of
Doctor Philosophiæ

CANDIDATE:
Michele Cirasuolo

SUPERVISORS:
Prof. Luigi Danese
Dr. Manuela Magliocchetti
Prof. Annalisa Celotti

October 2004

SISSA – Via Beirut 2-4 – 34014 TRIESTE – ITALY

SISSA ISAS

SCUOLA INTERNAZIONALE SUPERIORE DI STUDI AVANZATI
INTERNATIONAL SCHOOL FOR ADVANCED STUDIES

AGN Outflows and Galaxy Formation

Thesis submitted for the degree of
Doctor Philosophiæ

CANDIDATE:
Michele Cirasuolo

SUPERVISORS:
Prof. Luigi Danese
Dr. Manuela Magliocchetti
Prof. Annalisa Celotti

October 2004

Table of Contents

Citations to Previously Published Works

Part of the contents of this Thesis has already appeared in the following papers:

Refereed Journals:

- *The radio-loud/radio-quiet dichotomy: news from the 2dF-QSO Survey.*
  Cirasuolo M., Magliocchetti M., Celotti A., Danese L., 2003, MNRAS, **341**, 993.
- *Is there a dichotomy in the radio-loudness distribution of quasars?.*
  Cirasuolo M., Celotti A., Magliocchetti M., Danese L., 2003, MNRAS, **346**, 447.
- *Faint radio loud quasars: clues on their evolution.*
  Cirasuolo M., Magliocchetti M., Celotti A., 2004, accepted for publication in MNRAS.

In Preparation:

- *Radio properties of the highest redshift quasar sample.*
  Cirasuolo M., Gentile G., Celotti A., Magliocchetti M., Danese L., Cristiani S.
- *A new physical Fundamental Plane for spheroidal galaxies.*
  Cirasuolo M., Shankar. F., Granato G.L., Danese L.

Chapter 1

Introduction

1.1 Overview

Black holes (BH) are one of the most spectacular and amazing phenomena in modern astrophysics. Their properties and those of the flows around them are thought to be of fundamental importance in many astronomical fields, as they are expected to power quasars, Active Galactic Nuclei (AGN), X-ray binaries etc. In recent years it is also becoming clear that they are an indispensable ingredient to be taken into account in the paradigm of galaxy formation and evolution. Therefore, AGN activity extends its "sphere of influence" from very small scales around the central black hole up to Mpc scales, with important effects on its own host galaxy as well as on the intra cluster medium.

In this thesis particular attention will be devoted to outflows generated by AGN activity, with emphasis given to relativistic jets. The other class of outflows, the so-called winds, will be discussed in connection with the phenomenon of galaxy formation, since they are thought to be the main source of AGN feedback. In this work we will therefore deal with a very broad dynamical scale, linking together galactic structures, as traced in the hierarchical scenario of Cold Dark Matter (CDM), to the collapse of the baryonic component forming stars and down to accretion processes around the central black hole. The aim of the present Introduction is then to establish a "leitmotiv" of the thesis, briefly describing the main physical processes involved and the motivations at the base of this work.

1.2 The Black Hole paradigm

Let us start this brief Introduction by describing the first observational evidences for the existence of black holes, the fundamental "seed" of all our discussion. In 1960, Allan Sandage discovered an odd-looking star-like object (a quasi-star, or *Quasar*) by observing the field of the radio galaxy 3C48 with a five meter optical telescope. Other similar objects were discovered immediately afterwards, but it was only three years later that a revolutionary explanation was found for their spectra: Maarten Schmidt realized that one of these sources, 3C273, was a very distant object, whose light and spectral lines were redshifted as a result of the expansion of the Universe. Since the very beginning, those extraordinary objects were believed to be powered by accretion onto super massive black holes (Salpeter 1964; Zeldovich & Novikov 1964). Indeed, quasars were known to be prodigiously powerful, with luminosities, equivalent to hundreds of galaxies, releasing an energy of 10^{60} erg, in a region smaller than a few light days. This energy was thought to be released by accreting matter onto a black hole in a way which could be over a hundred times more efficient than the known nuclear processes.

1.3 Accretion disks around black holes

In this Section we will briefly introduce the basic concepts of accretion onto a compact object, which, as already said, is the most efficient mechanism to power quasars and AGN activity in general. If the accreting material possesses angular momentum, gravitational contraction is halted by a centrifugal barrier, which forces the material to settle on a disk. It is such a disk that mediates the process of accretion: neighbouring annuli of differentially rotating matter experience a viscous shear that transports angular momentum outwards, allowing the material to slowly spiral in, towards the center of the potential.

Several different modes of accretion have been proposed depending on the rate of gas supply. A fundamental discriminant is the radiative efficiency of the flow, defined as the ratio of the output bolometric luminosity to the rest mass energy accretion rate:

$$\epsilon = \frac{L}{\dot{M}c^2}. \tag{1.1}$$

When radiative cooling is efficient, the maximal energy per unit mass available is uniquely determined by the binding energy at the innermost stable orbit, which in turn fixes the efficiency. A general relativistic treatment (Novikov & Thorne 1973) reveals that the quantity ϵ increases from 0.06, for a non-rotating hole, up to 0.42, for a maximally rotating Kerr black hole.

The standard radiatively efficient disk solution was originally proposed by Shakura & Sunyaev (1973). A full discussion of the many issues associated to the standard accretion disk is outside the aims of this work and can be found in e.g. Pringle (1981), Papaloizou & Lin (1995), Frank et al. (2002), Blaes (2002). Here we will just introduce the basic idea: under the assumptions of a geometrically thin (vertical scale-height H much smaller than the radial coordinate R: $H \ll R$) and optically thick disk, its structure is determined by solving the conservation equations (conservation of vertical momentum, mass, angular momentum and energy), once the equations of state of pressure and opacity are given. In order to allow the closure of the system of equations, we also need a viscosity law. Shakura & Sunyaev (1973) recognized the central importance of the viscosity factor and, in face of the theoretical uncertainties, proposed for the stress tensor, W, the famous "α-prescription":

$$W = \alpha_V \, c_s^2 \tag{1.2}$$

where c_s is the sound speed and $\alpha_V \lesssim 1$ is the viscosity parameter.

For radiatively efficient disks, the bolometric luminosity is characterized (and in general limited) by the so-called *Eddington luminosity*, $L_{\rm Edd}$. This quantity is the luminosity at which the radiative momentum from a spherically symmetric source is balanced by the gravitational force of the central object. As both the radiation flux and the Newtonian force diminish with the square of the distance, the Eddington luminosity only depends on the mass of the central BH and on some fundamental constants:

$$L_{\rm Edd} = \frac{4\pi G m_p M_{\rm BH} c}{\sigma_T} \simeq 1.3 \times 10^{38} \frac{M_{\rm BH}}{M_\odot} {\rm erg\ s^{-1}} \tag{1.3}$$

where m_p is the proton mass, c the speed of light, σ_T is the Thompson scattering cross section and $M_{\rm BH}$ is the mass of the central BH. This luminosity also identifies the Eddington accretion rate $\dot{M}_{\rm Edd}$, which is the mass accretion rate necessary to sustain the Eddington luminosity:

$$\dot{M}_{\rm Edd} = \frac{L_{\rm Edd}}{\epsilon c^2}. \tag{1.4}$$

This corresponds to a rate of $\sim 2.2 M_\odot$ yr^{-1} for a BH of $10^8 M_\odot$, assuming $\epsilon \simeq 0.1$.

On the other hand, when radiative cooling is negligible, accretion is adiabatic and $\epsilon \ll 1$. In an optically thin and geometrically thick accretion disk (Shapiro et al. 1976; Ichimaru 1977), the density may be so low that ions are unable to transfer energy to electrons at a high enough rate for the radiative electronic cooling to balance the viscous heating. Part of the energy is advected with the proton flow and swallowed by the central black hole. In this case the disk is likely to inflate as a consequence of its large internal energy. This kind of solution was named the "ion supported torus" by Rees et al. (1982), who also demonstrated that such a solution can be established only for low accretion rates ($\dot{M} \lesssim \alpha_V^2$). In recent years, much work has been devoted to a detailed study of such flows, renamed Advection Dominated Accretion Flows or *ADAF* (Narayan & Yi 1994, 1995; Abramowicz et al. 1995; Narayan et al. 1999). Adiabatic accretion may also be accompanied by outflows (Abramowicz et al. 2000; Narayan et al. 2000; Igumenshchev et al. 2000) which carry away energy, angular momentum and mass as in the *ADIOS* model proposed by Blandford & Begelman (1999).

Another mode of adiabatic accretion can occur when the gas is supplied at a rate far in excess of the Eddington rate ($\dot{M}/\dot{M}_{\rm Edd} > 1$), the so-called *slim disk* solution (Abramowicz et al 1988). In this case, photons will be trapped in the accreting gas and advected towards the hole faster than the rate at which they can diffuse away (Katz 1977; Begelman & Meier 1982; Beloborodov 1998). Again the flow is likely to be effectively adiabatic and is likely to drive an outflow as for low accretion rates (Meier 1982; Lipunova 1999).

1.4 The nature of outflows

Closely related to accretion mechanisms is the nature of the outflows generated by such processes. In fact accretion, at both high and low rates, can be accompanied by powerful outflows, that may or may not collimate. If they do, then they become jets and are likely able to propagate to large distances from their originating sources as it is observed in radio galaxies and quasars. If they do not, they show up as winds, which are likely to become subsonic and undergo a strong shock when their momentum flux falls to match the ambient pressure.

1.4.1 Winds

An interesting class of outflows are those observed in BAL (Broad Absorption Line) quasars. In fact, roughly 10% of optically selected AGN show these unusually broad P-Cygni-like absorption features in their optical and ultraviolet spectra. The kinetic power of the outflowing gas in these objects can be a significant fraction of the bolometric luminosity (Begelman 2003). X-ray observations of BAL quasars revealed significant absorption ($N_{\rm H} \gtrsim 10^{23}\,{\rm cm}^{-2}$), implying large outflows ($\dot{M}_{\rm out} \gtrsim 5\,M_{\odot}/{\rm yr}$) and large kinetic luminosities (Brandt et al. 2001; Brandt & Gallagher 2000).

It has been suggested that these absorption features arise in a flow of gas which rises vertically from a narrow range of radii in the accretion disk. It then bends forming a conical wind, which moves radially outwards with a divergence angle of $\sim 6°$, corresponding to a covering factor of 10%, which provides the observed fraction of BAL over the total quasar population (Elvis 2000). When the line of sight is along the flow, the full range of velocities is seen in absorption with a large column density, giving rise to the BAL phenomena.

Theoretical studies on the mechanisms responsible for AGN-driven outflows show that efficient acceleration could be due to radiation pressure through scattering and absorption by dust (see e.g. Voit et al. 1993) and scattering in resonance lines (see e.g. Arav, Li & Begelman 1994). Murray et al. (1995) presented a dynamical model for a wind produced just over the disk by a combination of radiation and gas pressure. In a similar way Proga, Stone & Kallman (2000) showed that a wind can be launched from a disk around a $10^8\,M_{\odot}$ black hole with velocities up to 0.1c and mass-loss rate of $0.5\,M_{\odot}\,{\rm yr}^{-1}$. According to Murray et al. (1995), an approximate solution for the wind velocity produced by line acceleration as a function of the radius is:

$$v = v_{\infty}\left(1 - \frac{r_f}{r}\right)^{2.35} \tag{1.5}$$

where r_f is the radius at which the wind is launched. The asymptotic speed as a function of the Eddington luminosity is:

$$\frac{v_\infty}{c} \sim 6.2 \times 10^{-2} \left(\frac{r_f}{10^{16}\,\mathrm{cm}}\right)^{-1/2} \left(\frac{L_{\mathrm{Edd}}}{10^{46}\mathrm{erg\,s^{-1}}}\right)^{1/2} . \tag{1.6}$$

Detection of outflows with velocities ranging between 0.1c and 0.4c in BAL quasars APM08279+0522 (Chartas et al. 2002) and PG1115 + 080 (Chartas et al. 2003) has been reported from observations of X-ray broad absorption lines performed with the Chandra and XMM-Newton X-ray observatories. In the case of APM08279 + 0522 an intrinsic bolometric luminosity of $L_{\mathrm{bol}} \sim 2.4 \times 10^{47}\,\mathrm{erg\,s^{-1}}$ has been estimated by Egami et al. (2000). Under the assumption of $L_{\mathrm{Edd}} \sim$ 1–3 L_{bol}, the maximum observed velocity $v \simeq 0.4c$ is obtained with a launching radius $r_f \sim 0.5$–2×10^{16} cm. Such small values of r_f are confirmed by the observed variability of the absorption line energies and widths in APM08279 + 0522 over a proper timescale of 1.8 weeks (Chartas et al. 2003).

1.4.2 Jets

The other class of outflows is certainly more spectacular. In fact, relativistic jets are the largest astrophysical bodies that preserve their own identity as they extend from few Schwarzschild radii near the central black hole, up to Mpc scales outside the host galaxy. The ultra-relativistic outflows exhibit speeds which show typical Lorentz factors $\gamma \sim 10$. However, more extreme bulk velocities ($\gamma \gtrsim 100$) have been invoked to account for the extreme values of brightness temperatures inferred from intra-day variability (Kedziora-Chudczer et al. 1997). These observations strongly suggest that the outflows are formed quite deep in the potential well. This hypothesis has received support from VLBI observations of M87 which show that collimation takes place within ~ 20 Schwarzschild radii (Junor et al. 1999). Observations have also demonstrated that, even if the radio emission is only 1% (or much less) of the bolometric luminosity, the jet power can exceed the total power of the accreting gas (Rawlings & Saunders 1991; Celotti et al. 1997; Tavecchio et al. 2000). For example, in the case of Cygnus A, the jet power which inflates the two radio lobes must exceed $\sim 10^{45}\,\mathrm{erg\,s^{-1}}$, value which is comparable with the bolometric luminosity of a typical quasar (Wilson et al. 2000).

A still unanswered question is related to the composition of jet: are they made of protons and electrons, or electron-positron pairs, or a mixture of both? Arguments in favour of proton-electron jets in quasars have been presented by Celotti & Fabian (1993) based on the energetic of the jet and the required number of e^+e^- pairs. On the other hand, the discovery of circular polarization in the radio cores of quasars, such as 3C279, suggests that the jets plasma is dominated by e^+e^- pairs (Wardle et al. 1998, 2001). From X-ray observations of blazars Sikora & Modejski (2000) infer that jets contain many more e^+e^- pairs than protons, although these latter particles still dominate the dynamics.

The question of the composition of the jet plasma is also closely related to the still open issue of the formation of jets. They can be launched as outflows dominated by Poynting fluxes, generated in the force-free magnetosphere of a black hole (Blandford & Znajek 1977), or as hydromagnetic winds driven centrifugally from an accretion disk (Blandford & Payne 1982; Königl 1989). In any case, the key ingredient are magnetic fields that provide a natural mechanical link between disks and jets, as they account for the launching, confinement and collimation of jets. The maximal power, L_{BP}, extracted from a magnetized accretion disk is (Blandford & Payne 1982):

$$L_{\mathrm{BP}} = 4\pi \int \frac{B_{\mathrm{pd}}^2}{4\pi} R^2 \Omega(R) dR \tag{1.7}$$

where Ω is the angular velocity of the magnetic field lines and B_{pd} is the strength of the large scale ordered field at the disk surface.

On the other hand, when the hole spins, it can act as a unipolar inductor and create an emf $\sim 10^{20}$ V (Blandford & Znajek 1977). This emf can drive a closed and field-aligned current circuit that dissipates both within the horizon of the hole (the internal resistance of the circuit) and in the *astrophysical load.* The latter one is a region of weak magnetic field, where currents can cross the field lines and accelerate particles at the base of the jet. The electromagnetic power, L_{BZ}, extracted from a rotating black hole depends on the mass of the hole, on its spin and on the strength of the poloidal field threading the horizon (Blandford & Znajek 1997; Macdonald & Thorne 1982):

$$L_{\mathrm{BZ}} \simeq \frac{1}{64}\, A^2\, B_{\perp}^2\, R_h^2\, c \tag{1.8}$$

where A is the dimensionless angular momentum of the black hole and $B_{\perp}$ is the magnetic field component normal to the black hole horizon, $R_{\rm h}$. As the field $B_{\perp}$ is maintained by the currents in the accretion disk surrounding the BH, the strength of $B_{\perp}$ is expected to be of the same order of the magnetic field in the inner edge of the disk (i.e. $B_{\perp} \simeq B(R_{\rm in})$), which is usually assumed to scale with the pressure of the disk ($P_{\rm mag} = B^2/8\pi \simeq P_{\rm disk}$).

The origin of the ordered field, which is assumed to thread the disk and the hole, is still unclear. It is probably generated locally by the small-scale field created by dynamo processes (Balbus & Hawley 1991, 1998; Tout & Pringle 1996), rather than advected inwards by the accreting matter (Blandford & Payne 1982; Königl 1989). If this is the case, the poloidal field is only a small fraction of the field in the disk generated by the dynamo: $B_{\rm pd} \sim H/R\ B_{\rm dynamo}$ (Tout & Pringle 1996), where H is the scale-height of the disk. Therefore, in the case of standard Shakura-Sunyaev disks ($H/R \ll 1$), far more power is extracted from the inner disk via the Blandford & Payne mechanism (eq. 1.7) rather than from the hole directly, simply because of the larger area of the disk involved (Ghosh & Abramowicz 1997; Livio et al. 1999)

In recent years, due to the limitations of analytical models, many efforts have been done to study jet formation using Magneto Hydro Dynamic (MHD) simulations. Great progress has been achieved on several issues, such as studies on the behaviour of magnetic fields in disks (Balbus & Hawley 1998), on hydrodynamical accretion flows (Stone, Pringle & Begelman 1999), and of the inner black hole magnetosphere (Koide et al. 1999). New phenomena have also been proposed like magnetic switching (Meier 1999), or launching mechanisms related to instabilities in the disk (Hejuerat & Blandford 2004). In Chapter 2 and 3 we will tackle this open issue of jet formation from an observational point of view, trying to understand which properties can favour or prevent the formation of jets in quasars.

1.5 The spectrum of AGN

1.5.1 Continuum

The observable imprinting of AGN accretion processes and of their associated outflows comes from their emission properties. The spectral energy distribution (SED) of AGN is quite complex, extending from radio bands up to γ-ray photons and revealing the presence of many features, i.e. broad depressions and bumps. The very existence of these various features strongly suggests that different physical processes are at work, and they dominate the emission in different bands. As it is shown in Figure 1.1, most of the energy is emitted in a strong broad feature that dominates the spectrum at wavelengths shortwards $\sim$ 4000Å and extends to the UV and soft X-ray bands. This is the so-called *big blue bump*. It is attributed to some kind of thermal emission in the range $10^{5\pm1}$ K depending on whether the emission arises in optically thin (thermal Bremsstrahlung) or optically thick (blackbody) disks. Numerous authors have attempted detailed calculations of the SED emerging from accretion disks which include stellar atmosphere and general relativistic effects (Sun & Malkan 1989; Laor & Netzer 1989; Ross et al. 1992; Sincell & Krolik 1998; Hubeny et al. 2000, 2001). The simplest way is to assume that the disk radiates locally like a blackbody with a temperature at each radius r from the center (Shakura & Sunyaev 1976) given by:

$$T(r) \simeq 3.45 \times 10^7 \left(\alpha_V \frac{M_{\rm BH}}{M_\odot}\right)^{-1/4} \left(\frac{r}{R_{\rm S}}\right)^{-3/8} \tag{1.9}$$

where $R_S = 2GM/c^2$ is the Schwarzschild radius. This equation shows that the temperature of the disk actually decreases with increasing black hole mass. The superposition of blackbodies from many different radii produces the classical spectral energy flux $F_\nu \propto \nu^{1/3}$. There are many ways in which this standard result can be modified (see Blaes 2002 for a comprehensive review). For example, advection causes a redder spectrum, with $F_\nu \propto \nu^{-1}$ (Szuszkiewicz et al. 1996; Wang et al. 1999). There is also the possibility that the energy, liberated at small radii, can be reprocessed by the disk at larger radii (Frank et al. 2002) as well as relativistic light bending (Agol & Krolik 2000) or many other processes that are able to modify the spectrum.

These optical/UV photons are also the seeds for emission at higher energies (see Poutanen 1998; Zdziarski 1999 for a review). The basic idea is that the optical/UV continuum from the accretion disk is up-scattered in energy by inverse Compton scattering on hot (possibly relativistic) electrons with a temperature $T_e \sim 10^9$ K in a corona surrounding the disk (Shapiro et al. 1976; Sunyaev & Titarchuk 1980). The X-ray spectra basically consist

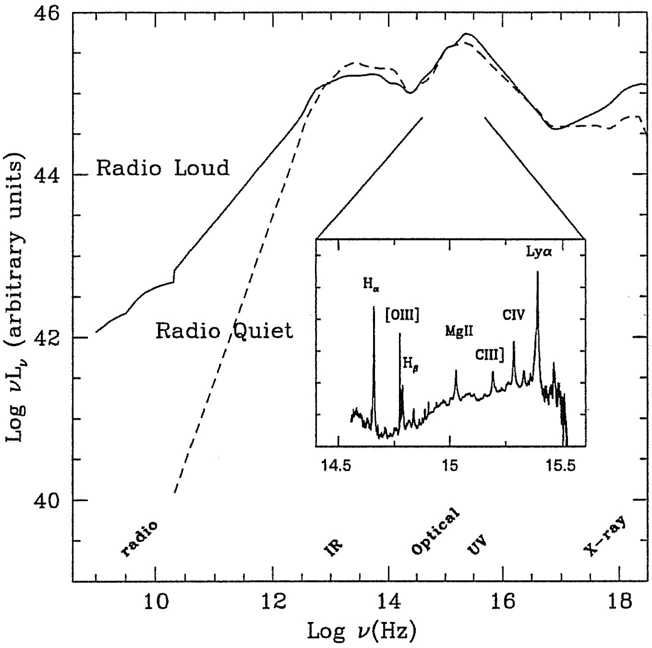

Figure 1.1: Mean spectral energy distribution for radio loud (solid line) and radio quiet (dashed line) quasars from Elvis et al. (1994). In the small window, it is also shown the composite quasar optical spectrum from Brotherton et al. (2001).

of (intrinsic) power laws (in units of photon per KeV $\propto E^{-\Gamma}$ with typical photon indices $\Gamma \sim 1.5 - 3$) accompanied, in most cases, by signatures of reprocessing by cold media: Compton reflection (Lightman & White 1988) and iron lines (George & Fabian 1991; see Fabian et al. 2000 for a review).

Another remarkable feature in the SED of an AGN is the presence of a local minimum in $\nu L(\nu)$ at wavelength $\sim 1\mu$m. This is thought to represent the minimum between the hot thermal spectrum (the big blue bump) and a cold thermal spectrum due to emission by warm dust grains. The temperature of such grains is below 1500-2000 K because, at higher temperatures, they sublimate.

Finally, about 10-20% of all AGN show high levels of radio emission and the presence of a jet. According to their radio luminosity or the ratio of radio (5 GHz) to optical (B-band) luminosities, AGN have been classified as "Radio Loud" or "Radio Quiet" (Kellerman et al. 1989; Miller et al. 1990). There is a long debated question related to the radio loudness in quasars and to the presence of a dichotomy separating these two populations, that will be extensively developed in Chapters 2 and 3. In contrast to optical/UV emission, the radio spectrum is non-thermal and originates from synchrotron radiation of relativistic electrons. The rate of synchrotron energy loss $\dot{E}_{\rm sync}$ by a single electron moving in a magnetic field with energy density $U_{\rm mag}$, is given by:

$$-\dot{E}_{\rm sync} = 2\sigma_T\,\gamma^2\,\beta^2 sin^2\theta U_{\rm mag} c, \tag{1.10}$$

where $\beta = v/c$, $\gamma = (1-\beta^2)^{1/2}$ is the Lorentz factor and θ is the pitch angle ($cos\theta = \hat{\mathbf{v}}\cdot\hat{\mathbf{B}}$). The synchrotron emissivity for a population of electrons will be $\epsilon_\nu = -\dot{E}N(E)dE/d\nu$, where N(E) is the number of electrons in the energy range (E, E+dE). For a power-law spectrum of electrons with $N(>\gamma) = N_0\gamma^{1-x}$, where N_0 is the total electron number density, the synchrotron emissivity becomes:

$$\epsilon_\nu \propto B^{1+\alpha_R}\,\nu^{-\alpha_R} \tag{1.11}$$

where $\alpha_R \equiv (1+x)/2$ is the radio spectral index.

According to their radio spectral index, objects have been sub-divided in flat ($\alpha_R \lesssim 0.5$) and steep ($\alpha_R \gtrsim 0.5$) spectrum sources. When the radio synchrotron emission of a jet is self-absorbed and mainly unresolved, the sum of the different components mimics a flat spectrum and constitutes the so-called radio core. At larger radii, the emission is optically thin and generally associated to the external lobes revealing the classical steep spectrum feature.

1.5.2 Emission lines

The visible spectra of AGN are also characterized by several emission lines. They can provide diagnostics for velocities, temperatures and densities unavailable from any other observational technique. These lines represent re-radiation by individual ions of energy originating from (a more primordial) continuum. We deal with two fundamental categories of emission lines: those produced by decays occurring during ionic recombination following ionization and those produced by decays following collisional excitations by other particles in the gas. The former ones (recombination lines) are mainly hydrogen lines. Collisionally excited lines are usually forbidden lines (i.e. [OII], [OIII], [NeIII]), even though two of the strongest permitted lines MgII and CIV are also collisionally excited.

A further classification of the emission lines observed in AGN spectra is between the *broad* lines, with full widths at half maximum (FWHM) of the order of 5000 km s^{-1} and *narrow* lines with FWHM of the order of 500 km s^{-1}. Forbidden transitions are only found as narrow lines, whereas permitted lines may have both broad and narrow components. At high densities, forbidden lines are collisionally suppressed so that they appear weak when compared to both permitted collisionally excited lines and recombination lines. It can then be concluded that the narrow lines in AGN spectra come from lower velocity and lower density regions, at variance with what happens in the case of broad lines. These two regions are therefore respectively called the *Narrow Line Region* (NLR) and the *Broad Line Region* (BLR).

The energy source that drives the emission lines in AGN spectra is almost certainly photoionization by the continuum radiation from the central source. Direct evidences come from observations of broad lines whose fluxes vary strongly in response to changes in continuum fluxes. The absence of forbidden lines and the presence of some semi-forbidden ones (i.e. CIII]) implies an electron density of about 10^9 cm^{-3} in the BLR. The size of BLRs has been estimated to be of the order a few light days to $\sim$ 100 light days, growing with luminosity as $L^{0.5}$ (Peterson 1993; Kaspi et al. 1996; Wandel 1997). The radiating mass of gas is estimated to be about $10^3 M_\odot$ decreasing to less than $1 M_\odot$ for less powerful sources, with a covering factor of the order of 10% or less. Surrounding the BLR is the NLR, that extends from a few tens of parsec to over a kiloparsec and exhibits lower ionization states and lower densities, of the order of $10^3 - 10^4$ cm^{-3}.

1.6 Unification scheme for AGN

The intrinsically complex nature of AGN systems and the differences in the terminology among different scientific communities (radio, optical, X-ray astronomers) had led throughout the years to an extremely complicated nomenclature for the AGN zoo. As the wealth of observations piled up, and with them the number of different AGN types, the enterprise of finding unification schemes has progressively gained support. The basic idea behind any unification scheme is that AGN are *asymmetric* and *anisotropic* systems. This is natural, as all rotating systems necessarily single out a preferential axis in space and break the full spherical symmetry of non-rotating bodies. Therefore, the orientation of the AGN rotation axis with respect to our line of sight becomes another important parameter that can make two sources that are intrinsically identical observationally different.

According to the current widely accepted paradigm, there are two principal causes for the anisotropic radiation: *obscuration* and *relativistic beaming.* The former is usually associated with a torus of gas and dust obscuring the optical/UV and sometimes soft X-ray radiation along some line of sights, the latter with outflows of energetic particles (jets) along the symmetry axis: the high velocity plasma in the jet relativistically beams the radiation in the forward direction.

Following the approach of Urry & Padovani (1995), we present a classification of the principal AGN types summarized in Table 1.1 (adopted from Lawrence 1987), where they are organized according to their radio loudness (vertical axis) and their optical spectra, i.e. to whether they have broad emission lines (Type 1), only narrow emission lines (Type 2), or weak or unusual line emission (Type 0). Within each group, different types of AGN are listed by increasing nuclear luminosity.

- Sources with bright continua and broad emission lines from hot, high-velocity gas, presumably located deep in the gravitational well of the central black hole, are known as Type 1 AGN. In the radio quiet group, these include the Seyfert 1 galaxies (Sy1), which have relatively low-luminosities and therefore are only seen nearby, and the higher-luminosity radio quiet quasars (QSO), which are typically seen at greater distances (because of their local relative rarity) and thus are usually unresolved and rarely show an obvious galaxy surrounding the bright central source. The radio loud Type 1 AGN are called Broad-Line Radio Galaxies (BLRG) at low optical luminosities and Radio-Loud Quasars at higher luminosities, respectively indicated as Steep Spectrum Radio Quasars (SSRQ) or Flat Spectrum Radio Quasars (FSRQ) depending on the radio continuum shape. Other than luminosity, little distinguishes Seyfert 1s from radio quiet quasars, or BLRG from radio quasars.

- Type 2 AGN have weak continua and only narrow emission lines, meaning either

	Type 2 (Narrow Lines)	Type 1 (Broad Lines)	Type 0 (Unusual)
Radio Quiet	Sy 2	Sy 1	
	NELG	Radio Quiet Quasars (QSO)	
	Type 2 QSO		
Radio Loud	NLRG $\left\{\begin{array}{l}\text{FRI}\\ \text{FRII}\end{array}\right.$	BLRG	Blazars $\left\{\begin{array}{l}\text{BLLac}\\ \text{FSRQ}\end{array}\right.$
		SSRQ	
		FSRQ	
	– Decreasing angle to line of sight →		

Table 1.1: AGN taxonomy, from Urry & Padovani (1995). See text for details.

that they have no high velocity gas or, as we now believe, that the line of sight to such gas is obscured by a thick wall of absorbing material. Radio quiet Type 2 AGN include Seyfert 2 galaxies at low luminosities, as well as the Narrow Emission Line Galaxies (NELG). The high luminosity counterparts are not clear identified, but likely candidates are the heavily obscured quasars recently detected in X-rays by *Chandra* (Norman et al. 2002; Crawford et al. 2002). Radio loud Type 2 AGN, often called Narrow-Line Radio Galaxies (NLRG), include two distinct morphological types: the low-luminosity Faranoff-Riley type I (FR I) radio galaxies (Faranoff & Riley 1974), which have symmetric radio jets whose intensity falls away from the nucleus, and the high-luminosity Faranoff-Riley type II (FR II) radio galaxies, which have more highly collimated jets leading to well-defined lobes with prominent hot spots.

- A small number of AGN have very unusual spectral characteristics. Following Urry & Padovani (1995), we call these objects "Type 0" AGN and speculate that they are characterized by a very small angle to the line of sight. These include the BL Lacertæ (BL Lac) objects, which are radio loud AGN that lack strong emission or absorption features. A subset of Type 1 quasars, including those variously defined as Optically Violent Variable (OVV) quasars, Highly Polarized Quasars (HPQ), Core-Dominated Quasars (CDQ) or Flat Spectrum Radio Quasars (FSRQ), are probably also found at a small angle to the line of sight. Their continuum emission strongly resembles that of BL Lac objects (apart from the presence of a blue bump in a few cases) and, like BL Lac objects, they are characterized by very rapid variability, unusually high and variable polarization, high brightness temperatures and superluminal velocities of compact radio cores. Although the names OVV, HPQ, CDQ and FSRQ reflect different empirical definitions, evidence is accumulating that they are more or less the same thing. Collectively, BL Lac and FSRQ are called Blazars.

1.7 Cosmological evolution of AGN

In the previous section it has been discussed how, under the simple assumptions of obscuration and beaming due to the presence of outflows, different classes of observed AGN can be reconciled under the unique hypothesis of an accreting massive black hole. Let us now consider these objects within their cosmological context. What do we know about the cosmological evolution of AGN?

Since their discovery, it was soon realized that the space density of both radio and optically selected quasars increases significantly with redshift (Schmidt 1968, 1970). The effect is so strong that it was detectable in a sample as small as containing only 20 objects. Subsequently, using the UV excess technique, significant advance was achieved in both sample size and limiting magnitude (Schmidt & Green 1983; Boyle et al. 1988). The situation in the late 1980s was that either the space density of quasars increased by more than a factor 100 between redshift 0 and 2 (Schmidt & Green 1983), or their characteristic luminosity increased by a factor 30 (Boyle et al. 1988) within the same redshift interval. However, the UV excess technique only allowed to select sources up to $z \sim 2$. A significant step forward in exploring the higher redshift Universe was obtained in the 1990s, by using either multi-color selection or low-resolution spectroscopy. A convincing evidence for a steep decline at $z > 3$ in their space density was found for luminous optically selected quasars (Warren, Hewett & Osmer 1991, 1994; Schmidt, Schneider & Gunn 1995; Kennefick, Djorgovski & de Carvalho 1995). These results, combined with the behaviour at lower redshifts, indicate a remarkable spike of optically selected quasar activity when the

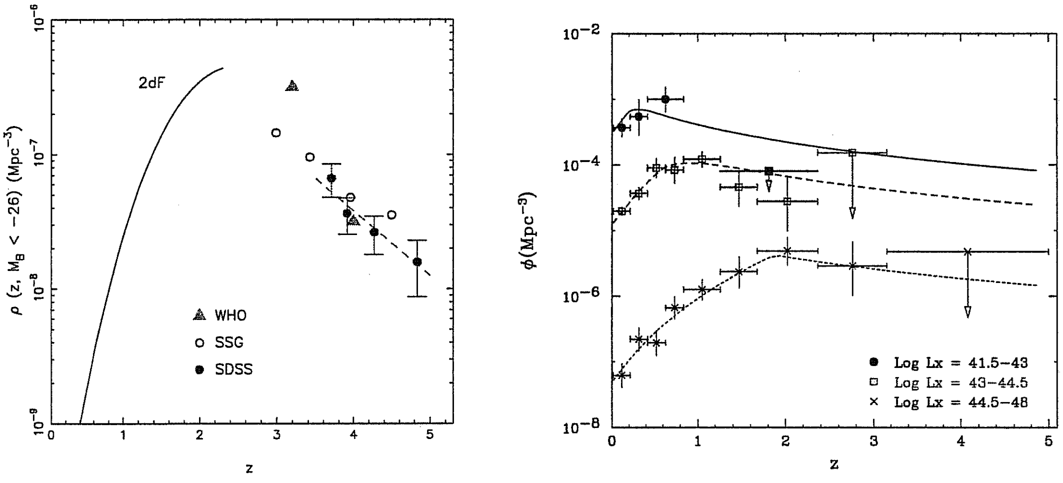

Figure 1.2: Left panel: space density of optically selected quasars as a function of redshift from Fan et al. (2001b). The solid line shows the space density derived from the 2dF survey (Boyle et al. 2000), compared with higher redshift determinations: triangles from Warren, Hewett & Osmer (1991, 1994), open circles from Schmidt, Schneider & Gunn (1995) and solid circles from Fan et al. (2001b). Right panel: space density as a function of redshift for X-ray selected sources of different luminosities from Ueda et al. (2003).

Universe was 15-20% of its current age.

These results have been confirmed by recent large area surveys and in particular by the 2dF Quasar Redshift Survey (Boyle et al. 2000; Croom et al. 2001, 2004) and Sloan Digital Sky Survey (SDSS, York et al. 2000). The former survey – extensively described in Chapter 2 – constrained the evolution of the optically selected quasar population in the redshift range $0.35 \lesssim z \lesssim 2.2$. Their main result is that a model with pure luminosity evolution works fine, with the characteristic luminosity of optical quasars increasing by a factor of 40 at the peak of activity, with respect to local determinations.

On the other hand, the SDSS opened an important window for the search of high redshift quasars through its large areal coverage ($\sim$ 10,000 sq. deg.) and its use of the z^* filter with $\lambda_{\rm eff} \approx 9100$Å, which extended the discovery space up to very high redshifts. So far, the most distant quasar found is at $z = 6.43$ (Fan et al. 2003), and up to now 12 quasars with $z > 5.7$ (Fan et al. 2004) have been found. Fan et al. (2001a,b), by exploiting the SDSS data, computed the quasar luminosity function (LF) in the range $3.6 \leq z \leq 5.0$ for a color-selected sample of 39 quasars in 182 sq. deg. of sky. This analysis confirmed the sharp decline of the quasar space density (see Figure 1.2) beyond $z \gtrsim 2.5$.

Deep radio observations – down to few tens of μJy – of the Fan et al. (2001b) sample will be presented in Chapter 5 in order to investigate the radio properties of quasars at high redshift. In fact, radio data can be important to provide information on the question of obscuration by dust at high redshifts.

The evolution of the space density up to $z \sim 4$ of powerful radio sources ($P_{2.7} \gtrsim 7 \times 10^{26}$ W Hz^{-1} sr^{-1}) is found to be very similar to the optical one (Hook et al. 1998). This is a strong evidence against dust reddening being the main cause of the decline at high redshifts, even though the significant fraction of sources with very red values of B-K in radio selected quasars indicates that dust could severely affect optical surveys (Webster et al. 1995; Whiting et al. 2001; Gregg et al. 2002). In Chapter 4 we will tackle in more detail the issue of the evolution of radio quasars, with particular attention devoted to the issue of the faint sources.

Another important challenge in recent years has been the assessment of the evolution of low luminosity AGN. The luminosity function of quasars up to redshift ~ 5 was mapped – down to $M_{1450} \sim -21$ – by the multi-band imaging survey COMBO-17 (Wolf et al. 2003). The slope of its faint end at high z is remarkably flat, in agreement with more recent determinations from GOODS (Cristiani et al 2004) and VIRMOS data (Bongiorno, Cirasuolo et al. in preparation). A similar result has been obtained by Hunt et al. (2004) investigating the AGN population, found in a deep spectroscopic survey of Lyman-break galaxies.

However, the most surprising results were recently obtained with the help of X-ray data. XMM-Newton and Chandra observations resolved in discrete sources more than 90% of the 0.1-10 keV X-ray background (Hasinger et al 2001; Giacconi et al. 2002). Spectroscopic identifications revealed the redshift distribution of these sources to be peaked at $z \sim 0.7$ and dominated by Seyfert-like galaxies. This is a strong indication that the evolution of this latter population is considerably different from that of optically selected quasars, which exhibit a peak activity around $z \sim 1.5 - 2$. Recently, Ueda et al. (2003), by using a sample of 247 AGN over a wide flux range from 10^{-10} to 3.8×10^{-15} erg cm^{-2} s^{-1} (2-10 KeV), computed the Hard X-ray LF up to $z \sim 3$. This LF shows that luminous AGN (quasars) and less luminous ones (Seyfert galaxies) exhibit different evolutionary properties in terms of the cutoff redshift above which the evolution terminates, implying that quasars formed earlier than less luminous AGN (see Figure 1.2). The LF is well described by a *luminosity dependent density evolution* model where the redshift cutoff decreases from ~ 1.9 in the case of bright sources ($L_X \gtrsim 10^{45}$ erg s^{-1}) to ~ 0.8 for sources with $L_X \sim 10^{43.5}$ erg s^{-1}.

1.8 Importance of AGN in galaxy formation

Is it possible to relate this differential evolution found in the AGN population to the properties of their host galaxies and to shed light on the processes of galaxy formation? Powerful AGN (quasars) are mainly associated to spheroidal galaxies, while the less luminous Seyferts reside in spirals. Although the traditional approach to galaxy formation and evolution regards nuclear activity as an incidental diversion, in recent years it is becoming more and more clear that this is intimately related to the formation of the host galaxy. The first main evidence was the discovery of massive black holes ($10^6 - 10^9 M_\odot$) in at least all the local galaxies endowed with a spheroidal component (Kormendy & Richstone 1995). Furthermore, the local black hole mass function matches remarkably well that of the baryons accreted onto BHs during their active nuclear phase (Salucci et al. 1999; Marconi et al. 2004; Shankar et al. 2004).

However, the most convincing evidences come from the discovery of tight correlations between the mass of the central BH and large scale properties of the host spheroids. McLure & Dunlop (2002) found that the central BH mass, $M_{\rm BH}$ and the total R-band magnitude, $M_{\rm R}$, of the bulge are strictly related:

$$\log(M_{\rm BH}) = -(0.5 \pm 0.05) M_{\rm R} - (2.91 \pm 1.04) \tag{1.12}$$

with a scatter of $\Delta\log(M_{\rm BH}) = 0.33$. A larger scatter $\Delta\log(M_{\rm BH}) \simeq 0.45$ was found by Kormendy & Gebhardt (2001) using B-band luminosities which are not as good stellar mass tracers as the R-band luminosities. For galaxies observed with a spatial resolution high enough to resolve the BH sphere of influence, Marconi & Hunt (2003) report a tight correlation between $M_{\rm BH}$ and the host galaxy bulge K-band luminosity, with a scatter of $\Delta\log(M_{\rm BH}) = 0.33$. This latter relation yields higher masses at a fixed luminosity with respect to the relation of McLure & Dunlop (2002). The above discrepancy is possibly related to the fact that, at a given luminosity, selecting galaxies with resolved BH sphere of influence favours objects with higher BH mass.

The other tight observational correlation recently discovered in galaxies endowed with a bulge component is the one between $M_{\rm BH}$ and the velocity dispersion of the stellar spheroid, σ (Ferrarese & Merritt 2000; Gebhardt et al. 2000). Even though the existence of this relation is undisputed, its precise trend is still under debate. Tremaine et al. (2002), from a detailed analysis of a sample of galaxies with dynamical measurements of the central $M_{\rm BH}$, found:

$$\log(M_{\rm BH}) = (4.02 \pm 0.32)\log\left(\frac{\sigma}{200\ {\rm km\ s^{-1}}}\right) + (8.13 \pm 0.06) \qquad (1.13)$$

which is marginally consistent with the $M_{\rm BH} \propto \sigma^{4.58\pm0.52}$ found by Ferrarese (2002). The scatter around the mean relation is small, $\Delta\log(M_{\rm BH}) = 0.3$ and possibly consistent with pure measurement errors.

Clues on the joint of evolution of both galaxies and quasars are also provided by studies of chemical abundances (e.g. Friaça & Terlevich 1998). Spectroscopic observations in fact demonstrate a fast metal enrichment of the circum-nuclear gas even for the highest redshift quasars (e.g. Hamann & Ferland 1999; Fan et al. 2000; Freudling et al. 2003; D'Odorico et al. 2004).

1.8.1 When did Spheroids form?

In the light of these tight relations between the central BH and the properties of its host galaxy, what can we say about the history of galaxy formation? The two main theoretical models for the formation of galaxies – hierarchical formation and monolithic collapse – predict for spheroidal galaxies a very different history, for what concerns the formation epoch and the assembling processes. In the hierarchical scenario early type galaxies form by mergers of disks at relatively recent times (Toomre & Toomre 1972; White & Rees 1978; Blumenthal et al. 1984). This scenario tends to imply that most of the star formation occurs in relatively small galaxies that later merge to make bigger and bigger objects, with the most massive galaxies assembled only recently (Kauffmann 1996). On the other hand, in the traditional monolithic collapse scenario these massive systems formed their stars and assembled their mass in a short timescale, which is much shorter than their average age (Eggen, Lynden-Bell & Sandage 1962). This formation process happened at high redshifts in a substantial single burst later followed by an essentially passive evolution phase.

A key to solve this long-standing rebus can be provided by observations. The present day stellar populations in elliptical galaxies are coeval and presumably old (Sandage & Visvanathan 1978; Forbes & Ponman 1999; Trager et al. 2000a,b). Moreover, in the local Universe these objects obey a colour-magnitude relation: brighter spheroids are redder than less luminous ones (Bower et al. 1992). The widely accepted interpretation is that brighter objects are more metal rich and that star formation in these galaxies started and ceased early enough in cosmic time that the effects of any possible spread in the formation epoch are not detectable through broad band colours (Bower et al. 1998). Recent studies support this theory, suggesting that the slope of this relation does not change with redshift (Ellis et al. 1997; Kodama et al. 1998) as well as the scatter does not increase (Stanford et al. 1995, 1998; Ellis et al. 1997). Statistical studies of local spheroidal galaxies, hosting supermassive black-holes, also show in these objects an excess of the α-elements$/Fe$ ratio, when compared to solar (α-enhancement; Trager et al. 2000a,b; Thomas et al. 2002), suggestive of a past very intense but short star-formation activity.

Another promising way to "measure" the star formation history of spheroidal galaxies is provided by studies of the Fundamental Plane (Djorgovski & Davies 1987; Dressler et al. 1987) and its evolution with redshift. The Fundamental Plane is a tight empirical correlation found in spheroidal galaxies between the effective surface brightness SB_e, the velocity dispersion σ and the effective radius R_e (defined as the radius containing half of the light):

$$\log R_e = \alpha_{\rm FP} \log\sigma + \beta_{\rm FP}\, SB_e + \gamma_{\rm FP} \qquad (1.14)$$

where $\alpha_{\rm FP}$ and $\beta_{\rm FP}$ are called the slopes and $\gamma_{\rm FP}$ is called the intercept. Spheroidal galaxies are clustered on this plane with a surprisingly small orthogonal scatter, $\sim 15\%$ as what is expected for a homogeneous family of galaxies (Jørgensen et al. 1996; Treu et al. 2001). Moreover, recent studies by Treu et al. (2002) suggest that ellipticals – at least the ones in cluster – follow this fundamental relation up to $z \sim 1$, consistently with the hypothesis that massive spheroids are old and quiescent.

Another stringent evidence in favour of the early formation of spheroidal galaxies has been obtained in the last few years, by exploring the distant Universe: the detection of a large population of massive galaxies at $z \gtrsim 2$ by sub-millimeter surveys with SCUBA and MAMBO (Blain et al. 2002; Scott et al. 2002). These sources are mainly found to be very massive, with high star formation rates (SFRs $\sim 10^3 M_\odot$) embedded in a dusty environment (Dunlop 2001; Ivison et al. 2002; Aretxaga et al. 2003; Chapman et al. 2003). This suggests massive galaxies with $M \gtrsim 10^{11} M_\odot$ to be forming at $z \gtrsim 2$, in agreement with recent results obtained with K-band surveys (Cimatti et al. 2002; Kashikawa et al. 2003; Fontana et al. 2004). It is worth noting that the space density of these massive objects at $z \gtrsim 3$ is only a factor $\sim 5 - 10$ less than that at $z \sim 1$ (Tecza et al. 2004).

1.8.2 How to reconcile theory and observations

All these observational evidences seem to support the traditional monolithic scenario for galaxy formation. On the other hand, this framework is known to be inadequate as it cannot be fitted in a consistent scenario for structure formation from primordial density fluctuations. How to reconcile theory and observations? Since CDM was first considered in the late seventies (e.g White & Rees 1978), it was soon realized that some processes – namely feedbacks – must be invoked to prevent gas from cooling too fast, otherwise all the available gas would have cooled and turned into stars by the present day. The conventional feedback scheme (Dekel & Silk 1986), where energy feedback from supernova explosions is assumed to drive the cooled gas out of the galactic halo, may only be effective in very low mass galaxies (Mac Low & Ferrara 1999; Mori et al. 2002). Performing three-dimensional hydrodynamical simulations, Mori et al. (2002) found that for an object of total mass of 10^8 $M_\odot$, depending on the spatial stellar distribution, only $\sim 30\%$ of the available supernova energy is converted into kinetic energy of the escaping material, the remainder being radiated away.

Several semi-analytical models have been developed by using simple parameterized prescriptions for this feedback as well as for star formation processes within the CDM framework (Kauffmann et al. 1993,1994,1997; Cole et al. 1994,2000; Baugh et al. 1996,1998; Mo et al. 1998,1999; van Kampen et al. 1999; Somerville et al. 1999,2001; Menci et al. 2002). However, these models are unable to reproduce the space density of massive objects ($M \gtrsim 5 \times 10^{10} M_\odot$) and their colours, in particular with increasing redshift (Fontana et al. 2004). This problem has been partially solved by assuming merging or interaction-induced star formation (Somerville et al. 2004; Menci et al. 2004). By doing this, the observed space density can be reproduced up to $z \sim 1.5$ (Fontana et al. 2004), while at higher redshifts it is still underestimated (see also Nagamine et al. 2001, 2004).

The above discussion might have us wondering on whether there is still a missing ingredient to the phenomenon of galaxy formation. As discussed in the previous sections, tight relations have been observed between the central black hole and the global properties of spheroidal galaxies. Therefore, it has been suggested that feedback from the AGN activity might be important for galaxy formation. The basic idea is that the accreting black hole grows in parallel with the bulge until some feedback – possibly quasar outflows – expels the gas and terminates the star formation (Silk & Rees 1998; Fabian 1999). In this way a tight relation between galaxy and AGN activity is established, with the latter supplying the energy to unbind the gas and halt the star formation.

The mechanical luminosity (i.e. wind, L_K) can be taken to be a fraction f_w of the Eddington luminosity (Silk & Rees 1998):

$$L_\mathrm{K} = \frac{1}{2}\dot{M}_w v_w^2 = f_w L_\mathrm{Edd}, \tag{1.15}$$

where $\dot{M}_w$ is the mass of the outflow and v_w its velocity. In order to unbind the gas, the wind velocity should exceed the escape velocity from the galaxy: $v_w > \sigma$. By using $\dot{M}_w = 4\pi r^2 \rho(r) v_w$ and assuming a density profile $\rho(r) = \sigma^2/2\pi G r^2$ we get the condition:

$$L_\mathrm{K} > \frac{\sigma^5}{G} = 5 \times 10^{43} \left(\frac{\sigma}{200\,\mathrm{km\,s^{-1}}}\right)^5 \mathrm{erg\,s^{-1}} \tag{1.16}$$

that translates into a condition on the mass of the central black hole:

$$M_{\rm BH} \gtrsim 10^7 \left(\frac{\sigma}{200\,{\rm km\,s^{-1}}}\right)^5 M_\odot \qquad (1.17)$$

Therefore, in the case of massive spheroids having $\sigma \sim 200 - 300\ {\rm km\,s^{-1}}$, black holes could in principle eject all the material from their host galaxy when their mass exceeds $\sim 10^7 - 10^8 M_\odot$.

However, in its present form, the proposed mechanism does not imply shorter star-formation times for more massive galaxies and therefore cannot easily explain the α-enhancement of more massive objects. The evolution of active nuclei and of host galaxies was also analyzed in the framework of the hierarchical clustering scenario, using a semi-analytic approach. Kauffmann & Haenhelt (2000) and Haenhelt & Kauffmann (2000) proposed that merging process determines both the evolution of galaxies and the growth of the black-holes at their centers. Volonteri et al. (2002, 2003) presented a model in which most of the mass in BHs is assembled in accretion episodes triggered by merging.

In Chapter 6 we will tackle this issue, describing a model for the coevolution of galaxies and quasars (Granato et al. 2004). In this model, feedback from supernova explosions and, for the most massive galaxies, from nuclear activity, is able in the case of baryons to reverse the hierarchical scenario, which holds for the dark matter. For the most massive galaxies, the gas unbinding time should be short enough for the bulk of the star formation to be completed before Type Ia supernovae can substantially increase the iron abundance of the ISM, thus accounting for the α-enhancement seen in the largest galaxies. In other words, the canonical hierarchical CDM framework - small clumps collapse first - should be reversed for baryon collapse and the formation of luminous objects (*Anti-hierarchical Baryon Collapse* scenario).

1.9 Outlines

In the light of this brief discussion, in Chapter 2 we present the analysis of a new sample of faint quasars, both in radio and optical, obtained from the cross-correlation of FIRST and 2dF QSO Redshift Survey. The properties of this sample are described, with particular attention devoted to the long debated question of radio loud (RL)/ radio quiet (RQ) dichotomy. Since selection effects introduce severe uncertainties on the determination of the radio loudness, in Chapter 3 we present a new approach to tackle this issue based on Monte Carlo analysis of optically selected quasar samples. This allow us to investigate the intrinsic radio properties of quasars.

In Chapter 4 we exploit the large dataset of quasars drawn from the final releases of both FIRST and 2dF QSO Redshift Survey to study cosmological evolution of quasars. Particular emphasis is devoted to the behaviour of faint sources and to the connection between radio galaxies and quasars, within the unification scheme for AGN. In Chapter 5, we extend our studies of radio loudness up to high redshift, presenting preliminary results obtained from deep VLA observations of a complete sample of quasars drawn from SDSS.

The final part of the thesis (Chapter 6) is instead devoted to study the connection between the central BH – powering nuclear activity – and formation of their host galaxies. Finally, we discuss our conclusions and future prospects in Chapter 7.

For sake of comparison with previous works, in the first part of this thesis (Chapters 2,3,4,5) we will adopt Einstein-de Sitter Cosmology with $\Omega_m = 1$, $\Omega_\Lambda = 0$ and $H_0 = 50\ \mathrm{km\,s^{-1}Mpc^{-1}}$ (hereafter E.d.S.). However, note that in the redshift range considered ($0 \lesssim z \lesssim 2$) the results obtained throughout this work are not very different from the new "concordance" ΛCDM cosmology, with $\Omega_m = 0.29$, $\Omega_b = 0.047$, and $\Omega_\Lambda = 0.71$, $H_0 = 72\ \mathrm{km\ s^{-1}}$, adopted in Chapter 6.

Chapter 2

The Radio Loud / Radio Quiet dichotomy

2.1 Introduction

It was soon realized that not all the quasars, though first discovered by Schmidt in 1963 at radio wavelengths, are powerful radio sources (Sandage 1965). Several optically selected quasar samples have been observed in radio (e.g. Sramek & Weedman 1980; Condon et al. 1981; Marshall 1987; Miller, Peacock & Mead 1990; Kellermann et al. 1989), showing that typically only 10% - 40% of the quasars are radio detected.

From these studies it was suggested that quasars can be divided into the two different populations of "Radio-Loud" and "Radio-Quiet" on the basis of their radio emission. Kellermann et al. (1989), performing VLA observations of the Palomar-Green Bright Quasar Survey (the so-called PG sample), found that the radio-to-optical ratios of these objects – defined as the ratio between radio and optical luminosity – presented a bimodal distribution, clearly showing the occurrence of these two different populations. Miller, Peacock & Mead (1990) also found a dichotomy in the quasar population, although this time based on radio luminosity as the parameter to define the level of radio loudness.

A step forward in the study of the radio properties of quasars came with the FIRST Survey with the VLA (Becker, White & Helfand 1995) which was able to collect a large sample of quasars at faint flux levels. Recent works based on this survey (FIRST Bright Quasar Survey; White et al. 2000 and Large Bright Quasar Survey; Hewett et al. 2001) suggest that the RL/RQ dichotomy could be an effect due to the brighter radio and optical limits of the previous studies. The issue is however still under debate. A recent work by Ivezic et al. (2002), based on the cross-correlation of the Sloan Digital Sky Survey with the FIRST Survey seems to find clear evidence for bimodality (see also Goldschmidt et al. 1999).

From the theoretical point of view, despite the great advances in our ability of collecting unbiased sets of data, the physical mechanism(s) responsible for the radio emission in Active Galactic Nuclei is still unclear, as discussed in Chapter 1. It is generally accepted to be related to the processes of accretion onto a central black hole (BH) – the engine responsible for the optical-UV emission – but no tight correlation between radio and optical luminosity has been found so far in such objects (see e.g. Stocke et al. 1992). On the other hand, although controversial, there is some evidence for the fraction of radio-loud quasars to increase with increasing optical luminosity (Padovani 1993; La Franca et al. 1994; Hooper et al. 1995; Goldschmidt et al. 1999; but see also Ivezic et al. 2002 for a dissenting view).

A different approach deals with the possibility for radio loudness to be connected with the intrinsic properties of the host galaxy. Early studies in fact concluded that, while radio-loud quasars reside in elliptical hosts, radio-quiet ones are mainly found in spiral galaxies (Malkan 1984; Smith et al. 1986). Furthermore, it was observed a preference for radio-quiet quasars to be located in environments considerably less dense than those of radio-loud objects (Yee & Green 1987; Ellingson et al. 1991).
More recent studies (Dunlop et al. 2003; Finn et al. 2001) however find a very different picture whereby the hosts of both radio-loud and radio-quiet quasars are massive elliptical galaxies with basic properties (colors, environments, etc.) indistinguishable from those of quiescent, evolved, low-redshift ellipticals of comparable mass.

In this Chapter we analyze a wide sample of radio detected quasars drawn from the joined use of the FIRST and 2dF QSO Redshift Surveys in order to answer some of the questions raised throughout this section, with particular emphasis on the issue of radio-quiet/radio-loud dichotomy.

The layout of this Chapter is as follows. In Section 2 we give a brief description of the FIRST and 2dF datasets and of the matching procedure used to cross-correlate them, while in Section 3 we analyse the properties of the sample obtained from the joined use of these two surveys. In Section 4 we study the dependence on redshift and optical luminosity of the fraction of radio-detected quasars and in Section 5 we discuss the problem of radio loudness with particular attention devoted to the issue of radio-loud/radio-quiet dichotomy. In Section 6 we summarize our conclusions. Throughout this Chapter we will adopt the E.d.S. Cosmology (see Chapter 1).

2.2 The Datasets

2.2.1 The FIRST Survey

The FIRST (Faint Images of the Radio Sky at Twenty centimeters) survey (Becker et al. 1995) began in 1993 and will eventually cover $\sim 10,000$ square degrees of the sky in the North Galactic cap and equatorial zones. The beam-size at 1.4 GHz is 5.4 arcsec, with an rms sensitivity of typically 0.15 mJy/beam. Sources are detected using an elliptical Gaussian fitting procedure (White et al. 1997) with a 5σ detection limit of ~ 1 mJy. The positional accuracy in the FIRST survey is $\lesssim 0.5$arcsec at the 3 mJy level, reaching the value of 1 arcsec only at the survey threshold.

The release of the catalogue (5 July 2000), used for the work presented in this Chapter, covers 7988 square degrees of the sky, including most of the area $7^h20^m \lesssim$ RA(2000) $\lesssim 17^h20^m$, $22.2^\circ \lesssim$ dec(2000) $\lesssim 57.5^\circ$ and $21^h20^m \lesssim$ RA(2000) $\lesssim 3^h20^m$, $-2.8^\circ \lesssim$ dec(2000) $\lesssim 2.2^\circ$, and comprises approximately 722,354 sources down to a flux limit $S_{1.4\mathrm{GHz}} \simeq 0.8$ mJy. The surface density of objects in the catalogue is ~ 90 per square degree, though this is reduced to ~ 80 per square degree if one combines multi-component sources (Magliocchetti et al. 1998). The survey has been estimated to be 95 per cent complete at 2 mJy and 80 per cent complete at 1 mJy (Becker et al. 1995). Note that, as the completeness level quickly drops for flux levels fainter than 1 mJy, in the following analysis we will only consider sources brighter than this limit.

2.2.2 The 2dF Quasar Redshift Survey

For the purposes of this work we have considered the first release of the 2dF QSO Redshift Survey, the so called *2QZ 10k catalogue*. A complete description of the catalogue can be found in Croom et al. (2001). Here we briefly recall its main properties. QSO candidates with $18.25 \leq b_J \leq 20.85$ were selected from the APM catalogue (Irwin, McMahon & Maddox 1994) in two $75^\circ \times 5^\circ$ declination strips centered on $\delta = -30^\circ$ and $\delta = 0^\circ$, with colour selection criteria $(u - b_j) \leq 0.36$; $(u - b_j) < 0.12 - 0.8\ (b_j - r)$; $(b_j - r) < 0.05$. Such a selection guarantees a large photometric completeness (> 90 %) for quasars within the redshift range $0.3 \leq z \leq 2.2$.

Redshifts for QSO candidates were determined via both cross-correlation of the spectra with specific templates (AUTOZ, Miller et al. in preparation) and by visual inspection. A flag was then assigned to each spectrum, where Q=1 corresponds to high quality identifications and redshift determinations, Q=2 means low-quality identifications and redshift determinations and Q=3 indicates no redshift assignment.

Only 2dF fields with a spectroscopic completeness (defined as the ratio of objects observed in the field with Q=1 or Q=2 flags to the total number of spectroscopically observed objects) of 85 per cent or greater were included in this first release of the 2dF QSO catalogue. This corresponds to a mean overall completeness of 93 per cent which – by also allowing for sources not yet observed in the targeted fields – converts into an effective area for the survey of 289.6 square degrees (see Croom et al. 2001).

The final catalogue contains $\sim 21,000$ objects with reliable (Q=1; Q=2) spectral and redshift determinations, out of which $\sim 11,000$ are quasars (~ 53 % of the sample). Whenever available, the 2QZ 10k catalogue also includes radio fluxes at 1.4 GHz from the NRAO VLA Sky Survey (NVSS; Condon et al. 1998) and X-ray fluxes from the ROSAT All Sky Survey (RASS; Voges et al. 1999).

2.2.3 Matching Procedure

The overlapping region between the FIRST and 2dF Quasar Redshift Surveys is confined to the equatorial plane: $9^h\ 50^m \leq$ RA(2000) $\leq 14^h\ 50^m$ and $-2.8^\circ \leq$ dec(2000) $\leq$

2.2°. Optical counterparts for a subsample of FIRST radio sources have been obtained by matching together objects included in the radio catalogue with objects coming from the APM survey (Maddox et al. 1990) in the considered area (for a similar analysis see also McMahon et al. 2002). By following this procedure, Magliocchetti & Maddox (2002) find 4075 identifications – out of a total of $\sim$ 24,000 $S_{1.4\mathrm{GHz}} \geq 1$ mJy radio sources – in the APM catalogue down to $b_J \leq 22$ and for a matching radius of 2 arcsec. This last value was chosen after a careful analysis as the best compromise to maximize the number of real associations (estimated to be $\sim$ 97%), and at the same time minimize the contribution from spurious identifications down to a negligible 5 per cent.

While this procedure has been proved to work for the population of radio sources as a whole since it mainly includes radio galaxies with point-like radio structures (Magliocchetti et al. 2002), caution needs to be taken when dealing with powerful radio sources such as quasars. These objects in fact often show multiple components such as jets and/or hot-spots. The algorithm introduced by Magliocchetti et al. (1998) and adopted in this work to collapse sub-structured sources into single objects having radio fluxes equal to the sum of the fluxes of the various components, assigns positions to the final single-source products which correspond to the median point between the different sub-structures. Since multiple-component objects in general present quite complex morphologies, it can be possible that a number of "collapsed" sources end up with radio positions for their centroids which are displaced from their optical counterpart by more than the originally chosen value of 2 arcsec.

For this reason, we relax the requirement on the matching radius to 5 arcsec and consider as true optical identifications all the radio-optical pairs offset by less than this value.

Following the above procedure, we end up with 1044 identifications (hereafter called id-sample), down to a magnitude limit $b_J = 20.85$, which optically show point-like structures typical of the population of QSOs (see Magliocchetti & Maddox 2002 for further details).

Finally, in order to obtain redshift measurements and spectral features for these sources, we looked for objects in the 2QZ 10k catalogue with positions which differ by less than 2 arcsec from the optical positions of sources in the id-sample. The choice of this value for the matching radius is based on the 2 arcsec diameter of each 2dF fibre. This

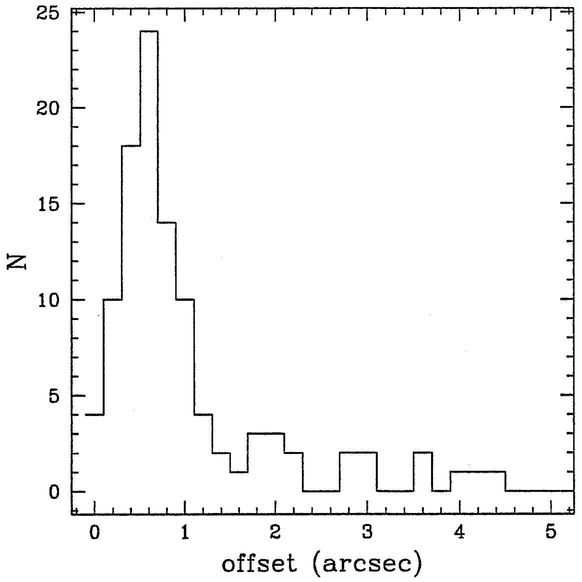

Figure 2.1: Distribution of offsets between radio and optical positions for the sub-sample of 2QZ 10k quasars included in the FIRST survey.

procedure leads to 104 quasars included in the 2dF QSO catalogue and endowed with radio fluxes $S_{1.4\mathrm{GHz}} \geq 1$ mJy. The distribution of offsets between optical and radio positions is shown in Figure 2.1. Note that, despite the problems associated with multi-component structures discussed in this section, the overwhelming majority ($> 90\%$) of identifications still lie within 2 arcsec from the corresponding radio position. As expected, only a few sources (almost all associated to multi-component structures) present offsets $> 2''$.

As a final remark we note that, even though a choice for a larger matching radius in principle increases the number of spurious associations, this is not a concern in our analysis given the low space-density of 2dF quasars. In fact, for a 5 arcsec matching radius, the expected number of random coincidences on an area of 122 square degrees (effective area of the overlapping region between the FIRST and 2dF QSO Surveys) is about 7×10^{-2}.

2.2.4 FIRST vs NVSS

To double check the reliability of our sample and to also investigate the different efficiency of the FIRST and NVSS surveys in detecting sources, we have then compared objects from the sample obtained as in section 2.3 with those sources included in the 2QZ 10k catalogue and endowed with a radio-flux measurement from NVSS.

42 sources from the combined FIRST-2dF dataset do not present NVSS flux measurements in the 2QZ catalogue. A direct search for these objects in the NVSS on-line database found 14 of them in the flux range $3 \lesssim S_{1.4\mathrm{GHz}} \lesssim 600$ mJy. Out of these 14 sources, three objects show multiple components and were therefore lost in the 2dF-NVSS matching procedure due to lack of a combining algorithm for sub-structured objects. Three more are instead single sources which show quite large radio-to-optical offsets (>7 arcsec). The others are single objects with offsets $\lesssim 3$ arcsec and it is not clear why they were not included in the 2QZ 10k catalogue. The remaining 28 sources included in the combined FIRST-2dF catalogue show fluxes $S_{1.4\mathrm{GHz}} \lesssim 3$ mJy and were therefore lost by NVSS because of its relatively bright (~ 3 mJy; Condon et al. 1998) flux limit.

Following the same procedure as above, we also found 9 of the 2dF quasars with NVSS fluxes to be missed by our matching procedure. After a direct search, it turned out that six of them are double/triple sources, with positions for the centroids (as assigned by our combining procedure) which were displaced from the centers of the optical emission by more than 5 arcsec. The last three objects are instead point-like sources with radio-to-optical offsets between 5 and 7 arcsec and therefore lost by our searching criteria. These 9 sources have been added to our original FIRST-2QZ 10k dataset and appear in Table A.1 in Appendix.

As a final remark, note that the high resolution of the FIRST survey (beaming size 5.4 arcsec) might imply some of the flux coming from extended sources to be resolved out, leading to a systematic underestimate of the real flux density of such sources. In order to check for this effect, we have compared FIRST and NVSS (which, having a lower resolution – beaming size of 45 arcsec – should not be affected by this problem) fluxes for all the sources in the 2QZ 10k catalogue which show a radio counterpart in both of these radio surveys. The result of the comparison is shown in Figure 2.2. It is clear that the agreement between fluxes as measured by FIRST and NVSS is excellent and therefore no correction to the flux densities derived from the FIRST survey is needed.

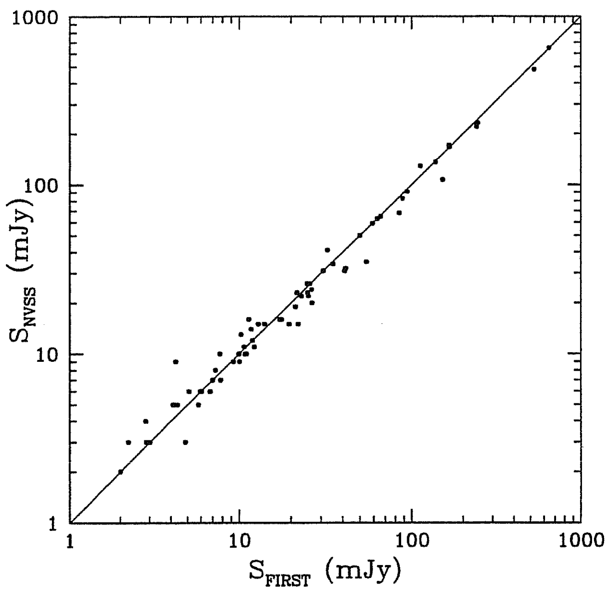

Figure 2.2: Comparison between 1.4 GHz fluxes as measured by the FIRST and NVSS Surveys for sources in the FIRST-2dF sample.

2.3 The Samples

2.3.1 FIRST-2dF

Based on the procedure described in the previous section, the sample derived from the joined use of the FIRST and 2dF QSO surveys is constituted by 113 objects (hereafter in this Chapter called the FIRST-2dF sample) with optical magnitudes $18.25 \leq b_J \leq 20.85$ and radio fluxes at 1.4 GHz $S_{1.4\mathrm{GHz}} \geq 1$ mJy. All the objects included in the FIRST-2dF sample are presented in Table A.1 in Appendix.

The redshift distribution of these sources is shown in the top panel of Figure 2.3 as a dotted line. For comparison, Figure 2.3 also shows the redshift distribution of the $\sim 4,000$ quasars from the 2QZ 10k catalogue found in the North Galactic Cap (indicated by the solid line). Interestingly, the two distributions present the same trend, as they both smoothly rise for $z \gtrsim 0.3$, exhibit a maximum at about $z \sim 1.5$ and then decline at higher redshifts. This could be suggestive of a similar fueling mechanism which controls the birth and life-time of quasars, regardless of their radio-emission.

Note that the observed trend for the two redshift distributions beyond $z \geq 2.1$

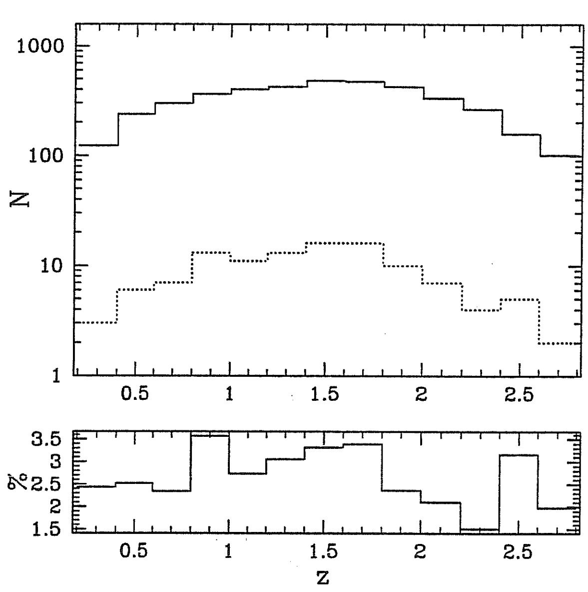

Figure 2.3: Top panel: redshift distribution for the sample of FIRST-2dF QSOs (dotted line) and for all the quasars from the 2QZ 10k catalogue found in the North Galactic Cap (solid line). Bottom panel: ratio between the two distributions.

is biased by lack of completeness in the 2QZ 10k sample due to colour selection effects. For this reason, in the following analysis we will only consider objects in the redshift range $0.35 \leq z \leq 2.1$. The total number of sources in the FIRST-2dF sample is then reduced to 94, which also includes 3 Broad Absorption Lines QSO (BAL).

The lower panel of Figure 2.3 shows the ratio between the two redshift distributions. This ratio is found to be ~ 3 % over the entire redshift range. As it will be extensively discussed in the following sections, the joined effects of selecting sources in the blue band and of using a relatively faint magnitude range, makes the above figure lower than what previously found in literature ($\sim 10-20$ per cent; White et al. 2000; Hewett, Folz & Chaffee 2001; Ivezic et al. 2002).

Figure 2.4 shows the distribution of $b_J - r$ colours for the sample of FIRST-2dF quasars (filled squares) as a function of redshift (top panel); a large fraction of sources present values $0 \lesssim b_J - r \lesssim 1$ (see lower panel), independent of redshift. For comparison, the top panel in Fig. 2.4 also shows, in small dots, the distribution of $b_J - r$ colours obtained for all the 2QZ quasars included in the overlapping FIRST/2dF region (North

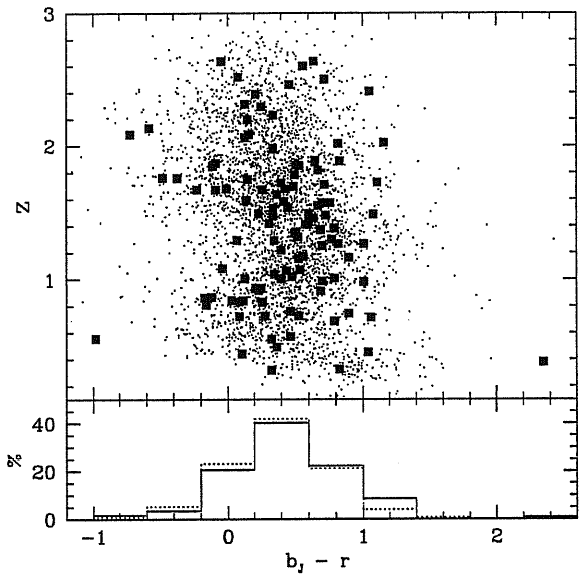

Figure 2.4: Top panel: $b_J - r$ colours versus redshift for the FIRST-2dF sample (filled squares) as compared with the ones obtained for all the 2QZ 10k quasars in the North Galactic Cap (small dots). The lower panel represents the distributions of $b_J - r$ colours for the FIRST-2dF sample (solid line) and for all the 2QZ 10k quasars, expressed as a percentage over the total number.

Galactic Cap). As shown in Figure 2.5 the distribution of $b_J - r$ colours is also independent of apparent magnitude and radio flux. It is evident that radio-emitting sources follow the same distribution as the one obtained for the quasar population as a whole, suggestive of a radio activity not related to the colour of the source.

Note that two objects present colours which greatly differ from the average values, the first one showing $b_J - r > 2$ and the second one having $b_J - r \lesssim -1$. This is presumably due to their faint absolute optical magnitudes (found to be ~ -21 and ~ -22 respectively in the first and second case), which allow for a non-negligible light contribution from the host galaxy or due to measurement error.

A further piece of information on the nature of sources in the FIRST-2dF sample is given by the investigation of their radio spectral index α_R [1]. In order to measure α_R we searched for observations performed at different (usually at 5 GHz) wavelengths using NED (NASA/Ipac Extragalactic Database). Unfortunately, as objects in our sample are

---

[1] As defined in Chapter 1, throughout this work we define the radio flux density as $S_\nu \propto \nu^{-\alpha_R}$

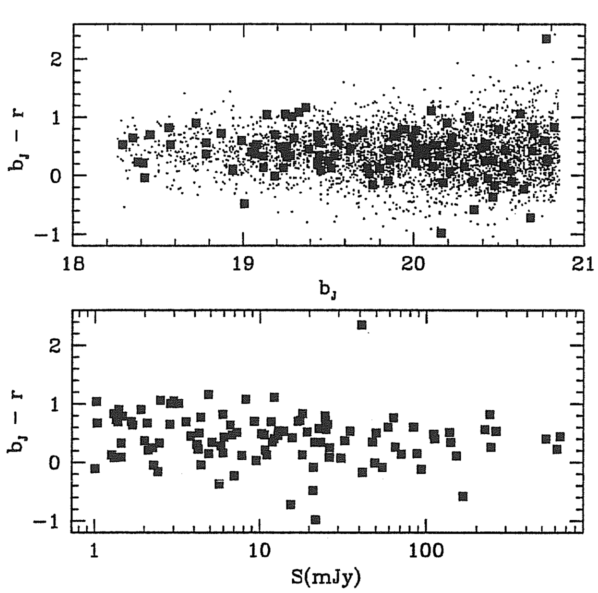

Figure 2.5: $b_J - r$ colours versus b_J magnitude (top panel) and radio flux at 1.4 GHz (lower panel). Symbols are as in Figure 2.4.

relatively faint, we only managed to acquire radio fluxes at 5 GHz for the ten most luminous ($S_{1.4\mathrm{GHz}} \geq 100$ mJy; see Table A.1) ones. The distribution of their spectral indices is found to be rather uniform, with five steep spectrum ($\alpha_R > 0.5$) and four flat spectrum ($\alpha_R < 0.5$) sources, plus one object which presents a negative value for the radio spectral index ($\alpha_R = -0.6$).

As the remaining objects do not have any counterpart for radio frequencies $\nu > 1.4$ GHz, this suggests that sources in our sample mainly present steep radio spectra, since values $\alpha < 0.5$ would make at least some of them observable in surveys performed e.g. at 5 GHz. With some confidence we can then assume most of the quasars in the FIRST-2dF sample to have a steep spectrum and associate them to a mean value for the radio spectral index, $\alpha_R = 0.8$.

As a final step – in order to facilitate comparisons between our results and those found in literature – we decided to convert magnitudes from the b_J to the B band. To compute the mean $B - b_J$ we used the composite quasar spectrum compiled by Brotherton et al. (2001) from ~ 600 radio-selected quasars in the FIRST Bright Quasar Survey (FBQS). It turns out that in the redshift range $0.3 \leq z \leq 2.2$ the difference between corresponding values in the two bands is very small, $0.05 \lesssim B - b_J \lesssim 0.09$, independent of redshift. We therefore chose to apply a mean correction $B = 0.07 + b_J$. Note that the K-correction in the B band has also been computed from the Brotherton et al. (2001) composite quasar spectrum.

2.3.2 LBQS

In the previous section we have shown the main observational properties of the FIRST-2dF quasars. Even though ~ 100 radio-emitting QSOs represent one of the widest samples obtained so far, nevertheless – in order to increase the statistics and cover larger portions of the $M_B - z$ plane – we decided to combine our dataset with other existing samples. Thanks to its selection criteria, the Large Bright Quasar Survey (LBQS) comes as the natural extension of our original dataset to brighter magnitudes. A detailed description of this survey can be found in Hewett et al. (1995). Briefly, it consists of quasars optically selected from the APM catalogue (Irwin et al. 1994) at bright ($b_J < 19$) apparent magnitudes. Redshift measurements were subsequently derived for 1055 of them over an effective area of 483.8 square degrees. Due to the selection criteria of the survey, quasars were detected over a wide redshift range ($0.2 \leq z \leq 3.4$), with a degree of completeness estimated to be at the $\sim 90\%$ level.

Recently, this sample has been cross-correlated with the FIRST radio survey (Hewett et al. 2001) by using a searching radius of 2.1 arcsec over an area of 270 square degrees. This procedure yielded a total of 77 quasars (hereafter called the FIRST-LBQS sample) with radio fluxes $S_{1.4\mathrm{GHz}} \geq 1$ mJy, magnitudes in the range $16 \lesssim b_J \lesssim 19$, and fractional incompleteness of $\sim 10\%$.

2.3.3 The Combined Sample

The joined FIRST-LBQS and FIRST-2dF samples span a wide range in magnitudes – $16.5 \lesssim b_J \lesssim 20.85$ – providing a very good coverage of the $M_B - z$ plane. This can be seen in Figure 2.6 which represents the distribution of absolute M_B magnitudes as a function of redshift for the two datasets. In the redshift range where our sample is

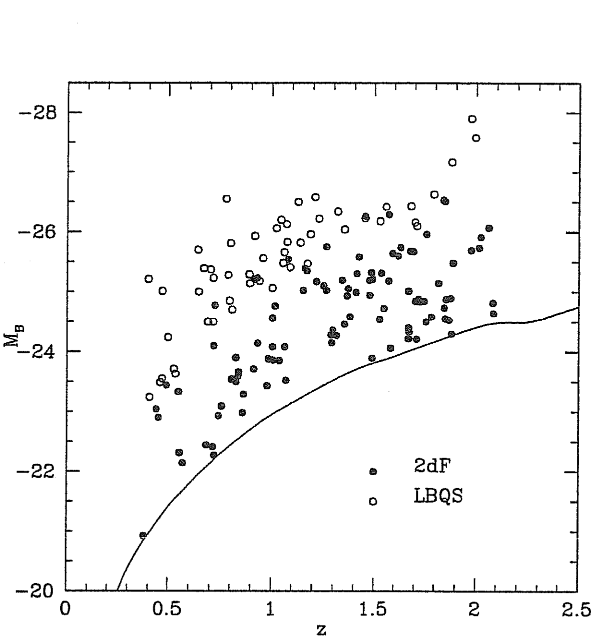

Figure 2.6: Absolute M_B magnitude versus redshift for the FIRST-2dF (filled circles) and the FIRST-LBQS (empty circles) samples. The solid line describes the selection effect due to the limiting magnitude $b_J = 20.85$.

complete ($0.35 \leq z \leq 2.1$) a wide portion of the $M_B - z$ plane is filled by sources, and this obtained with the advantage of using only two samples, drawn from the same parent catalogues (FIRST and APM) and with compatible selection criteria.

We remind here that low-redshift, low-luminosity quasars with $M_B > -23$ may have their optical emission dominated by the host galaxy, and can therefore be missed from the 2QZ catalogue as a result of the stellar appearance selection criterion applied to the input catalogue. Following the works by Boyle et al.(2000) and Croom et al.(2001), we then exclude from the dataset all the low-luminosity quasars with $M_B > -23$. As Figure 2.6 shows, this final sample exhibits a full coverage of the $M_B - z$ plane, except for the narrow region $-24 \lesssim M_B \lesssim -23$ at $z \gtrsim 1$.
Note that the radio power-redshift plane (see Figure 2.7) is also widely covered; only the region between $23 \lesssim \log_{10}\mathrm{P}_{1.4\mathrm{GHz}}\,(\mathrm{W\,Hz^{-1}\,sr^{-1}}) \lesssim 24$ is not entirely filled, due to the 1 mJy flux limit of the FIRST survey.

To summarize, our final sample is made of 141 quasars, either coming from the 2QZ 10k catalogue or from the LBQS dataset. These sources, brighter that $b_j = 20.85$ and

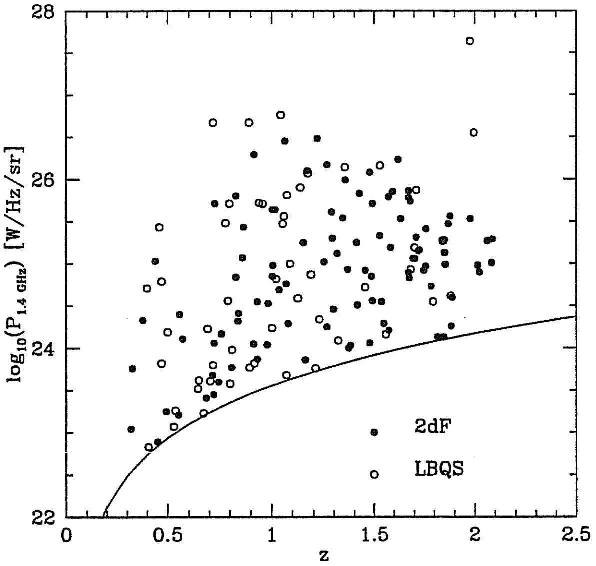

Figure 2.7: Radio-power $P_{1.4\mathrm{GHz}}$ versus redshift for the FIRST-2dF (filled circles) and the FIRST-LBQS (empty circles) samples. The solid line describes the selection effect due to the limiting flux density of 1 mJy.

$M_B = -23$, are found in the redshift range $0.35 \leq z \leq 2.1$, and are endowed with a radio counterpart in the FIRST catalogue with $S_{1.4\mathrm{GHz}} \geq 1$ mJy. The sample is estimated to be $\gtrsim 90\%$ complete with respect to the optical selection criteria and spectroscopic data acquisition, and 80% complete in its radio component (with a completeness level reaching 100% for fluxes brighter than 3 mJy; see Becker et al. 1995).

In the following sections we will then exploit the potentialities of this sample, homogeneous and deep both in radio and in optical, to investigate the properties of radio-active quasars.

2.4 Fraction of Radio Detected Quasars

A key point on the properties of quasars is the determination of the fraction of radio-emitting sources at a certain flux level, and its possible dependence on redshift and optical luminosity.

As it was shown in Figure 2.3, from the FIRST-2dF sample we find this fraction to

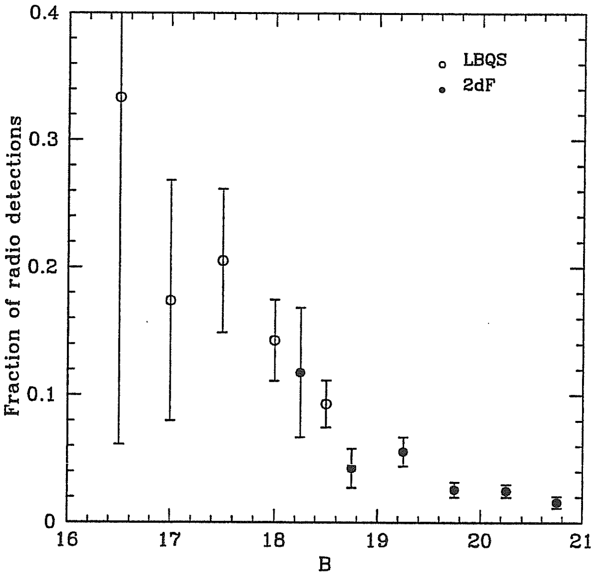

Figure 2.8: Fraction of sources with a counterpart in the FIRST Survey ($S_{1.4\mathrm{GHz}} \geq 1$ mJy) for the Large Bright Quasar Survey (empty circles) and 2QZ 10k (filled dots) sample as a function of apparent magnitude.

be relatively small ($\sim$ 3%) when compared to previous works ($\sim 10-20$ per cent; White et al. 2000; Hewett, Folz & Chaffee 2001; Ivezic et al. 2002), and independent of redshift. The dependence of the fraction of radio-detected quasars on apparent B magnitude is instead presented in Figure 2.8, both for the FIRST-LBQS and the FIRST-2dF samples. Note that with "radio-detected" we indicate all the quasars having radio fluxes greater then 1 mJy and therefore observed by FIRST. As already noticed by Hewett et al. (2001), we find a significant decrement for increasing magnitudes, with the fraction of radio-detections going from $\sim$ 20% at B=17 to $\sim$ 2% at B=21. These values are somewhat different from the 25% of objects with magnitudes $E \leq 17.8$ deduced by White et al. (2000) from the First Bright Quasar Survey (FBQS). However, Hewett et al. (2001) point out that by applying corrections for the bandpass differences between the LBQS and the FBQS surveys (selected in B_J and E band respectively), the predicted fraction of radio-detected quasars with magnitudes $E \leq 17.8$ is found to be 15-17%, which is close to the value obtained for the LBQS sample.

The observed behaviour of the fraction of radio-detected quasars could be ex-

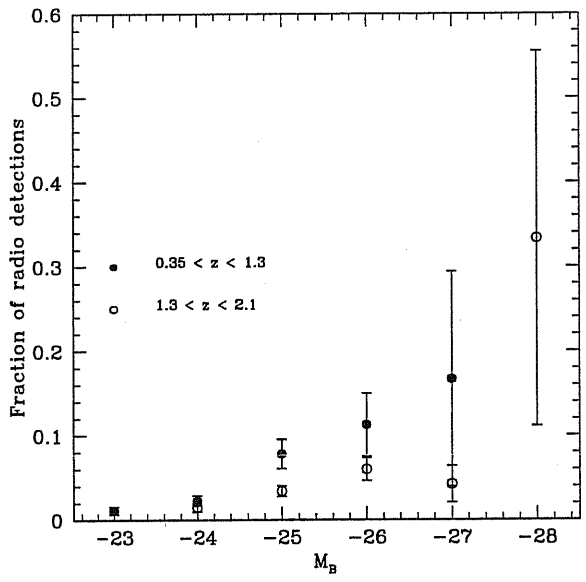

Figure 2.9: Fraction of sources with a counterpart in the FIRST Survey ($S_{1.4\mathrm{GHz}} \geq 1$ mJy) from both the Large Bright Quasar Survey and 2dF QSO sample as a function of absolute magnitude M_B in the two redshift ranges: $0.35 \leq z \leq 1.3$ (filled circles) and $1.3 < z \leq 2.1$ (empty circles). Only sources with $\log_{10} \mathrm{P}_{1.4\mathrm{GHz}} \geq 24$ (W Hz^{-1}sr^{-1}) have been used in this case.

plained as either due to an intrinsic dependence of this fraction on optical luminosity, as already suggested by Miller et al. (1990), or as simply given by selection effects. In order to test these hypotheses, in Figure 2.9 we have plotted the fraction of quasars from both the 2QZ 10k sample and the LBQS that have a counterpart in the FIRST catalogue as a function of the absolute magnitude M_B, and for the two different redshift bins $0.35 \leq z \leq 1.3$ and $1.3 < z \leq 2.1$. To minimize the selection effects, we have chosen to use only objects with radio powers $\log_{10}\mathrm{P}_{1.4\mathrm{GHz}} \geq 24$ (W Hz^{-1} sr^{-1}), since from Figure 2.7 it can be seen that the range $23 \leq \log_{10} \mathrm{P}_{1.4\mathrm{GHz}}(\mathrm{W\ Hz^{-1}sr^{-1}}) < 24$ is not sampled over the entire redshift range due to the 1 mJy flux threshold of the FIRST.

It turns out that the fraction of radio-detected quasars is indeed dependent on their optical luminosity: it grows from $\lesssim 5\%$ in the case of faint ($M_B \sim -24$) objects, up to $\sim 20\%$ for the most powerful sources with $M_B \lesssim -27$. This trend, although more significant in the lower redshift bin, appears to be present in both of the redshift bins, suggesting an optical luminosity function for the radio-detected quasars flatter than the one measured for the quasar population as a whole. This result is in agreement with what found by Goldschmidt et al. (1999) from the Edinburgh Survey, who also observe the fraction of radio-detected QSOs to slightly decrease for increasing redshift. Our data show something similar but, because of the large error-bars associated to high optical luminosities, this finding does not have great statistical significance.

In fact, if we perform a Kolmogorov-Smirnov (KS) test we find that, while the hypothesis for the two samples of optical quasars and radio-detected ones to have the same distribution in absolute magnitude is discarded at a very high significance level (probability $\sim 10^{-8}$), the same test gives a probability of ~ 0.7 for the data sets to be drawn from the same redshift distribution.

2.5 Radio Loudness

In this section we will tackle in more detail the issue of radio loudness, with particular attention devoted to the problem of RL/RQ dichotomy. Two parameters have been proposed to define the radio-loudness of a quasar: the first one is the radio-to-optical ratio R^*_ν defined as the ratio between the rest frame radio luminosity at a given frequency ν and the optical luminosity usually in the B band (Kellermann et al. 1989). Miller et al. (1990) however argued that R^*_ν has a physical meaning only if radio and optical luminosities are linearly correlated, and therefore chose the radio power P_ν as a better parameter to describe the level of radio loudness.

Several studies which used radio surveys at 5 and 8.5 GHz (Stocke et al. 1992; Padovani 1993; Hooper et al. 1995; Goldschmidt et al. 1999) argued for a gap in the distribution of radio powers and/or radio-to-optical ratios for the objects under exam. The same behaviour was also recently claimed by Ivezic et al. (2002). The presence of a bimodal distribution has been interpreted in the past as direct evidence for quasars to be divided into the two distinct populations of "radio-loud " and "radio-quiet", with different properties and probably also different mechanisms responsible for the radio emission. The threshold values at which the radio-quiet/radio-loud transition would happen have been inferred by these early works to be $R^*_{8.5} \sim 10$ (corresponding to $R^*_{1.4} \sim 30-40$ for objects with spectral

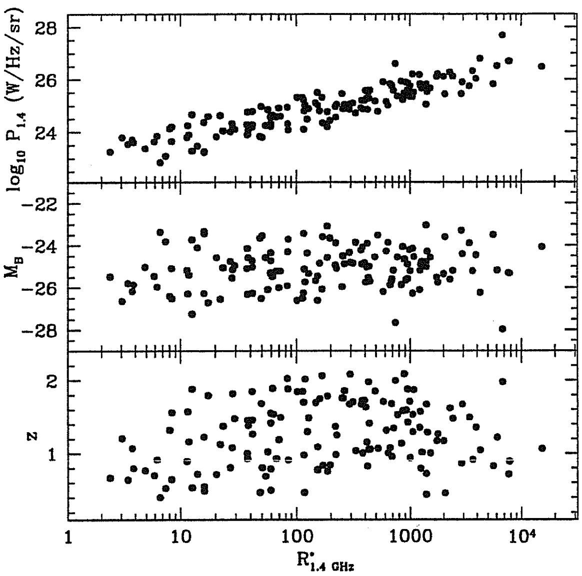

Figure 2.10: Radio-to-optical radio $R^*_{1.4}$ versus radio power (top panel), absolute magnitude (middle panel) and redshift (bottom panel) for the sources in our combined (FIRST-2dF and FIRST-LBQS) sample.

index $\alpha_R = 0.8$) or $\log_{10} \mathrm{P}_{5\mathrm{GHz}} \sim 24$ (W Hz^{-1}sr^{-1}).

It is worth remarking here that the above definitions are not equivalent. In fact, if we consider our combined FIRST-2dF and FIRST-LBQS dataset and plot the radio-to-optical ratio $R^*_{1.4}$ as a function of radio luminosity $\mathrm{P}_{1.4\mathrm{GHz}}$ (top panel of Figure 2.10), it becomes clear that not all the sources (although still a great portion of them) satisfying one of the two criteria can be accepted as radio-loud by the other one. This is the reason why in the following sections – in order to assess the possible presence of a RL/RQ dichotomy in our sample – we will consider both the $R^*_{1.4}$ and $\mathrm{P}_{1.4\mathrm{GHz}}$ distributions.

Note that if we apply the above definitions for radio loudness to the combined sample, we then find ~ 75% of the sources to be considered as "radio-loud", with the remaining ~ 30 – 40 objects probing part of the "radio quiet" regime.

As a last consideration before investigating in more detail the issue of dichotomy, we note that the distribution of radio-to-optical ratios for the combined sample is independent of both optical luminosity (middle panel of Figure 2.10) and redshift (bottom panel of Figure 2.10). This last finding is in agreement with the results obtained by White et al.

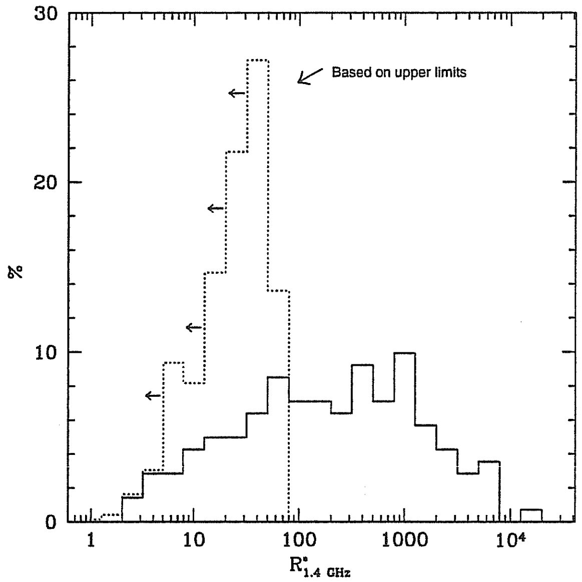

Figure 2.11: Distribution of radio-to-optical ratios $R^*_{1.4}$ for the sources in the combined sample expressed in percentages (solid line). The dotted histogram has been obtained for all the quasars found in the North Galactic Cap of the 2QZ 10k catalogue and the Large Bright Quasar Sample which do not have a radio counterpart in the FIRST survey, by assuming an upper flux limit of 1 mJy (see text for details).

(2000) for the First Bright Quasar Survey and Hewett et al. (2001) for the Large Bright Quasar Survey.

2.5.1 No Evidence for a Bimodal Distribution

The previous definitions of radio loudness were introduced in literature because the distributions of radio power and R^* for the objects under exam appeared to be bimodal. In order to test the presence of this bimodal behaviour in our dataset, we have then considered the distribution of radio-to-optical ratios $R^*_{1.4}$ for objects in the combined sample. As Figure 2.11 illustrates, our data (shown by the solid line) do not present any gap around $R^*_{1.4} \sim 40$, and the distribution appears to be quite flat over a large range of radio-to-optical ratios, the decline observed for $R^*_{1.4} \lesssim 30$ being fully consistent with effect of the 1 mJy flux limit of the FIRST survey.

This effect becomes more clear if one considers Figure 2.12, where the apparent optical

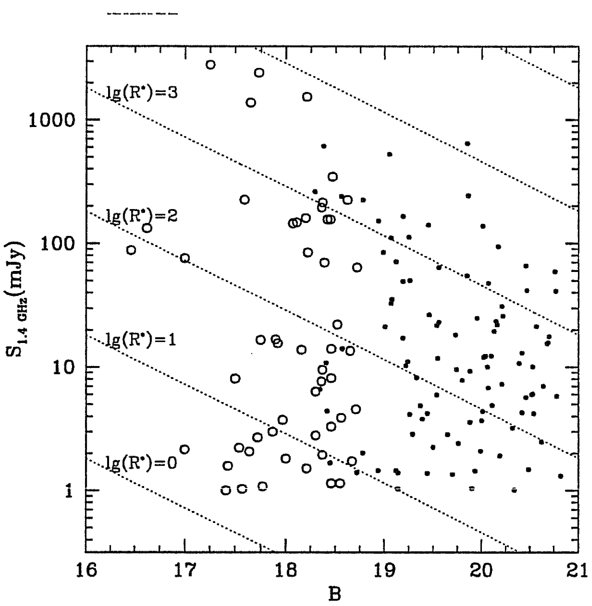

Figure 2.12: Radio flux S versus B magnitude for the FIRST-2dF (filled dots) and FIRST-LBQS (empty circles) samples. The dotted lines are the loci of constant radio-to-optical ratio $R^*_{1.4}$ (see text for details).

magnitude B has been plotted as a function of the radio flux at 1.4 GHz both for the FIRST-2dF and the FIRST-LBQS samples. The dotted lines represent the loci of constant radio-to-optical ratio. One can then see that the 1 mJy radio limiting flux determines a loss of $R^*_{1.4} \lesssim 40$ sources for the FIRST-2dF sample and of $R^*_{1.4} \lesssim 7$ for the FIRST-LBQS sample, and that these losses which become progressively more relevant for lower radio-to-optical ratio.

To have an idea of the R^* distribution of these "missing" sources, we can plot (as shown by the dotted line in Figure 2.11) the distribution of radio-to-optical ratios for those quasars found in the North Galactic Cap of the 2QZ 10k Survey and in the Large Bright Quasar Survey which do not have a counterpart in the FIRST catalogue, where values for R^* have been calculated by assuming an upper flux limit of 1 mJy. We can reasonably conclude that our data show no evidence for a $R^*_{1.4} \sim 30 - 40$ gap, in agreement e.g. with the White et al.(2000) results on the FBQS sample.

The presence of a bimodal distribution in the population of quasars has been recently re-claimed by Ivezic et al.(2002) who analysed a sample of radio sources obtained

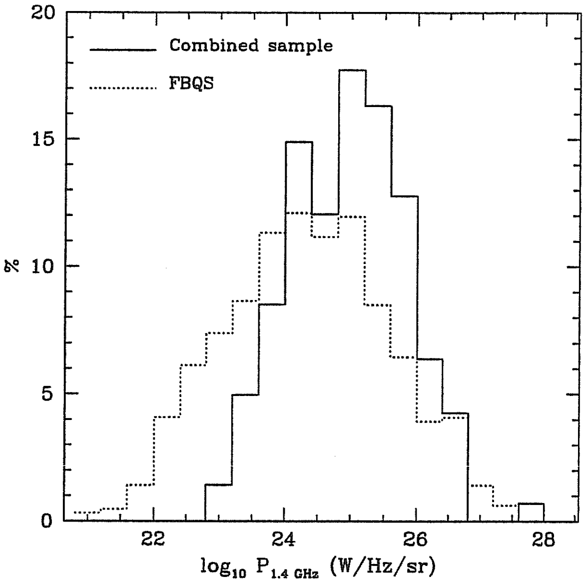

Figure 2.13: Distribution of radio powers for sources of the combined FIRST-2dF and FIRST-LBQS sample (solid line) and in the case of objects from the FBQS (dotted line).

from the joined use of the FIRST and Sloan Surveys. We believe their results to be highly biased by the cut both in flux and in magnitude, which preferentially excludes sources with low values of the radio-to-optical ratio and therefore generates an artificial gap in the distribution of radio-to-optical ratios for $\log_{10}R^*_{1.4} \lesssim 2.5$. In fact, the authors select objects in a region of the apparent magnitude-radio flux plane enclosed by lines perpendicular to the loci of constant radio-to-optical ratios (see their Figure 14). We argue that, in order to obtain an unbiased $R^*_{1.4}$ distribution, a weight should be applied to take into account optical number counts, since their steep rise for increasing magnitudes determines both a spurious detection of the apparent peak at large values of $R^*_{1.4}$ and a lack of sources with low radio-to-optical ratios.

No evidence for a "gap" is seen even if we use the radio-power $\mathrm{P_{1.4GHz}}$ as the parameter which separates quasars into radio-quiet and radio-loud ones. We remind here that the assumption for a bimodal distribution as expressed above would in fact imply a deficit of sources at radio luminosities $\log_{10}\mathrm{P_{1.4GHz}} \sim 24.5$ (W $\mathrm{Hz^{-1}sr^{-1}}$) (assuming a spectral index $\alpha_R = 0.8$). The absence of a gap at $\log_{10}\mathrm{P_{1.4GHz}} \sim 24.5$ is clearly shown in Figure 2.13. Again, the decline observed for $\log_{10}\mathrm{P_{1.4GHz}} \lesssim 24$ (W $\mathrm{Hz^{-1}sr^{-1}}$) is due to

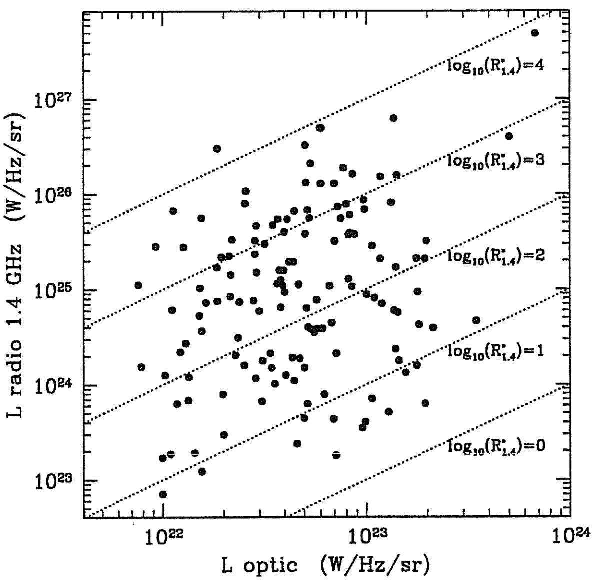

Figure 2.14: Optical luminosity versus radio power for sources in the combined FIRST-2dF and FIRST-LBQS sample. The dotted lines are the loci of constant radio-to-optical ratio.

the lack of low-power sources in our sample caused by the 1 mJy completeness limit of the FIRST survey (see Fig. 2.7). Note that a very similar trend is obtained for quasars from the FBQS (dotted line in Figure 2.13). Because of the broader redshift range spanned by this survey (different selection criteria allow to also detect low – $z \leq 0.35$ – redshift quasars), the FBQS can provide a better coverage of the faint end of the radio power distribution, even though the 1 mJy limit once again determines the decline of the distribution at low – $\log_{10} \mathrm{P}_{1.4\mathrm{GHz}} \leq 23.5$ (W Hz^{-1}sr^{-1}) – radio powers. It is nevertheless clear that none of the two distributions hints to the presence of a gap for $\log_{10} \mathrm{P}_{1.4\mathrm{GHz}} \sim 24.5$ (W Hz^{-1}sr^{-1}), i.e. to a bimodal distribution for the quasar population.

An alternative way to look at this result is to consider the distribution of radio powers for the objects in our sample as a function of their optical luminosities. As Figure 2.14 shows, the coverage of the $\mathrm{L}_{\mathrm{radio}}$- $\mathrm{L}_{\mathrm{optic}}$ plane is homogeneous, and the transition from those objects defined as "radio-loud" to those belonging to the "radio-quiet" population extremely smooth. Again, no gap is present, implying a continuous variation in the radio properties of quasars. This is in agreement with e.g. what found by Lacy et al. (2001) from the analysis of sources in the FBQS.

As a final remark, we note (see Figure 2.14) that there is no tight relationship between radio power and optical luminosity for the objects in our combined sample, since sources with a particular luminosity $L_{\rm optic}$ can be endowed with radio powers spanning up to three orders of magnitude. The above result suggests that the radio properties of quasars are not related to the mass of the central black hole. In fact, in the case of quasars it has been shown that the optical emission is reasonably well related to the bolometric one (Elvis et al. 1994). If we assume that these bright quasars are emitting close to the Eddington limit, the bolometric luminosity can in turn be connected to the mass of the central black hole. Since we find a very large spread in the relation between radio and optical luminosity, it seems unlikely that the mass of the central black hole is the main factor in determining the level of radio emission.

2.6 Conclusions

We have presented a new sample of radio-emitting quasars, obtained by matching together objects from the FIRST and 2dF Quasar Redshift Surveys. The dataset includes 113 quasars, found within the redshift range $0.3 \leq z \leq 2.2$, with optical magnitudes $18.25 \leq b_J \leq 20.85$ and radio fluxes at 1.4 GHz $S \geq 1$ mJy.

This sample has then been combined with the FIRST-LBQS catalogue (Hewett et al. 2001) in order to provide an almost-complete coverage of the optical luminosity-redshift plane and increase the statistical significance of our results. The main conclusions deriving from the joined analysis of the two samples can be summarized as follows:

1. The properties of radio-emitting quasars, such as their redshift distribution and $b_j - r$ colours, are in full agreement with those derived for the quasar population as a whole. This suggests the fueling mechanism(s) responsible for the birth, colour and life-time of quasars to be independent of the level of radio emission.
2. The fraction of radio detections decreases for fainter apparent magnitudes. This is also true if one considers the intrinsic luminosity of the sources, as the fraction of radio detections is found to grow from $\lesssim 3\%$ at $M_B \sim -24$ up to 20-30 % for the brightest ($M_B \sim -28$) objects.

3. The classical radio loud/radio quiet dichotomy, in which the distribution of radio-to-optical ratios and/or radio luminosities shows a "gap", has been ruled out by our analysis. We found no lack of sources neither for $R^*_{1.4} \sim 30-40$ nor for $\log_{10} \mathrm{P}_{1.4\mathrm{GHz}} \sim 24$ W Hz^{-1} sr^{-1}. Due to the selection effects – in particular the 1 mJy radio flux limit of the FIRST survey – we could not explore the low-P/low-R^* regions of the distributions. However, at least in the observed ranges, it is suggestive of a smooth transition from the radio-loud to the radio-quiet regime.

4. We find no tight relationship between radio and optical luminosity for the sources in our sample. For a given optical luminosity the scatter in the radio power is found to be more than three orders of magnitude. This result can give us some insight on the physical quantities responsible for the radio emission. In fact – since in the case of quasars the optical emission is reasonably well related to the bolometric one (Elvis et al. 1994), the bolometric luminosity (under the assumption that quasars emit close to the Eddington limit) can in turn be connected to the mass of the central black hole – such a large scatter tends to exclude the mass of the central black hole as the relevant quantity which controls the level of radio activity.

It is clear that the above results – especially those concerning the radio-quiet/radio-loud dichotomy – need further investigation. While awaiting for wide-area surveys able to probe the low radio-power/low radio-to-optical ratio regime, in the next Chapter the nature and behaviour of the radio emission of quasars will be investigated through Monte Carlo simulations.

Chapter 3

Is there a Dichotomy in the Radio Loudness Distribution of Quasars ?

3.1 Introduction

As discussed in previous Chapter, the uncertainties on the presence of a dichotomy, the character of radio loudness and the consequent poor knowledge of its origin (dependence on BH mass, optical luminosity etc.) are due to the analysis of different samples, often very inhomogeneous because of selection effects both in the optical and radio bands, i.e. the lack of a single sample covering all the ranges of optical and radio properties of quasars. Phenomenologically there are indications in RL objects of correlations between radio emission and luminosity in narrow emission lines, produced by gas presumably photoionized by the nuclear optical–UV continuum (e.g. Rawlings & Saunders 1991). Results from previous Chapter (see Cirasuolo et al. 2003a) show that, for a given optical luminosity, the scatter in radio power is more than three orders of magnitude. Note that if quasars are AGN accreting near the Eddington limit, this result tends to exclude the mass of the central BH as the main quantity controlling the level of radio activity (see also Woo & Urry 2002), although we cannot conclude anything on the possible presence of a threshold effect, whereby RL AGN would be associated to the more massive BH ($M_{\rm BH} > 1 - 5 \times 10^9 M_\odot$, Laor 2000, Dunlop et al. 2003, but see also Woo & Urry 2002 for a dissenting view). On the other hand, although controversial, there is some evidence for the fraction of RL quasars to increase with increasing optical luminosity (Padovani 1993; La Franca et al. 1994; Hooper et al. 1995; Goldschmidt et al. 1999; Cirasuolo et al. 2003a; but see also Ivezic et al. 2002 for a different view).

Therefore, in order to shed light on this issue, we adopted the alternative approach of starting from simple assumptions on the intrinsic properties of the quasar population as a whole – namely an optical quasar luminosity function and a prescription to associate a radio power to each object - and, through Monte Carlo simulations, generate unbiased quasar samples. By applying observational limits in redshift, apparent magnitude and radio flux we can then compare the results of the simulations with the properties of observed samples. The aim of this approach is of course twofold: constrain the initial hypothesis on the intrinsic nature of quasars, by requiring properties of the simulated samples – such as $R^*_{1.4}$ and radio power distributions, fraction of radio detections etc. – to be in agreement with the observed ones; test the effects of the observational biases on each sample by simply changing the observational limits.

The layout of the Chapter is the following. In Section 2 we briefly present the samples used to constrain the models, while in Section 3 we describe the procedures adopted to generate simulated samples. In Section 4 results of the simulations and comparisons of the properties of the observed and simulated samples are shown. We discuss the physical meaning of these results and summarize our conclusions in Section 5. Throughout this Chapter we will adopt the E.d.S. Cosmology (see Chapter 1).

3.2 The Datasets

As there is not (yet) a single sample able to cover, with enough statistics and completeness, the total range of known radio activity (e.g. the distribution of radio-to-optical ratios and/or radio powers), we have to consider various samples to constrain - as completely as possible - the properties of our simulated samples. We choose three samples of optically selected quasars, namely the 2dF Quasar Redshift Survey (2dF), the Large Bright Quasar Survey (LBQS) and the Palomar Bright Quasar Survey (PBQS). These have in fact a high completeness level and are quite homogeneous since all of them are optically selected in the blue band and have a similar radio cut. The 2dF and LBQS have been cross-correlated with the FIRST survey with a limiting flux at 1.4 GHz of 1 mJy (see Chapter 2, Cirasuolo et al. 2003a, Hewett et al. 2001), while the PBQS has been observed at 5 GHz down to a limiting flux of 0.25 mJy (Kellermann et al. 1989), which is comparable to the 1 mJy flux limit at 1.4 GHz, for a typical radio spectral index $\alpha_{\rm R} = 0.8$. Equally crucial for our work is the fact that these samples produce a very large coverage of the optical luminosity-redshift plane and provide information on different regimes of radio activity (see Fig.3.1).

In order to have complete homogeneity and favour the comparison with simulations, for each sample we have only considered the ranges in redshift, apparent magnitude and radio flux with the highest completeness. We have also selected sources with $M_{\rm B} \leq -23$ to avoid contaminations from the host galaxy light (Croom et al. 2001; Cirasuolo et al. 2003a) and we have applied a mean correction of 0.07 mag to convert $b_{\rm J}$ to B magnitudes (see previous Chapter), on the basis of the composite quasar spectrum compiled by Brotherton et al. (2001). The same composite spectrum has also been used to compute the K-correction in the B band.

Samples from 2dF and LBQS have been extensively described in previous Chapter. The sample resulting from the cross-correlation of 2dF and FIRST is constituted by 113 objects, with optical magnitudes $18.25 \leq b_{\rm j} \leq 20.85$ and radio fluxes at 1.4 GHz $S_{\rm 1.4GHz} \geq$ 1 mJy, over an effective area of 122.4 square degrees. In the following we consider only the sub-sample (hereafter called the FIRST-2dF sample) containing 89 objects with absolute magnitudes brighter than $M_{\rm B} \leq -23$ spanning the redshift range $0.35 \leq z \leq 2.1$.

For homogeneity with the FIRST-2dF, out of the sample obtained from the LBQS we have only considered 58 sources with apparent magnitudes $16 \leq b_{\rm j} \leq 18.8$ and redshifts $0.2 \leq z \leq 2.2$, all of them with $M_{\rm B} \leq -23$ (hereafter called the FIRST-LBQS sample).

3.2.1 Palomar Bright Quasar Survey

We have also considered the Palomar Bright Quasar Survey (Schmidt & Green 1983), which represents one of the historical and most studied sample of quasars, in order

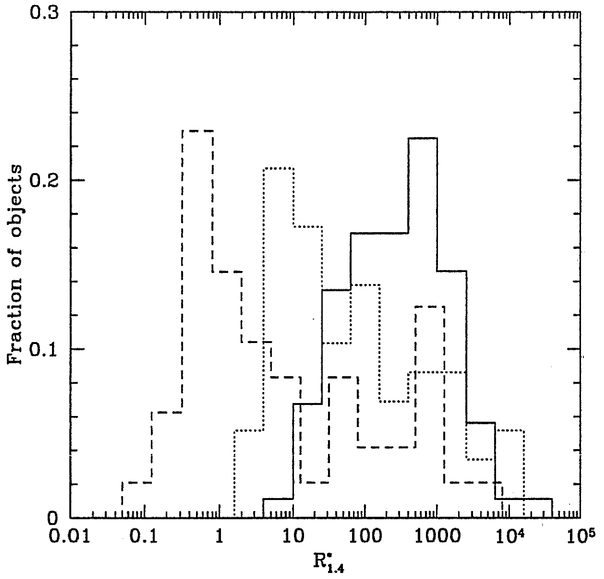

Figure 3.1: Distributions of the radio-to-optical ratios for the three samples: FIRST-2dF (solid line), FIRST-LBQS (dotted line) and PG (dashed line)

to cover the very bright end of the absolute magnitude distribution. It contains 114 objects brighter than an effective limiting magnitude $B = 16.16$, selected over an area of 10,714 square degrees using the UV excess technique. Such quasars have been observed using the VLA at 5 GHz with 18 arcsec resolution, down to a flux limit of 0.25 mJy (4σ) (Kellermann et al. 1989). In order to reduce, as much as possible, the contamination due to the host galaxy, we have chosen not to consider the very local sources with redshift $z < 0.1$. Our choice is also justified by the fact that all these objects are classified as "galaxy" in the NED archive (NASA/Ipac Extragalactic Database), indicating that the host galaxy is clearly visible. Again, for homogeneity with the former datatsets, from this sample we have only selected objects with $13 \leq B \leq 16.16$, in the redshift range $0.1 \leq z \leq 1.5$, with $M_{\rm B} \leq -23$ and radio flux $S_{\rm 5GHz} \geq 0.25$ mJy, ending up with a sub-sample of 48 radio sources (hereafter called the PG sample).

3.3 Monte Carlo Simulations

As already mentioned, selection effects – both in radio and optical bands – can introduce severe biases in the observed radio properties of quasars. Therefore, our approach is to start from simple assumptions on the intrinsic features of the quasar population and test them by comparing results from simulated samples – generated through Monte Carlo realizations – with those of the observed samples. We decided to assume as the two fundamental ingredients to describe the quasar population a well defined Optical Luminosity Function (OLF) - from which to obtain redshift and optical magnitude for the sources - and a distribution of radio-to-optical ratios which provides each source with a radio luminosity. Here we briefly specify these assumptions and describe the procedure applied in our Monte Carlo simulations.

3.3.1 Optical Luminosity Function

The best determined OLF for the whole quasar population currently available is the one obtained from the 2dF Quasar Redshift Survey (Boyle et al. 2000; Croom et al. 2001), based on $\sim 11,000$ sources. This can be described as a broken power-law (Croom et al. 2001)

$$\phi(M_{\rm B}, z) = \frac{\phi^*}{10^{0.4[C(z)(\alpha+1)]} + 10^{0.4[C(z)(\beta+1)]}}, \tag{3.1}$$

with $\alpha = 3.28$, $\beta = 1.08$, $C(z) = M_{\rm B} - M^*_{\rm B}(z)$, where sources undergo a pure luminosity evolution parametrized by the expression

$$M^*_{\rm B}(z) = M^*_{\rm B}(0) - 2.5(k_1 z + k_2 z^2), \tag{3.2}$$

with $k_1 = 1.41$, $k_2 = -0.29$ and $M^*_{\rm B}(0) = -21.45$. One of the main advantages of using this luminosity function is that it has been obtained in the B band and over the wide redshift range $0.35 \leq z \leq 2.2$, therefore reducing the need for extrapolations, which would add further uncertainties. Some extrapolation is instead needed for the bright end of the luminosity function ($M_B \lesssim -27$), which is not well sampled by the available data. Adopting the above OLF we have then randomly generated sources, over redshift and apparent magnitude ranges necessary to compare them with each of the three samples.

Note that, we have used the Optical LF as a description of the key quasar properties and number density mainly because we are going to compare our results with samples of optically selected quasars. In a more general picture one should also include the contribution to the quasar population given by the obscured (type II) QSO. To this aim it would be plausibly more appropriate to use a hard X-ray LF, which however so far has only been computed for type I objects (La Franca et al. 2002, Ueda et al. 2003) and which thus results to be similar in shape and evolution to the one determined in the soft X-ray band (Miyaji et al 2000). We stress that, since the radio emission is not affected by obscuration, the contribution of type II quasars would affect our results (e.g. the distribution of radio-to-optical ratios) only if there was a dependence of the obscuration level on the quasar optical luminosity. However, as recent results (La Franca et al. 2002; Tozzi et al. 2001; Giacconi et al. 2002; Rosati et al. 2002) seem to suggest, the fraction of these obscured quasars is expected to be small when compared to the unobscured ones. The above conclusion implies that the presence of type II quasars should not significantly affect our findings and therefore we have decided to neglect their (uncertain) contribution.

3.3.2 Radio vs Optical Luminosity

The other ingredient needed for our analysis is a relation between optical and radio luminosities. As already concluded in Chapter 2, although present, this shows a wide spread: Figure 3.2 illustrates – for the objects in the three samples considered in this work – how sources with a particular optical luminosity can be endowed with radio powers spanning more than three orders of magnitude.

We have thus taken into account two (simple) different scenarios. The first one assumes a relation between radio and optical luminosity, although with a large scatter (Model A); in this case we use a distribution in $\log_{10}(R^*_{1.4})$ and compute the radio power as $\log_{10}(R^*_{1.4})+\log_{10}(L_{\rm opt})$. The second case describes the possibility for the radio luminosity to be completely unrelated to the optical one, and assumess a distribution in $\log_{10}(P_{1.4\,{\rm GHz}})$ for any given optical luminosity (Model B). For Models A and B respectively, we then consider different shapes for the distribution of radio-to-optical ratios and radio luminosities: a) the simplest case of a flat uniform distribution over the whole range of radio-to-optical ratios

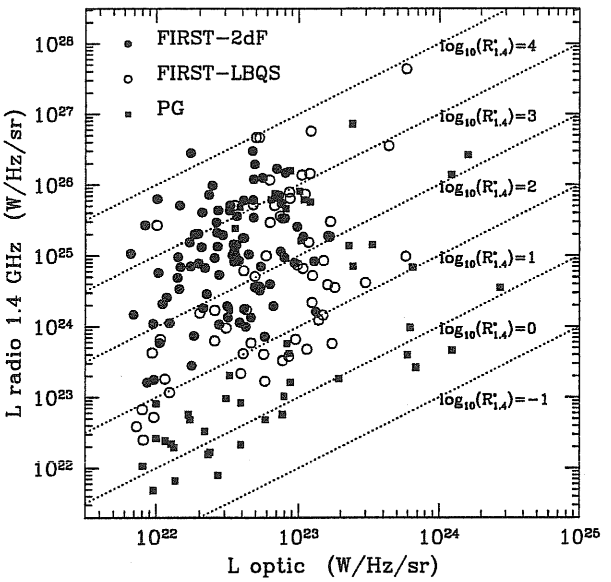

Figure 3.2: Optical versus radio luminosity for sources in the considered samples. The dotted lines are loci of constant radio-to-optical ratio.

or radio powers; b) a single Gaussian distribution, in which the RL regime could simply represent its tail; c) two Gaussians, the first peaked in the RL regime and the second in the RQ one, in order to allow for a more flexible shape of the distributions and test the hypothesis of bimodality.

As a final step, radio flux densities have been computed from radio powers by assuming 80 per cent of these sources to be steep spectrum ($\alpha_{\rm R} = 0.8$), while the others to be flat spectrum ($\alpha_{\rm R} = 0$) objects. These fractions have been chosen according to the results found in Chapter 2: although for the FIRST-2dF sample we only managed to compute the radio spectral index for the ten most luminous objects, roughly finding the same fraction of steep and flat spectra, the remaining sources do not have any counterpart at radio frequencies > 1.4 GHz, suggesting that most of the quasars have a steep spectrum. These assumed fractions are also in agreement with that of steep spectrum sources observed in the PG sample. It must be noticed that in these associations of a radio luminosity to each optical quasar there is a strong implicit assumption on the evolution, namely that radio and optical luminosities evolve in the same way. Even though we have no direct evidence, some hints supporting this hypothesis can be bound from the data. On one

z	Total	Radio
0.35 - 1	0.61 ± 0.01	0.58 ± 0.07
1 - 1.5	0.55 ± 0.01	0.53 ± 0.05
1.5 - 2.1	0.51 ± 0.008	0.50 ± 0.05

Table 3.1: Mean $V/V_{\rm max}$ values for the radio detected and the total quasar population from the 2dF sample as measured in three different redshift bins.

side in Chapter 2 it has been shown that the $R^*_{1.4}$ distribution, both for sources in the FIRST-2dF and in the FIRST-LBQS, is completely independent of redshift. This is not expected if radio and optical luminosities had significantly different evolutions. On the other side, an independent indication of such hypothesis is obtained from the $< V/V_{\rm max} >$ test, which we applied separately to radio detected objects (from the FIRST-2dF) and to quasars representative of the population as a whole (from the total 2dF). For objects in the radio sample we computed $V_{\rm max}$ by using the maximum redshift at which a source could have been included both in the radio and in the optical datasets, given the radio flux and optical magnitude limits. We considered three redshift bins and the results [1] are reported in Table 3.1. The values of $< V/V_{\rm max} >$ for the two populations are perfectly compatible in all redshift bins, even though the errors for the radio sample are larger due to the smaller number of objects. This again suggests the evolutionary behaviour of the radio detected and total populations to be similar, justifying our assumption.

3.3.3 Constraints from the data

Adopting each of the six models described in the previous section and applying the observational limits (reported for clarity in Table 3.2), we have simulated samples of radio emitting quasars. Comparisons with the FIRST-2dF, FIRST-LBQS and PG samples provide several constraints. In particular the simulated populations must reproduce the observed:

- distributions of radio-to-optical ratios and radio powers. The three samples identify different levels of radio activity: while the FIRST-2dF – which is the optically faintest

---

[1] The errors on the mean value of $< V/V_{\rm max} >$ have been computed as $(\sqrt{12\,N})^{-1}$, where N is the number of objects in each bin.

Survey	$N_{\rm QSO}$	$z_{\rm lim}$	$B_{\rm lim}$	$S_{\rm lim}$ (mJy)	Area (deg^2)
FIRST-2dF	89	$0.35 \le z \le 2.1$	$18.25 \le b_{\rm j} \le 20.85$	$S_{1.4\,{\rm GHz}} \ge 1$	122.4
FIRST-LBQS	58	$0.20 \le z \le 2.2$	$16.00 \le b_{\rm j} \le 18.80$	$S_{1.4\,{\rm GHz}} \ge 1$	270.0
PG	48	$0.10 \le z \le 1.5$	$13.00 \le B \le 16.16$	$S_{5\,{\rm GHz}} \ge 0.25$	10714.0

Table 3.2: Selection limits and covered areas for the surveys used in our analysis. $N_{\rm QSO}$ is the number of quasars with $M_{\rm B} \le -23$

– well traces the RL regime for $R^*_{1.4} \gtrsim 50$, the FIRST-LBQS is sensible to the RL-RQ transition and the PG is particularly suited to constrain the RQ regime (see Figure 3.1).

- fraction of radio detections. As shown in Figure 3.3, this fraction depends on the optical limiting magnitude of the survey: from $\sim$ 3 per cent for the optically faint sources (FIRST-2dF), to $\sim$ 20 per cent for objects with $B \sim 17$ (FIRST-LBQS) and up to 70 per cent or more at the brightest magnitudes (PG).

  Note that a similar dependence is also followed by the intrinsic luminosity, as the fraction of radio detections grows from $\lesssim 3$ per cent at $M_{\rm B} \sim -24$ up to 20-30 per cent for the brightest $M_{\rm B} \sim -28$ objects (Cirasuolo et al. 2003a; Padovani 1993; La Franca et al. 1994; Hooper et al. 1995; Goldschmidt et al. 1999).

- number counts, both in the radio and in the optical band.

- redshift and absolute magnitude distributions.

3.4 Results

Monte Carlo simulations have been run exploring the widest range of values for the free parameters – which describe the distributions of radio-to-optical ratios (Model A) or radio powers (Model B) – in order to find all the sets of values able to reproduce the data. We have used simulated samples with a hundred times more objects than the original datasets and the realizations have been repeated with different initial seeds, in order to minimize the errors on the simulated quantities. We tested the validity of each model by

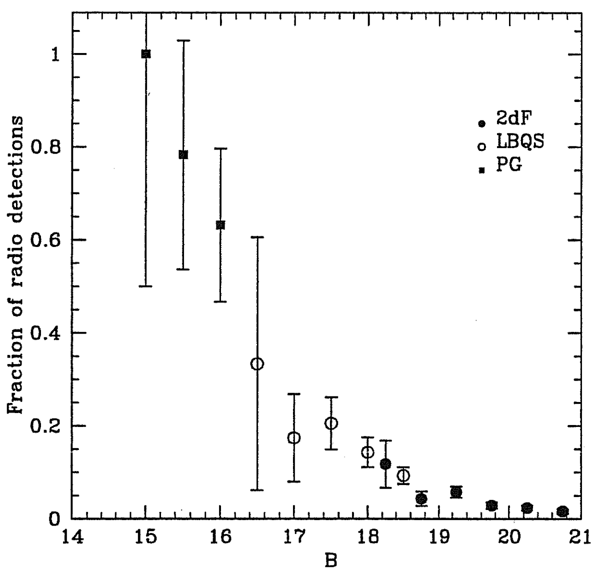

Figure 3.3: Fraction of quasars with a radio counterpart in the three samples as a function of the apparent optical magnitude.

comparing the properties of simulated and observed samples through statistical tests: a Kolmogorov-Smirnov (KS) test for the $R^*_{1.4}$ and radio power distributions, and a χ^2 test for the fraction of radio detections as a function of apparent and absolute magnitude, and also for the optical and radio number counts.

3.4.1 Results for flat and single Gaussian distributions

We find that the simplest model, a flat distribution, is totally inconsistent with the data and rejected by the statistical tests, both for Model A and B. In particular it is unable to reproduce the observed number counts for the three samples simultaneously: the data, in fact, require the number of RL quasars to be less than the RQ ones, while this distribution spreads objects uniformly.

We then tested the single Gaussian distribution, which also fails, for both Model A and B, mainly because it is unable to simultaneously reproduce the observed distribution of $R^*_{1.4}$ in the RL regime and the total number of objects in the three samples.

x_1	σ_1	x_2	σ_2	Fraction
2.7 ± 0.2	0.7 ± 0.2	-0.5 ± 0.3	0.75 ± 0.3	97 ± 2 per cent

Table 3.3: Best fit parameters for Model A, expressed in $\log_{10} R^*_{1.4}$. x_1 and σ_1 are the center and dispersion of the Gaussian in the RL regime, while x_2 and σ_2 are those for the Gaussian in the RQ one. "Fraction" indicates the percentage of objects having radio-to-optical ratios described by the second Gaussian. Errors have been obtained as explained in Section 3.4.2

3.4.2 Results for the two-Gaussian distribution

Given the above difficulties, we considered the more flexible model of two Gaussians, respectively centered in the RL and RQ regions. As said, each one of the considered samples traces different radio regimes: in particular the FIRST-2dF sample well constrains the shape of the distribution at high $R^*_{1.4}$, and also – through the number counts – well determines the fraction of objects with high levels of radio emission. As a consequence, the parameters of the first Gaussian (center x_1 and dispersion σ_1) and the relative fraction of objects in the two Gaussians are mainly determined by this sample. The other two samples constrain parameters of the second Gaussian in the RQ regime: the PG sample mainly determines its peak position; the FIRST-LBQS sample – which traces the transition region between RL and RQ – constrains quite well the shape of the wing of the second Gaussian and its overlap with the first one.

- Model B. In this case, i.e. radio luminosity completely unrelated to the optical one, no set of parameters has been found able to satisfy the statistical tests for all the observed quantities. In particular, this model is not able to predict the growing fraction of radio detections as a function of both apparent and absolute magnitudes, and to reproduce in a satisfactory way the shapes of the radio-to-optical ratio distributions simultaneously in the case of FIRST-2dF and FIRST-LBQS.

- Model A. A promising solution has been found in this case, namely by assuming radio and optical luminosities to be related even though with a large scatter. The radio-to-optical ratio and radio power distributions corresponding to this solution are displayed in Figure 3.4 and the model parameters are given in Table 3.3. A comparison

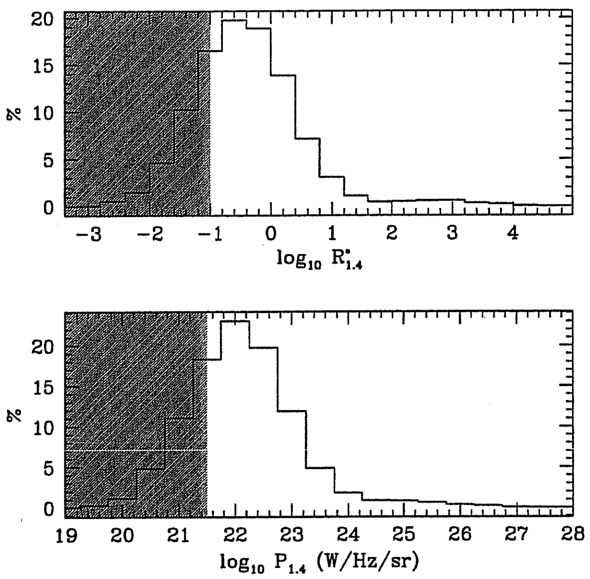

Figure 3.4: Distribution of radio-to-optical ratios (top panel) and of radio powers (bottom panel) obtained from the best-fit set of parameters of Model A (see Table 3.3). The distributions are plotted in binned form and the shaded regions indicate the range of $R^*_{1.4}$ and $P_{1.4}$ for which no data are available.

between the properties of observed and simulated samples is shown in Figures 3.5, 3.7 and 3.8. We find a good agreement with the $R^*_{1.4}$ and radio power distributions of the FIRST-2dF and FIRST-LBQS samples (high KS probabilities, from 0.2 up to 0.9, for the distributions in Figure 3.5). The simulated dataset is also able to reproduce the observed fraction of radio detections, both as a function of apparent and absolute magnitudes (with a significance level for the χ^2 test > 0.05 see Figure 3.7) and the number counts, except for a tendency – consistent within the errors – to over-estimate the FIRST-2dF and correspondingly under-estimate the FIRST-LBQS counts (see Figure 3.8).

However, substantial disagreement is found for the $R^*_{1.4}$ and radio power distributions when compared to the observed quantities in the PG sample (KS probabilities $< 10^{-2}$). The discrepancy is mainly due to the presence in this sample of ~ 10 objects with high values of $R^*_{1.4}$ ($\gtrsim 100$), which also determine the different shape of the radio number counts (see Figure 3.8). We stress that we found no solution compatible with both

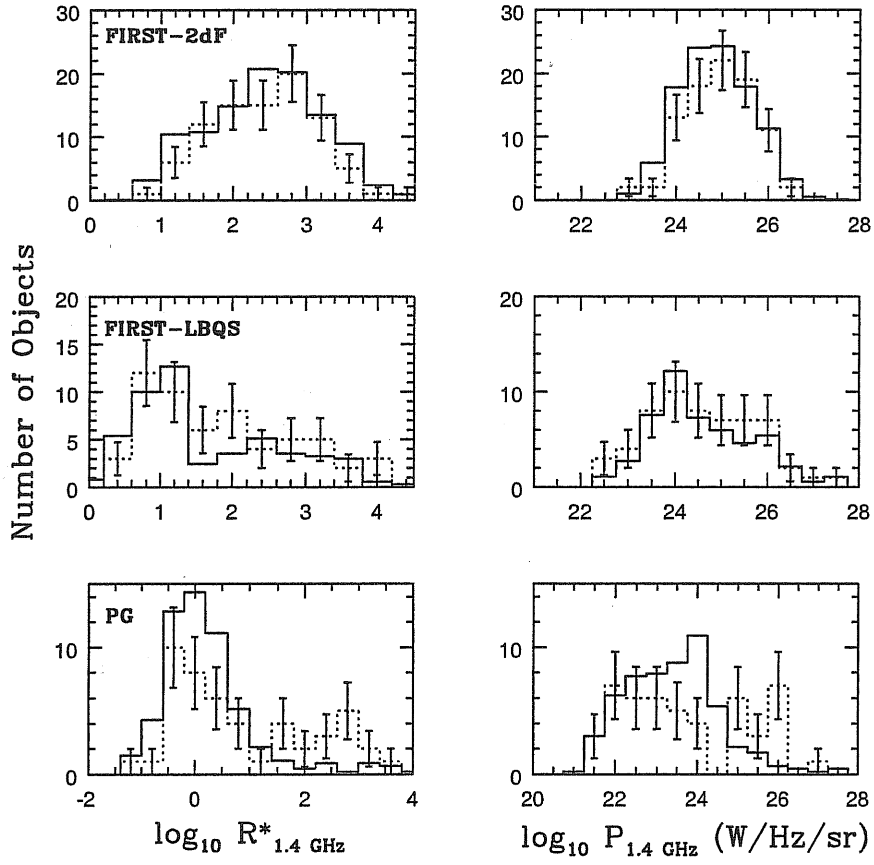

Figure 3.5: Comparison between the observed (dotted lines) and the predicted (solid lines) distributions of radio-to-optical ratios (on the left) and radio powers (on the right) for the three samples. Error-bars on the observed distributions are derived by assuming a Poissonian distribution.

the PG and the other two samples: the excess of RL sources in the PG dataset is in fact inconsistent with the both FIRST-2dF and FIRST-LBQS samples. We therefore investigated in more details the properties of these $\sim$ 10 PG sources, by looking at their radio and optical-to-X-ray spectral indices and the compactness of the radio emission. We found the properties of these quasars to be completely indistinguishable from those of other objects in the PG sample, except for a slightly different redshift distribution (these RL quasars are mainly concentrated in the range $0.3 \leq z \leq 0.5$) and (by definition) their high $R^*_{1.4}$. We notice however that it has been shown that the PG sample is incomplete (Goldschmidt et al. 1992) and it has also been suggested this incompleteness not to be random with respect to the radio properties (Miller, Rawlings & Saunders 1993; Goldschmidt et al. 1999).

In order to test this hypotesis, we studied the radio properties of a sample of quasars having the same characteristics of the PG sample. For this purpose we used the recent Asiago-ESO/RASS QSO Survey (AERQS) presented in Grazian et al. (2000, 2002). The sample of local quasars ($z \lesssim 0.2$) selected from this survey, contains bright sources ($12.6 \lesssim b_j \lesssim 15.13$), comparable with the PG sample. We have cross-correlated this sample with the FIRST survey and the resulting $R^*_{1.4}$ distribution is shown in Figure 3.6. Sources in the AERQS sample show a $R^*_{1.4}$ distribution with a peak at $R^*_{1.4} \sim 0.3$ and no objects with $R^*_{1.4} \gtrsim 100$, as predicted by our model (see lower-left panel in Figure 3.5). Therefore, we are more confident that the FIRST-2dF and FIRST-LBQS are better suited to represent the shape of the $R^*_{1.4}$ distribution, at least in the RL regime. Due to these problems with the PG sample, we have therefore not considered the constraints on the $R^*_{1.4}$ and radio power distributions for this sample, converging to the same best fit model as discussed before.

As a further test we have looked at the redshift and absolute magnitude distributions. The comparison between data and model predictions is shown in Figure 3.9, which reveals an excellent agreement in the case of the FIRST-2dF sample. A worse accordance has been found for the other datasets, even though the simulated vs. observed distributions are still compatible within the errors. The simulated samples (in these

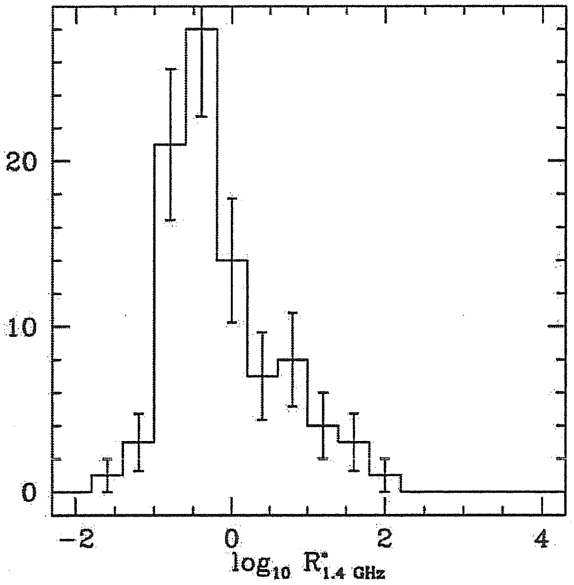

Figure 3.6: $R^*_{1.4}$ distribution for sources in the AERQS (Grazian et al. 2000, 2002) having a counterpart in the FIRST survey.

two cases) reveal a tendency to overproduce objects at bright ($M_B \lesssim -27$) absolute magnitudes, probably due to the extrapolation of the bright end of the luminosity function (see Section 3.3.1). However, we want to stress that this effect cannot explain the disagreement in the $R^*_{1.4}$ and radio power distributions found for the PG sample. In fact, those RL sources found to be in excess with respect to the expectations – and clearly visible in the redshift bin at $z \sim 0.4$ – have absolute magnitudes $-25 \lesssim M_B \lesssim -26$, a range in which the OLF is well defined.

Note that the above results have been obtained by relaxing the constraints for the PG sample only on the $R^*_{1.4}$ and radio power distributions, while still considering in the analysis the observed total number of objects and the fraction of radio detections: in fact, by completely eliminating this sample we would loose important and robust constraints on the RQ regime.

Finally we evaluate the ranges of acceptable parameters by varying their best fit values until one of the constraints (e.g. $R^*_{1.4}$ and radio power distributions, fraction of radio detections, etc.) was no longer satisfied with respect to the KS and/or χ^2 tests. We

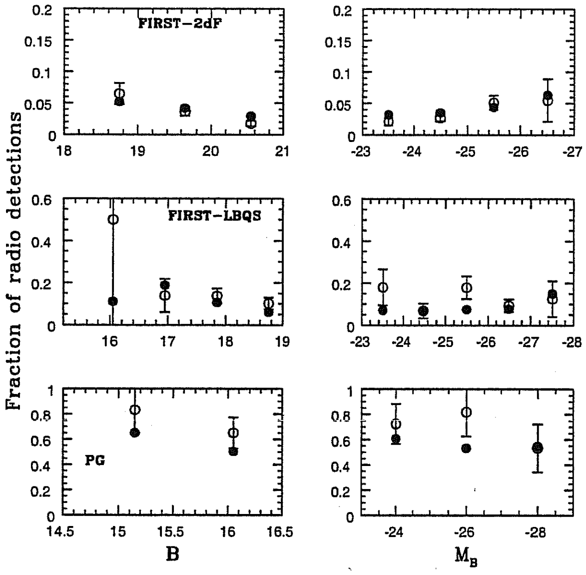

Figure 3.7: Comparison between the observed (open circles) and the predicted (solid dots) fraction of radio detections for the three samples, as a function of the apparent and absolute magnitudes.

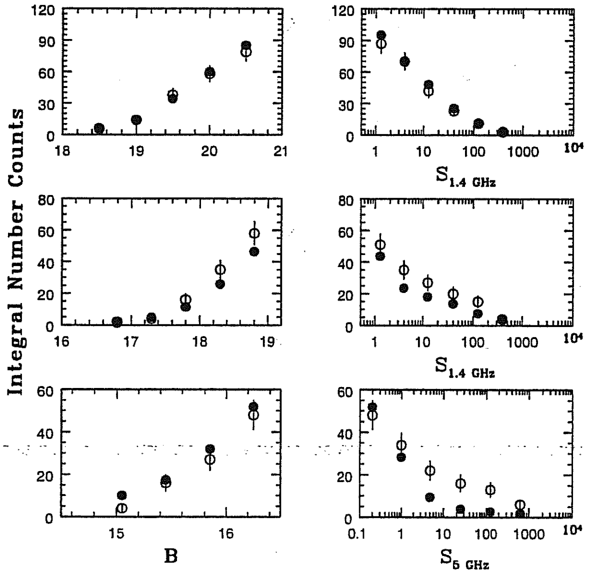

Figure 3.8: Comparison between the observed (open symbols) and predicted (dolid dots) optical and radio integral number counts.

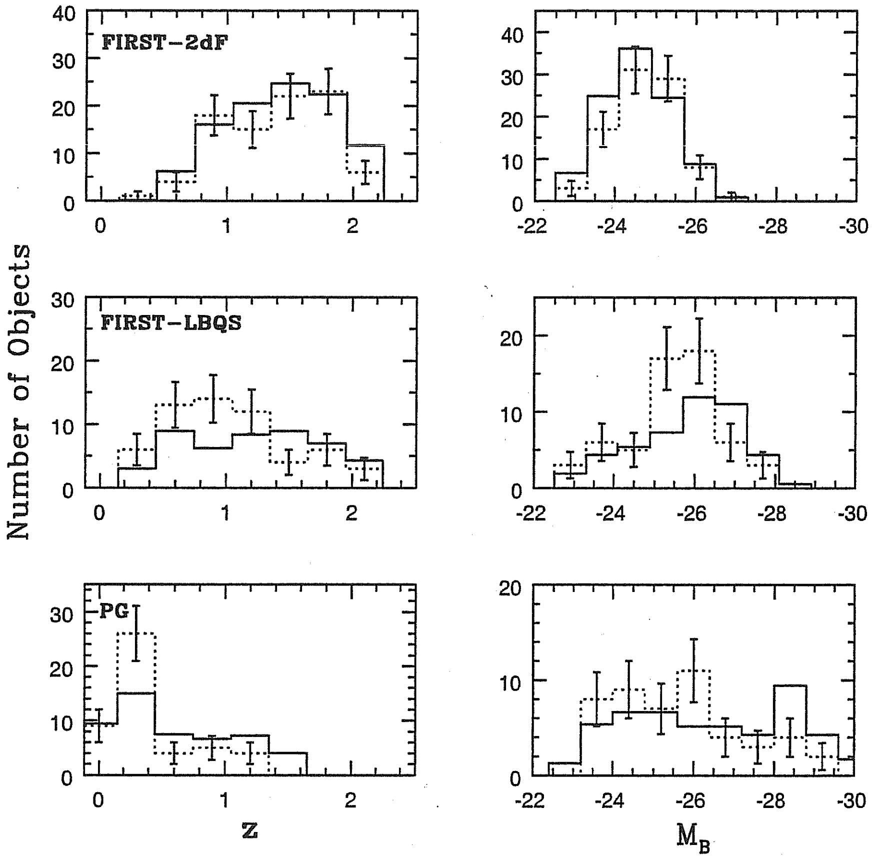

Figure 3.9: Comparison between the observed (dotted lines) and expected (solid lines) distributions of redshift (on the left) and absolute magnitude (on the right).

adopted, as acceptable limits, a probability of 0.1 for the KS test and a confidence level of 0.05 for the χ^2 test. In this way we obtained a reference error estimate on the parameters which is given in Table 3.3.

3.5 Discussion

The first point worth stressing is the "uniqueness" of the solution found. The combination of all the observational constraints is very cogent and thus we find that only one solution in the whole is able to simultaneously reproduce measurements from the three surveys. Furthermore, the uncertainties associated to the various parameters are in this case relatively small (see Table 3.3).

It is also intriguing to notice that a simple prescription for the distribution of the radio-to-optical ratios is able to well reproduce all of the available observational constraints given by three different samples. It is important to remark here that in order to reproduce the data we need a dependence of the radio luminosity on the optical one, even though with a large scatter. This is proved by the fact that Model B – where the two luminosities are completely unrelated – is rejected by the statistical tests. In particular, the successful model accounts for the dependence of the observed fractions of radio detected quasars on apparent and absolute optical magnitudes, as due to selection effects: going to optically fainter magnitudes (at a fixed radio flux limit) corresponds to selecting increasingly more RL objects. According to the model the intrinsic fraction of RL is small ($\lesssim 5$ per cent) when compared to the total population, and this e.g. explains the small fraction of radio detected quasars observed in the 2dF sample. Since the shape of the $R^*_{1.4}$ distribution (see Figure 3.4) is steep for $1 \lesssim R^*_{1.4} \lesssim 10$, surveys with brighter optical limiting magnitudes which select smaller values of $R^*_{1.4}$ (at a given radio flux) will then result in more and more radio detections. Similarly, the radio-optical dependence accounts for the flattening of the faint end of the optical luminosity function of RL quasars with respect to that of the whole population (La Franca 1994; Padovani 1993; see also Chapter 4).

Given the uniqueness of the solution, the main result of this work is indeed the fact that we can put rather tight constraints on the intrinsic radio properties of quasars. The distributions shown in Figure 3.4 could then describe the unbiased view of the properties of the whole quasar population and this might possibly help us to understand the physical mechanism(s) responsible for the radio emission. First of all, in the $R^*_{1.4}$ distribution we note no lack or deficit of sources between the RL and RQ regimes: the distribution has a peak at $R^*_{1.4} \sim 0.3$ and decreases monotonically with a small fraction ($\lesssim 5$ per cent) of objects which are into the RL regime and represent a long tail of the total distribution. This result contrasts (see also Cirasuolo et al. 2003a) the view of a RL/RQ dichotomy where a gap separates the two populations. Nevertheless we can still talk about a "dichotomy" in the sense that the data are compatible with an asymmetric distribution, with a steep transition region and with only a small fraction of sources having high values of $R^*_{1.4}$.

Then the basic questions are still open: do all sources belong to the same population? Or better: is there a single mechanism producing the radio emission in quasars or two different processes dominate in the bulk of the population and in the high $R^*_{1.4}$ tail? While it is believed that the radio emission in powerful radio quasars is produced in well collimated jets (related to accretion processes), it is not clear what is its origin in radio weaker and RQ sources. Let us then consider some of the possible interpretations.

First of all it is known that, because of relativistic beaming, the orientation of the source plays a leading role at least in the RL regime – although this could not account for the lack of large scale radio structures in RQ sources. In fact, relativistic boosting could push up by typically a factor of $10^3 - 10^4$ the observed radio emission (and correspondingly $R^*_{1.4}$ if the optical emission is dominated by thermal radiation). In this case we would expect at least the extreme RL sources to be flat spectrum, which is not supported by observations. A large fraction of the RL sources in the PG sample have a steep spectrum, and the same behaviour has been suggested for RL objects from the FIRST-2dF sample (Cirasuolo et al. 2003a). Also well studied datasets of radio selected quasars, from the 2-Jy (Wall & Peacock 1985) and the 1-Jy samples (Stickel et al. 1994), show the distribution of radio-to-optical ratios to be the same for flat and steep spectrum radio quasars. However, this result could be affected by variability because of the non simultaneous radio flux measurements at different frequencies.

It has been proposed that the radio emission in RQ quasars is supplied by "starburst" phenomena, i.e. thermal emission from supernova remnants in a very dense environment (Terlevich et al. 1992). Alternatively, the radio flux could be associated to non-thermal emission from jets/outflows. In both cases we could reduce the presence of a dichotomy to the capability of the central engine to create a powerful/collimated jet. This in turn translates into the quest for identifying the parameter(s)/physical condition(s) responsible for its presence in only a few per cent of the sources.

As already mentioned, recent studies suggest the mass of the central BH not to be tightly related to the radio emission (Cirasuolo et al. 2003a; Woo & Urry 2002), except for a possible threshold effect (Dunlop et al. 2003) which however has been recently questioned (Woo & Urry 2002). Also, radio loudness does not seem related to the properties of the host galaxy and of the environment (Dunlop et al. 2003), even though the latter claim is still debated. A further key physical parameter for the nuclear activity is the mass accretion rate: however it appears reasonable to assume that this is close to the Eddington limit for all powerful optical quasars. Still open possibilities instead include the hypothesis that the creation of a jet is related to a threshold in the BH spin or to the intensity and configuration of the magnetic field in the nuclear regions.

A clue on the origin of radio emission comes from the radio imaging at high resolution (pc scales) of RQ quasars, which revealed the presence of non–thermal emission from jet-like structures, even for objects with low ($R^*_{1.4} \sim 1$) radio loudness (Kukula et al. 1998; Blundell & Beasley 1998). In many objects double or triple radio structures on scales of a few kiloparsecs have been resolved. Moreover, the inferred high brightness temperatures ($T_B > 10^6 K$) suggest that the radio emission cannot be produced by a starburst. Then jets could be a common feature in quasars and the radio power level could be due to distributions in some of the jet properties, which however have to present a 'threshold' effect to reproduce the fast RQ/RL transition and RL tail. These properties could of course include the jet power or the efficiency of conversion of the jet energy into radiation. It has been suggested (Rawlings & Saunders 1991) that in powerful radio sources the power released into the jet is comparable to the accretion one. This would imply a radiative efficiency (in the radio band) of only about 0.1 - 1 per cent for RL quasars – and even less in RQ ones (Elvis et al.

1994).

As a final remark we notice that also time dependence/evolution could play an important role: different ignition and duration times for the mechanisms responsible for the optical and radio emission could explain the observed distribution of radio-to-optical ratios. To shed light on this issue, in next Chapter we will deal with the evolutionary properties of faint radio loud quasars.

Chapter 4

Faint radio–loud quasars: clues on their evolution

4.1 Introduction

Investigations of radio-emitting AGN can be of great help in tackling the evolution of nuclear activity (AGN) with cosmic time. In fact, as already proved by very early studies (Longair 1966), radio emission can be used as a clean tool, not affected by obscuration, to trace the AGN evolution.

One of the key studies on the evolution of both radio galaxies and radio quasars, was provided by Dunlop & Peacock (1990). The radio luminosity function (LF) of these populations was separately obtained for steep spectrum and flat spectrum sources, by means of several samples selected at 2.7 GHz with relatively bright flux limits (ranging from 0.1 to 2.0 Jy). This analysis confirmed the presence of a so-called 'redshift cut-off" for the population of flat spectrum sources (Peacock 1985), with a decline in comoving density of a factor ~ 5 between $z = 2$ and $z = 4$. Most intriguingly, their work provided the first evidence for a similar behaviour for the population of steep spectrum sources, both quasars and radio galaxies, making this decline a common feature for all powerful radio objects. The evolution of both populations was found to be satisfactorily described by a pure luminosity evolution (PLE) model, analogous to that found for optically selected quasars (Boyle et al.

1988; Boyle et al. 2000; Croom et al. 2004), as well as by a luminosity/density evolution model, which incorporates a negative density evolution at high redshifts.

In order to investigate the possible presence of a redshift cut-off in the AGN evolution, several searches for high redshift radio–loud quasars have been carried out in the last years. Shaver et al. (1996, 1999) argued for a drop in space density of flat spectrum quasars by more than a factor 10 between $z \sim 2.5$ and $z \sim 6$. However, a reanalysis of such sources, taking into account spectral indices, showed that the evidence of the sharp decline in Shaver et al. work was not fully correct (Jarvis & Rawlings 2000; Jarvis et al. 2001). A luminosity dependent cut-off, with a space density decline less dramatic for the most luminous radio sources, has also been claimed by Dunlop (1998) from a recent update on the work by Dunlop & Peacock (1990).

The question of the redshift cut-off in the quasar evolution has also been addressed at other wavelengths. No evidence for a rapid decline of the quasar space density has been found for soft X-ray selected samples in the *ROSAT* survey at $z \gtrsim 2.5$ (Miyaji, Hasinger & Schmidt 2000). On the other hand, optical data from the Sloan survey (Fan et al. 2001b) suggest the space density of $\mathrm{M_{AB}}(1450\text{Å}) < -25.5$ quasars at $z \sim 4$ to be more than one order of magnitude lower than that found at $z \sim 2$ (Boyle et al. 2000). Recently, by using a sample of 13 optically luminous radio quasars, Vigotti et al. (2003) showed that their decline in the space density is about a factor of 2 between $z \sim 2$ and $z \sim 4$, significantly smaller than the value ~ 10 found for samples including lower luminosity objects (Fan et al. 2001).

However, the comparison with the behaviour of radio–selected sources hinges on the connection between the optical (X–ray) and radio activity. This is clearly of paramount relevance also with regards to the physical connection between the accretion processes and the jet formation. This aspect can be tackled from the comparison of the radio–loud and radio–quiet quasar populations.

The behaviour of steep/flat and galaxies/quasar radio sources is tightly connected within the framework of unification models (e.g. Padovani & Urry 1992, Urry & Padovani 1995, Jackson and Wall 1999). These rely on the fact that beaming effects and thus orientation play a key role in determining the observed properties of sources: BL Lac objects and flat spectrum quasars would be the beamed version – i.e. viewed at an angle close to the jet axis – of FRI and FRII radio galaxies (Fanaroff & Riley 1974), respectively. The behaviour of radio quasars is thus tightly related to that of the whole radio source population and in particular of powerful radio galaxies.

In the light of the above discussion the aim of the present Chapter is to estimate the low luminosity end of the LF of radio active quasars, both in radio and optical band, by taking advantage of the new final releases of the 2dF QSO Redshift and FIRST surveys. The aims are: i) to explore the cosmological evolution of the selected sources, ii) to examine the relation between the radio and optical activity and iii) the connection between quasars and radio galaxies.

The layout of the Chapter is as follows. In Section 2 we give a brief description of the new final releases of FIRST and 2dF Quasar Redshift Survey datasets used for our analysis and the matching procedure used to cross-correlate the catalogues. In Section 3 we describe the computation of the radio and optical luminosity functions and present our results, giving an assessment for incompleteness effects. Our findings are compared with other LFs already present in literature in Section 4. We discuss the results and summarize our conclusions in Section 5. For sake of comparison with previous works we will adopt $H_0 = 50$ km s^{-1}Mpc^{-1}, $q_0 = 0.5$ and $\Lambda = 0$ (hereafter cosmology I), even though we will also report our results on both radio and optical LFs within the "concordance" model, consistent with the Wilkinson Microwave Anisotropy Probe (WMAP) data (Bennett et al. 2003): $\Omega_m = 0.3$, $\Omega_\Lambda = 0.7$ and $H_0 = 70$ km s^{-1} (cosmology II).

4.2 The new FIRST-2dF sample

Recently, both FIRST (Faint Images of the Radio Sky at Twenty centimeters) survey and 2dF QSO Redshift Survey (2QZ) have recently been completed. The former survey contains 811,117 sources observed at 1.4 GHz down to a flux limit $S_{1.4\mathrm{GHz}} \simeq 0.8$ mJy, covering a total of about 9033 square degrees of sky (8422 square degrees in the north Galactic cap and 611 in the south Galactic cap). Also the 2QZ survey has recently been completed and in this Chapter we will refer to the final release (Croom et al. 2004). The final catalogue contains $\sim 21,000$ quasars with reliable spectra and redshift determinations, selected in the two declination strips (see Chapter 2).

4.2.1 Matching Procedure

Following procedures described in Chapter 2, we have matched objects from the FIRST and 2QZ surveys in the equatorial strip in the North Galactic cap. In the overlapping region – $9^h\ 50^m \leq$ RA(2000) $\leq 14^h\ 50^m$ and $-2.8° \leq$ Dec(2000) $\leq 2.2°$ – we found 10,110 optical quasars from the 2QZ. Over the same area, the total number of sources in the FIRST survey is $\sim 45,500$ down to a flux limit $S_{1.4\mathrm{GHz}} = 1$ mJy. As described in Chapter 2 (Cirasuolo et al. 2003a), for the matching procedure we used an algorithm to collapse multi-component sources (Magliocchetti et al. 1998): the algorithm collapses sub-structured sources into single objects having radio fluxes equal to the sum of the fluxes of the various components.

All the optical-radio pairs having an offset less than 2 arcsec have been considered as true optical identifications. The value of 2 arcsec as matching radius was chosen after a careful analysis as the best compromise to maximize the number of real associations (estimated to be ~ 97 per cent), and to minimize the contribution from spurious identifications down to a negligible 5 per cent (Magliocchetti & Maddox 2002). Furthermore, in order to verify the reliability of the associations, all the radio-optical pairs obtained from the collapsing algorithm were checked by eye on the FIRST image cutouts.

This procedure has lead to 352 quasars with good redshift determinations from the 2QZ and endowed with radio fluxes $S_{1.4\mathrm{GHz}} \geq 1$ mJy over an effective area of 284 square degrees. Of these sources, 113 have been already presented in Table A.1 (see Chapter 2), while the remaining 239 constitute an entirely new sample. The overall sample will be referred to as FIRST-2dF.

As discussed in Chapter 2, the reliability of the present sample has also been checked against quasars with a radio counterpart in the NVSS (Condon et al. 1998). The high resolution of FIRST (beaming size 5.4 arcsec) might in fact lead to a systematic underestimate of the real flux density in the case of extended sources. In order to assess the possible presence and entity of this effect, we have then compared FIRST and NVSS (beaming size of 45 arcsec) fluxes for all those sources in the sample which show a radio counterpart in both surveys. In the common 2QZ, FIRST and NVSS region, we only found 253 objects having an NVSS counterpart. All of these sources were also detected by our matching procedure and, as in Cirasuolo et al. (2003a), we found an excellent agreement between fluxes as measured by FIRST and NVSS. No correction to the flux densities derived from the FIRST survey was therefore applied. This also supported the validity of the collapsing algorithm.

About 40 per cent of the sources undetected by NVSS have $S_{1.4GHz} \geq 3$ mJy, i.e. above the flux limit of the survey ($\sim$ 3 mJy). This implies that such objects could have been lost in NVSS because of their multiple component structure.

4.2.2 Radio spectral index

Radio spectral indices α_R for a sub-sample of FIRST-2dF sources have been obtained by cross-correlating this dataset with the Parkes-MIT-NRAO (PMN) radio survey (Griffith et al. 1995). The PMN survey covers the equatorial zone ($-9.5° \leq$ Dec(2000) $\leq 10°$), observing objects at 4.85 GHz down to a flux limit of 40 mJy.

Due to its large beaming size, a matching radius of 3 arcmin has been used to cross correlate sources in the PMN with those included in our sample. Out of the 352 objects, we found counterpart for 52 in the PMN catalogue. Note that most of the sources indeed present matching radii $\sim$ 50 arcsec, as shown in the upper panel of Figure 4.1. Only a few of them have a larger offset, in any case smaller than 2 arcmin. This enables us to be reasonably confident that they are true associations.

The lower panel in Figure 4.1 shows the distribution of the radio spectral indices obtained. It is clear that the majority of the sources are flat spectrum quasars ($\alpha_R < 0.5$). This is due to the brighter flux limit ($S_{4.85GHz} = 40$ mJy) of the PMN survey with respect to FIRST. In fact, only bright steep spectrum ($\alpha_R \gtrsim 0.7$) sources with fluxes $S_{1.4GHz} \gtrsim 100$ mJy could have been detected by PMN, which therefore misses the majority of the steep spectrum objects in the FIRST-2dF sample. Out of 49 quasars in the FIRST-2dF sample with $S_{1.4GHz} \gtrsim 100$ mJy, we found 13 steep spectrum and 21 flat spectrum objects. The remaining 15 sources have been missed in the PMN survey due to the fact that it does not cover all

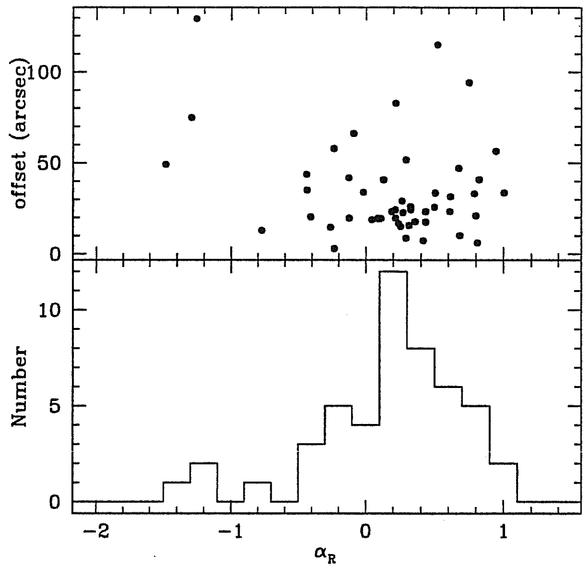

Figure 4.1: Top panel: radio spectral index for sources in the FIRST-2dF sample versus the offset between the positions in the FIRST and PMN surveys. The lower panel represents the distribution of the radio spectral indices found.

of the equatorial region, as it presents holes for $12^h \lesssim \mathrm{RA} \lesssim 16^h$.

4.2.3 The final sample

To summarize, the final FIRST-2dF sample is constituted by 352 objects with optical magnitudes $18.25 \leq b_J \leq 20.85$ and radio fluxes at 1.4 GHz $\mathrm{S}_{1.4\mathrm{GHz}} \geq 1$ mJy. All the 239 objects included in the FIRST-2dF sample and not present in Table A.1 (see Chapter 2) are listed in Table A.2 in Appendix.

4.3 Luminosity Functions

The larger size of the present sample with respect to the one presented in Chapter 2 (about a factor 3) enables us to obtain the LF of the population of radio detected quasars, both in the radio and optical bands.

In order to minimize incompleteness problems, we only considered sources with $\mathrm{S}_{1.4\mathrm{GHz}} > 2$, since the FIRST survey is 95 per cent complete at these flux levels. For the

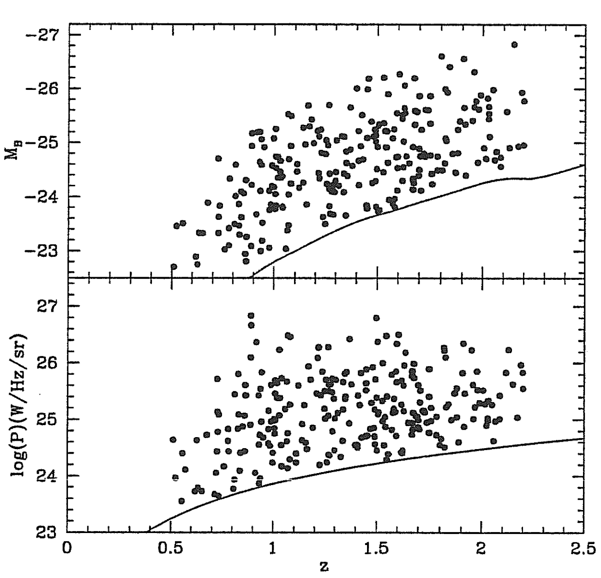

Figure 4.2: Redshift versus absolute $M_{\rm B}$ magnitude (top panel) and radio power at 1.4 GHz (lower panel) for sources in FIRST-2dF sample. The solid lines describe the selection effects respectively due to the limiting magnitude $b_{\rm J}$ = 20.85 and radio flux density $\rm S_{1.4GHz}$ = 2 mJy.

computation of the LFs we further confined the analysis to the redshift range $0.8 < z < 2.2$. The upper limit $z = 2.2$ is due to the drop of completeness at higher redshift of the 2dF QSO Survey (Croom et al. 2004). The choice of $z = 0.8$ as a lower limit is indeed related to the flux limits of both FIRST and 2dF surveys. As it is shown in Figure 4.2, faint sources – either in the optical or radio bands – are missed at high redshift due to selection effects. It follows that, in order to have a complete and unbiased coverage of both $\rm z - M_B$ and $\rm z - P_{1.4GHz}$ planes only sources with $M_B \lesssim -24.2$ and $\rm log_{10}P_{1.4GHz} \gtrsim 24.5$ ($\rm W\ Hz^{-1}\ sr^{-1}$) can be considered in the analysis (see Figure 4.2). In the redshift range $0.5 \lesssim z \lesssim 0.8$ the number of sources satisfying these criteria is extremely small and therefore we considered only sources with $z \geq 0.8$ in the computation of the LFs. After the above corrections, the final sample used for determination of LFs comprises $\sim$ 200 sources. It is worth noting that in the following analysis photometric and spectroscopic incompleteness of the 2QZ survey in the considered redshift range – both as a function of redshift and apparent magnitude – has been taken into account following Croom et al. (2004).

Radio LF

Cosmology	Evol.	α	β	$\log_{10}P^*_{1.4}$	k_1	k_2	Φ_0	P_{KS}
I	L	-0.1 ± 0.1	1.5 ± 0.2	22.7 ± 0.4	4.5 ± 0.5	-1.5 ± 0.2	5.0×10^{-8}	0.2
I	D	-0.1 ± 0.1	1.6 ± 0.3	26.0 ± 0.2	2.9 ± 0.6	-0.9 ± 0.2	2.5×10^{-10}	0.6
II	L	-0.1 ± 0.1	1.5 ± 0.2	22.9 ± 0.5	4.3 ± 0.6	-1.5 ± 0.2	4.2×10^{-8}	0.2
II	D	-0.1 ± 0.1	1.7 ± 0.4	26.0 ± 0.2	2.9 ± 0.6	-0.9 ± 0.2	2.0×10^{-10}	0.5

Optical LF

Cosmology	Evol.	α	β	M^*	k_1	k_2	Φ_0	P_{KS}
I	L	0.2 ± 0.6	2.4 ± 0.5	20.4 ± 1.0	2.3 ± 0.5	-0.8 ± 0.2	6.3×10^{-8}	0.6
I	D	0.7 ± 0.2	2.9 ± 0.7	25.6 ± 0.4	1.3 ± 0.5	-0.5 ± 0.1	5.3×10^{-9}	0.5
II	L	0.6 ± 0.3	2.8 ± 0.3	21.1 ± 1.0	2.0 ± 0.5	-0.6 ± 0.2	4.4×10^{-8}	0.4
II	D	0.8 ± 0.2	2.8 ± 0.7	25.6 ± 0.5	1.4 ± 0.5	-0.5 ± 0.2	3.1×10^{-9}	0.5

Table 4.1: Best fit parameters for the radio and optical LF of the FIRST-2dF sample. The characters L and D in the second column refer to a model of luminosity (Eq. 4.3) or density (Eq. 4.4) evolution, respectively.

The radio luminosities at 1.4 GHz have been calculated by using - whenever available - the measured α_R (see Table A.2) or adopting a mean value of $\alpha_R = 0.7$ (see Section 4.2.2).

As in previous Chapters, in order to easily compare our results with those found in literature we converted magnitudes from the b_J to the B band, applying a mean correction $B = 0.07 + b_J$ (see Section 2.3.1).

4.3.1 Binned $1/V_{max}$ method

The simplest approach to estimate LFs and their redshift evolution is provided by the 'classical' $1/V_{max}$ method (Schmidt 1968). For each source we evaluated the maximum redshift at which it could have been included in the sample, $z_{max} = \min(z^R_{max}, z^O_{max})$, where z^R_{max} and z^O_{max} are the redshifts at which the sources would not be selected due to the radio or the optical limiting flux densities, respectively.

Radio (RLF) and optical (OLF) luminosity functions have been computed in four equally spaced redshift bins ($\Delta z = 0.35$) and showed in the four panels of Figure 4.3 and 4.5, respectively.

4.3.2 Parametric method

To obtain an independent and more quantitative description of the LFs and to avoid loss of information due to the binning, we also carried out a maximum likelihood analysis. This is a parametric technique which relies on maximizing the probability of observing exactly one quasar in a $\Delta z \Delta L$ element at each redshift and luminosity for all the quasars in the dataset and of observing zero objects in all the other differential elements in the accessible regions of the redshift-luminosity plane (Marshall et al. 1983). This method requires an analytic functional form for the LF (Φ) and its evolution.

We chose to model both the radio and optical LFs as double power laws in luminosity (or magnitude) as:

$$\Phi(P_{1.4}, z) = \frac{\Phi_0}{(P_{1.4}/P^*_{1.4})^{\alpha} + (P_{1.4}/P^*_{1.4})^{\beta}} \tag{4.1}$$

and

$$\Phi(M_B, z) = \frac{\Phi_0}{10^{0.4(\alpha+1)(M_B - M^*_B)} + 10^{0.4(\beta+1)(M_B - M^*_B)}}, \tag{4.2}$$

The time-evolution of the LFs has been modeled with a 2nd-order polynomial function both in the case of pure luminosity evolution:

$$L^*(z) = L^*(z=0) \ \times \ 10^{k_1 z + k_2 z^2}, \tag{4.3}$$

where L^* is the radio or optical break luminosity, and pure density evolution:

$$\Phi_0(z) = \Phi_0(z=0) \ \times \ 10^{k_1 z + k_2 z^2} \tag{4.4}$$

The best fit parameters have been obtained by minimizing the likelihood function :

$$\mathcal{L} = -2 \sum_{i=1}^{N} \ln[\Phi(L_i, z_i)] + 2 \iint \Phi(L, z) \Omega \frac{dV}{dz} dz d\log_{10} L, \tag{4.5}$$

where $(dV/dz)dz$ is the differential co-moving volume element, Ω is the sky area covered by the sample and $\Phi(L, z)$ is the model distribution being tested. In the first term of this equation, the sum is over all the N sources in the sample.

The best fit parameters have been obtained by minimizing the likelihood function, through the MINUIT package from the CERN Libraries. Their values are given in Table 4.1

for both the radio and optical LFs. Errors on each parameter, corresponding to 68 per cent confidence level, have been obtained by using the MINOS task in MINUIT. This algorithm consists of varying one parameter per time, and then minimizing the likelihood function with respect to all the other parameters, in order to find a variation in the function corresponding to one standard deviation error. Figures 4.3 and 4.5 show the best-fit solutions obtained from the likelihood analysis (solid curves), compared with the LFs obtained with the binned method (Section 4.3.1). The analytical functions have been computed at the mean redshift of each bin. The agreement between LFs obtained through these two independent methods is remarkably good.

To have a quantitative assessment of the goodness of the best-fit parameters we used a 2D Kolmogorov-Smirnov (KS). This multidimensional version of the KS test (Press et al. 1992) compares the observed redshift-luminosity plane with the one obtained integrating the LF. Note that the KS test can only be used to reject models when the resulting probability $P_{\rm KS}$ is less than 0.1 or 0.05. In our case the probability $P_{\rm KS}$ values are ≥ 0.2 (see Table 4.1), implying that the data and model are not significantly different.

Models obtained by assuming a pure density evolution have a slightly better KS probability as it is shown in Table 4.1. However, as said the KS test is only useful to reject a model. Moreover, in the redshift range ($0.8 \lesssim z \lesssim 2.2$) the radio LFs obtained with the two evolution models are very similar, since we are sampling only the faint end of the LF. Figures 4.3 and 4.5 then show our results for the luminosity evolution model.

In order to provide a more direct visualization of the redshift evolution of the LFs, in each panel of Figures 4.3 and 4.5 we also reported – as a dotted line – the LF at the maximum of its redshift evolution which is obtained for both the radio and optical bands at $z \sim 1.7 \pm 0.2$. We note that this preliminary analysis suggest the presence of a decline in the observed number density of objects at $z \sim 2$. Even though this is not statistically significant and more data are needed to verify the trend, this appears to hold in both bands. We will present stronger evidence for the above finding in Section 4.4.

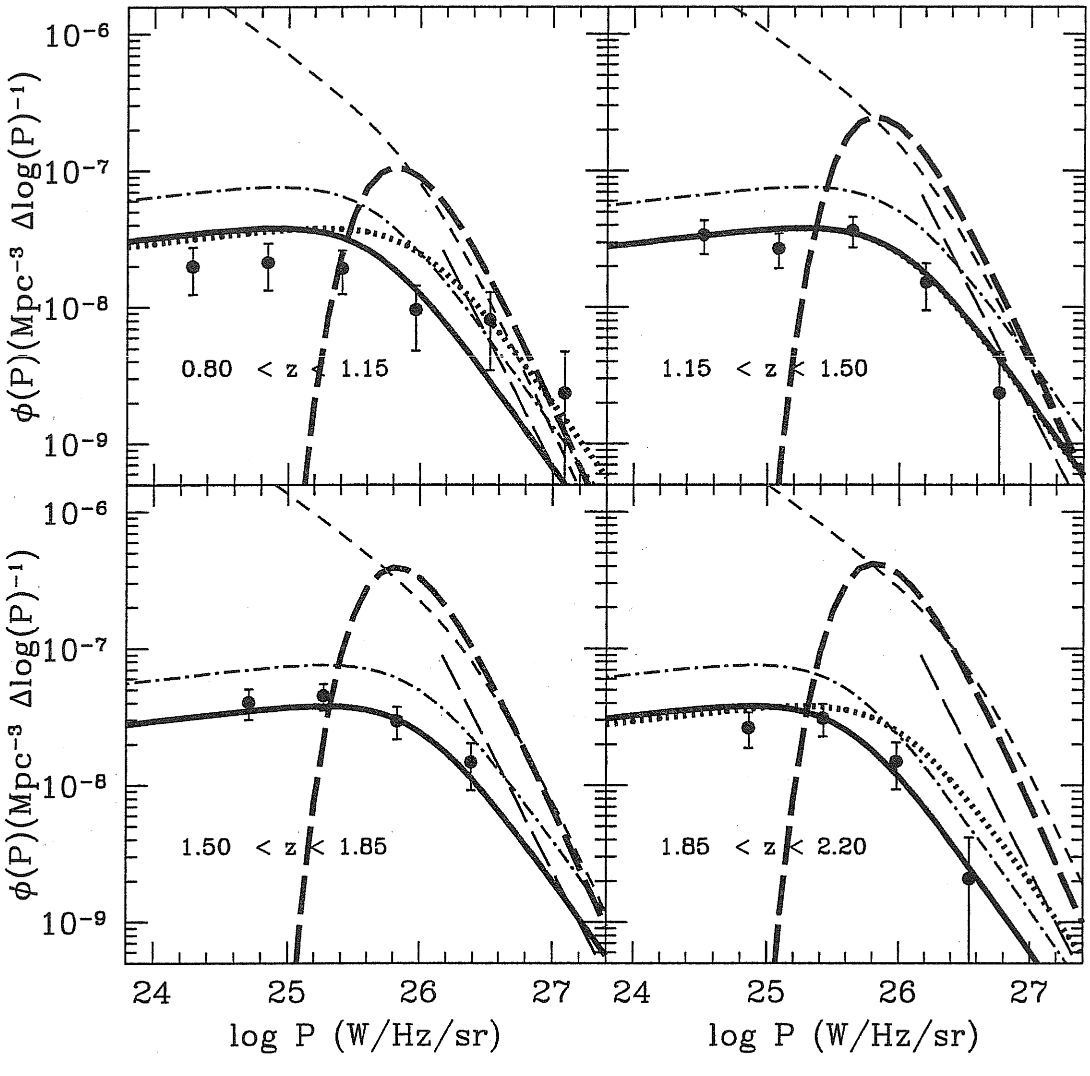

Figure 4.3: Radio luminosity functions for sources in the FIRST-2dF sample. The filled circles represent the LF obtained with the $1/V_{max}$ method and the solid lines derived from the likelihood analysis, by assuming a luminosity evolution model in cosmology I. The dotted lines is the RLF at the redshift of its maximum, while the dot-dashed lines are the RLFs corrected in normalization by a factor of 2 (see text). For comparison, we also plotted the LFs from Dunlop & Peacock (1990) (dashed), Willott et al. (1998) for steep spectrum radio loud quasars (thin long-dashed lines) and Willott et al. (2001) for the high luminosity radio population (thick long-dashed lines).

4.3.3 Assessment of incompleteness

It is worth noting that LFs, presented in previous Section, have been computed by applying various cuts to the dataset, both in redshift and luminosities. In fact, the analysis has been confined to a particular redshift range ($0.8 \leq z \leq 2.2$). Moreover, it has been used limits in both radio and optical luminosities, in order to avoid incompleteness effects and obtain an unbiased coverage of the redshift-luminosity planes. In this section we try to estimate the effects of these limits on the derived LFs, with particular attention devoted to the $M_B \lesssim -24.2$ and $\log_{10}\mathrm{P}_{1.4\mathrm{GHz}} \gtrsim 24.5$ ($\mathrm{W\,Hz^{-1}\,sr^{-1}}$) cuts.

In order to provide an estimate of the incompleteness affecting the radio LF, we considered the redshift interval $0.5 \lesssim z \lesssim 1.2$, in which the coverage of the $\mathrm{z} - \mathrm{M_B}$ plane is complete down to $M_B \sim -23$ (see Figure 4.2). In this redshift range, we computed the RLF both using sources with $M_B \leq -24.2$ and $M_B \leq -23$. It turns out that the shape of the RLF does not change by applying these two limits, while the normalization obtained in the case of $M_B \leq -24.2$ is about 2 times lower than that found in the $M_B \leq -23$ case. We stress that due to the small statistics in this redshift range such result should only be taken as a rough estimate of the true incompleteness. Therefore, we could assume that the $M_B \leq -24.2$ cut only affects the normalization of the RLF, independently of redshift. Therefore, under these "strong" assumptions, we can correct the RLF by applying a factor 2 in normalization, in order to have a rough estimate of the "complete" RLF of quasars down to $M_B \leq -23$.

We also tested for the effects of the $\log_{10}\mathrm{P}_{1.4\mathrm{GHz}} \geq 24.5$ ($\mathrm{W\,Hz^{-1}\,sr^{-1}}$) cut on the OLF. In the same redshift range ($0.5 \lesssim z \lesssim 1.2$) we can achieve completeness down to $\log_{10}\mathrm{P}_{1.4\mathrm{GHz}} \geq 24$ (see bottom panel of Figure 4.2). An analysis analogous to that applied for the RLF reveals that the cut at $\log_{10}\mathrm{P}_{1.4\mathrm{GHz}} \geq 24.5$ ($\mathrm{W\,Hz^{-1}\,sr^{-1}}$) does not affect the shape of OLF, as in the case of the RLF, but only its normalization by a factor ~ 1.5. Both radio and optical LFs corrected for this incompleteness assumed to hold at all redshifts (i.e. for LFs with a shape independent of z) are shown as dot-dashed lines in Figures 4.3 and 4.5.

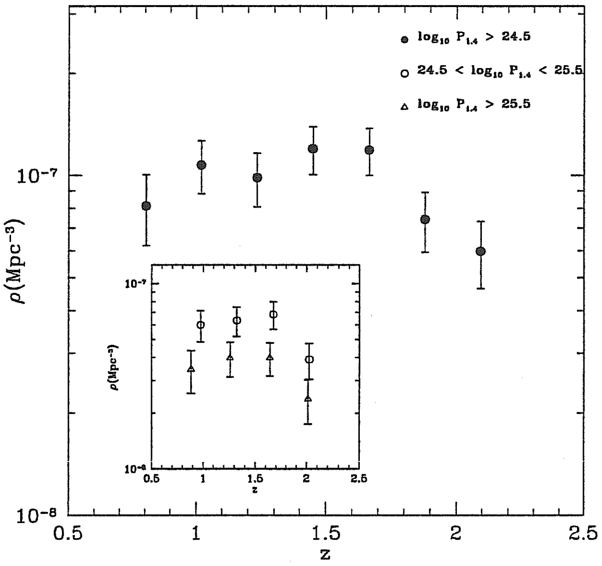

Figure 4.4: Space density as a function of redshift for sources in the FIRST-2dF sample for cosmology I. The small panel shows the same space density for two different bins in radio power.

4.4 Comparison with previous results

4.4.1 Radio Luminosity Function

Our results on the RLF can be significantly compared at its bright end with those obtained for bright radio selected quasars by Willott et al. (1998). A sample of steep spectrum quasars with $M_B < -23$ was selected by these authors from the 7C (McGilchrist et al. 1990) and 3CRR (Laing et al. 1983) catalogues. All their sources are found to be radio loud, due to the bright limits of these low frequency surveys, $\mathrm{S}_{151\mathrm{MHz}} \geq 0.51$ Jy and $\mathrm{S}_{178\mathrm{MHz}} \geq 10.9$ Jy, respectively.

Before moving on, a caveat is necessary. Our dataset cannot discriminate between steep and flat objects. As discussed in Section 4.2.2, most of the sources in the FIRST-2dF sample are probably steep spectrum, as suggested by the lack of detection in the PMN. Moreover, at low radio powers ($\log_{10}\mathrm{P}_{1.4\mathrm{GHz}} \lesssim 26$ W Hz^{-1} sr^{-1}), the number of flat spectrum sources is much smaller than the steep spectrum ones even in samples selected at high frequencies (Dunlop & Peacock 1990; Maraschi & Rovetti 1994). Therefore, this allows us to directly compare our data with the steep spectrum dataset of Willott et al. (1998).

In order to perform this comparison, we have converted source luminosities from the Willott et al. (1998) dataset to 1.4 GHz by assuming a radio spectral index $\alpha_{\rm R} = 0.7$. The RLF for their best fit (model C) are shown in Figure 4.3 as thin long dashed lines.

These appear to be in reasonably good agreement with our RLF (corrected for renormalization, see Section 3.3). In fact, the slopes of the bright ends are similar, even though the statistics of our data is very poor in this luminosity range. Our best fit value for the slope is 1.7 ± 0.3, fully consistent with 1.9 ± 0.1 quoted by Willott et al. (1998). The second important aspect is related to the flattening of the RLF at the faint end. Due to the paucity of the data, Willott et al. estimated the value of the break luminosity by fixing a slope $\alpha = 0$ for the faint end and fitting the radio number counts at 0.1 Jy. This procedure led to a value of the break luminosity $\log_{10}{\rm P}^*_{151{\rm MHz}} \sim 26.8$ (W Hz^{-1} sr^{-1}), i.e. ~ 26.0 when translated at 1.4 GHz. With our sample – which is more than 100 times fainter than the 7C – we can directly determine for the first time this flattening and our analysis confirms that the faint end is well described by $\alpha \sim 0$. Furthermore, we infer a break luminosity at $\log_{10}{\rm P}_{1.4{\rm GHz}} \sim 26.$ W Hz^{-1} sr^{-1}in agreement with that of Willott et al. (1998), both by considering a luminosity evolution and a density evolution model.

The evolution of the RLF found in our sample is also consistent with that derived for brighter sources, showing a maximum at $z \sim 1.7$. However, the FIRST-2dF sample shows indications for a negative evolution beyond $z \sim 1.8$ (see Section 4.3.2), while the brighter Willott et al. sample is consistent with no evolution up to the highest redshifts probed by their surveys ($z \sim 3$). However, due to the small number of sources (< 10) in the range $2 \lesssim z \lesssim 3$, their claim is not very robust, at least for $z \gtrsim 2$. In order to assess the statistical significance of our finding of a negative evolution beyond $z \sim 1.8$, we considered the behaviour of the quasar number density $\rho(z)$, at different redshifts. This is obtained by integrating the LFs over the luminosity range detectable up to the highest redshift in our data. It is worth noting that, even though we do not have information on the bright end of the RLF, our sample extends up to the break of the LF, accounting for the bulk of the sources. The number density $\rho(z)$ is plotted in Figure 4.4, where the error bars indicate

Poissonian uncertainties. We find that the space density of FIRST-2dF quasars shows a significant ($\sim 3\sigma$) tendency for a decrement at $z \gtrsim 1.8$. Such a decrement is found to be approximately a factor 2 at $z = 2.2$. We want to stress that these results are found to hold in both cosmologies.

In the small panel of Figure 4.4 we also show the space density computed for two bins of radio power. The decline observed for the whole sample is still evident for low-luminosity objects as well as for brighter ones. For these latter sources the decline seems to be less pronounced, but this effect is somewhat masked by larger error-bars due to small statistics.

We note that our choice of a single spectral index ($\alpha_{\rm R} = 0.7$) for all the sources undetected by PMN could introduce some uncertainties in the determination of $\rho(z)$. In fact, radio spectra steepen at higher frequencies and, as shown by Jarvis & Rawlings (2000), this is crucial in determining the space density of radio objects at high redshift.
In order to quantify this effect we have then considered an "extreme case" and associated all the sources with $z > 1.7$ with a steep spectral index ($\alpha_{\rm R} = 1.5$). This results in larger radio powers for these sources, which in turn cause a rise in the bright end of the LF, to the detriment of fainter luminosities.
The crucial point in this case is the assessment of the completeness of the sample. In fact, due to the steeper spectral index at high z, the observed fluxes drop more rapidly than expected with redshift. However, even by assuming such a steep spectral index ($\alpha_{\rm R} = 1.5$) for $z > 1.7$, the 2 mJy limit of our sample ensures completeness down to $\log_{10}{\rm P}_{\rm 1.4GHz} \sim 25$ W Hz^{-1} sr^{-1}for $z \leq 2.2$. This, together with the fact that the trend for the space density of fainter and brighter sources is found to be the same (cfr Figure 4.4), makes us confident that our results, and particularly those on the space density of radio-loud quasars, are not severely affected by the uncertainty associated to an unknown spectral index.

Another source of uncertainty could arise from the double selection, in both radio and optical band, since radio and optical luminosities are related, even though with a large scatter (Cirasuolo et al. 2003b). Therefore, low luminosity radio sources could drop through the optical flux limit more quickly than the brighter radio ones. This selection effect would be effective at all redshifts, being more evident at high z due to the redshift dependence of the limiting luminosity (see Figure 4.2), producing a fake decline in the space density. However, the large scatter between radio and optical luminosities – at least three orders of magnitude in radio luminosity at a fixed optical one (Cirasuolo et al. 2003a) – completely overtop this selection effect. This is confirmed by the evidence of a same decline in the space density at high redshift when computed for different radio powers (see Figure 4.4).

The last point worth stressing is that we find no evidence for a strong decrement in the space density at low redshifts. In fact, $\rho(z)$ is found to decrease by only a factor ~ 1.5 between $z \sim 1$ and $z \sim 0.5$. This lack of a significant evolution at low redshifts has also been recently claimed by Clewley & Jarvis (2004) for fainter sources ($\mathrm{P}_{325\mathrm{MHz}} < 10^{25}$ $\mathrm{W\,Hz^{-1}\,sr^{-1}}$) at $z < 0.5$, even though the evolution of the very low luminosity population (i.e. FRI) still remains unconstrained (Magliocchetti, Celotti & Danese 2002).

4.4.2 Optical Luminosity Function

Clearly the best reference for the OLF of the radio quasar sample is constituted by the OLF of the 'parent' (2dF QSO Redshift Survey) population (Croom et al. 2004).

In Figure 4.5 we report the best fit solutions for the OLF found by Croom et al. (2004) (dashed lines, corresponding to the polynomial evolution model in the case of cosmology I). As in the case of the RLF, we applied a correction of a factor 1.5 in the normalization of our OLF to account for incompleteness effects (see Section 4.3.3). This provides an estimate of the OLF (dot-dashed lines) representative of the whole population of radio-active quasars with $\log_{10}\mathrm{P}_{1.4\mathrm{GHz}} \geq 24$ ($\mathrm{W\,Hz^{-1}\,sr^{-1}}$).

As expected, the OLF of radio detected quasars is flatter than the one derived for the population as a whole. This is already visible at the brighter end where the slope of the FIRST-2dF OLF is $\beta \sim 2.4-2.8$ (depending on the adopted model), while that obtained by Croom et al. (2004) is $\beta = 3.2$. This trend becomes increasingly more significant towards fainter magnitudes. Indeed, this is consistent with the observed dependence of the fraction of radio detected quasars as a function of optical luminosity (Padovani 1993; La Franca et al. 1994; Hooper et al. 1995; Cirasuolo et al. 2003a). However, Cirasuolo et al. (2003b) showed that this can simply be the result of selection effects due to the radio and optical limits of the various samples under exam, under the assumption that the optical and radio

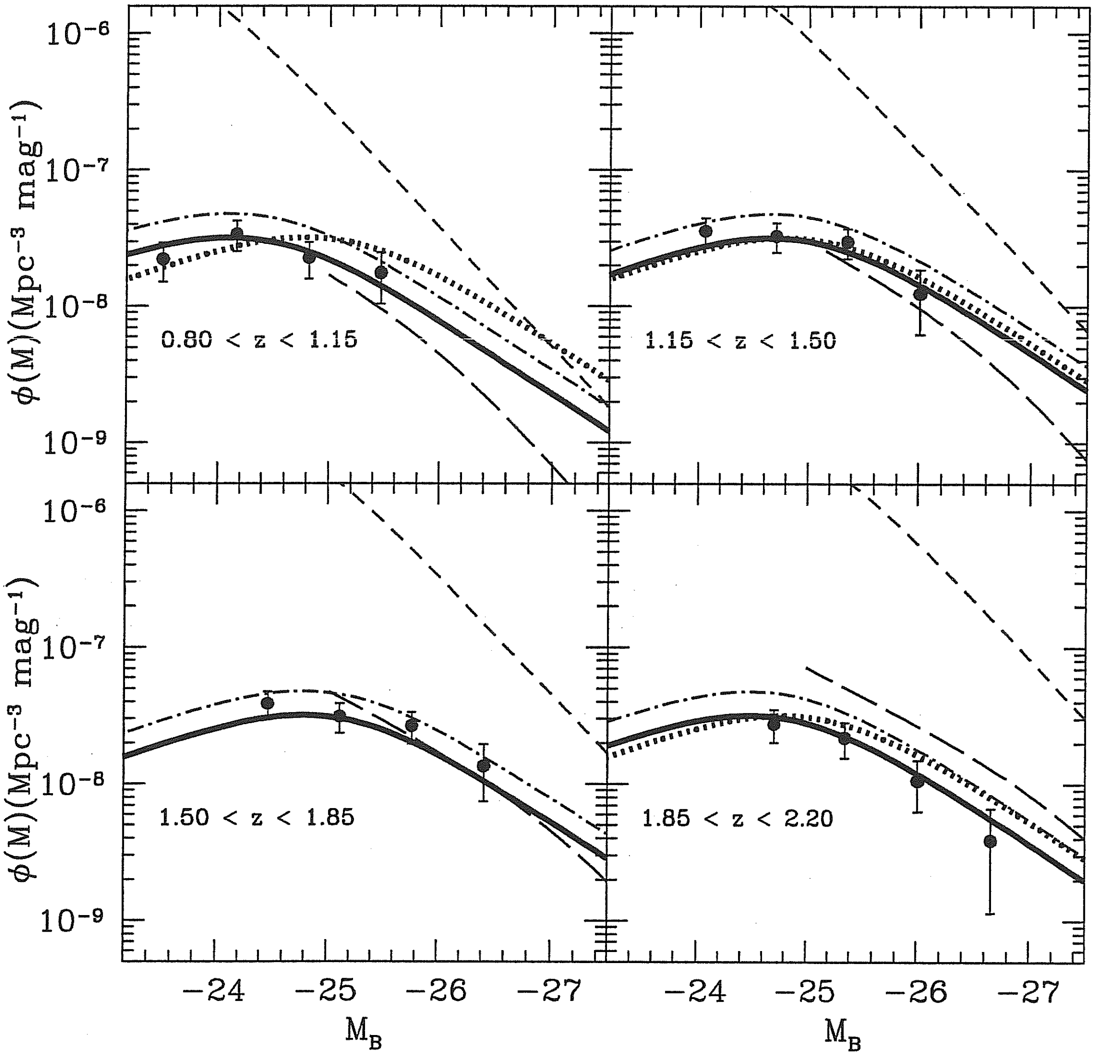

Figure 4.5: Optical luminosity function for sources in the FIRST-2dF sample. The filled circles represent the LF obtained with the $1/V_{max}$ method and the solid lines derived from the likelihood analysis, by assuming a luminosity evolution model in cosmology I. The dotted lines is the OLF at the redshift of its maximum, while the dot-dashed lines are the OLFs corrected in normalization by a factor of 1.5 (see text). For comparison, we also plotted the LFs from La Franca et al. (1994) (long-dashed) and for the quasar population as a whole (Croom et al. 2004, dashed lines).

luminosities are linearly (even though) broadly correlated. In this case the intrinsic shape of the distribution of the radio-to-optical ratio $R^*_{1.4GHz}$ for the quasar population as a whole is found to show a broad peak at $R^*_{1.4GHz} \sim 0.3$ containing more than 90 per cent of the sources, followed by a steep transition region at $1 \lesssim R^*_{1.4GHz} \lesssim 10$ (see Fig. 4 in Cirasuolo et al. 2003b). This implies that, at a given radio flux limit, surveys with brighter optical limiting magnitudes preferentially select smaller values of $R^*_{1.4GHz}$ – i.e. closer to the peak of the distribution – which results in a higher percentage of radio detections.

In Figure 4.5 we also compare our results with previous determinations of the OLF for bright ($M_B \lesssim -25$) radio-loud quasars (La Franca et al. 1994; their best-fit function (model B) is indicated with long-dashed lines). An overall good agreement between the two OLFs is found in the magnitude range in which the two samples overlap.

The OLF obtained from our sample peaks at $z \sim 1.7$ and – as in the case of the radio LF – possibly hints to a decline at higher redshifts. On the contrary, La Franca et al. (1994) find a maximum redshift for luminosity evolution $\mathrm{z_{max}} \sim 1.9$, beyond which no further evolution is detected. The same substantial lack of evolution in the range $1.5 \lesssim z \lesssim 2$ has also been claimed by Goldschmidt et al. (1999). However, we argue that the limited dimensions of their $z \sim 2$ samples do not allow for any strong statistical conclusion.

4.4.3 The whole radio source population

Let us finally consider the relation between the radio quasar and the entire radio source population. The dashed lines in Figure 4.3 represent the RLF for steep plus flat spectrum radio sources obtained by Dunlop & Peacock (1990) (calculated at 1.4 GHz by assuming a radio spectral index $\alpha_{\mathrm{R}} = 0.7$ for steep spectrum sources). It is clear that the fraction of radio quasars decreases toward lower powers, implying that for $\log_{10}\mathrm{P}_{1.4\mathrm{GHz}} \lesssim 26$ ($\mathrm{W\,Hz^{-1}\,sr^{-1}}$) the fraction of radio galaxies is dominant with respect to radio quasars, while at higher luminosities the two populations are of comparable importance. The shaded area in Figure 4.6 shows the ratio f_{QSO} between the RLF of radio quasars – drawn from the FIRST-2dF sample and corrected in normalization – and the RLF of Dunlop & Peacock (1990) as a function of radio luminosity. The increasingly larger scatter for $\log_{10}\mathrm{P}_{1.4\mathrm{GHz}} \gtrsim 25.5$ ($\mathrm{W\,Hz^{-1}\,sr^{-1}}$) is due to the different evolution in redshift of the two

RLFs. As already discussed, the space density of radio active quasars is found to decline at high redshift, while the radio population as a whole still shows a positive evolution, therefore increasing the scatter in $f_{\rm QSO}$. A similar trend in the fraction of quasars as a function of luminosity has been found by Willott et al. (2000) by analyzing radio selected samples. They found that this fraction is ~ 40 per cent at bright (narrow [OII]) emission line luminosities ($L_{[OII]}$) – assumed to be good tracer of the ionizing continuum – dropping to a few per cent for fainter luminosities. They suggested that this finding can be accounted for by either a gradual decrease of the opening angle of the obscuring 'torus' with decreasing ionizing luminosity or with the emergence of a distinct population of low luminosity radio sources, like M87.

Following the approach suggested by Willott et al. (2000) we try to interpret the decrease of $f_{\rm QSO}$ within the 'receding torus' scenario. In this model, initially proposed by Lawrence (1991; see also Simpson 1998), the inner radius of the torus depends on the AGN radiation field which sublimates the dust grains. If the scale-height of the torus is independent on the ionizing luminosity $L_{\rm ion}$, its inner radius scales as $L_{\rm ion}^{0.5}$ resulting in larger half-opening angles θ at higher luminosities. The fraction of quasars predicted is then:

$$\mathrm{f_{QSO}} = 1 - \left(1 + \left(\frac{L_{\rm ion}}{L_0}\right) \tan^2\theta_0\right)^{-0.5}, \qquad (4.6)$$

where L_0 and θ_0 are a normalization luminosity and the corresponding torus half-opening angle, both fixed by the measured quasar fraction at that luminosity. As we cannot rely on the $L_{[OII]}$ as Willott and collaborators, as a working hypothesis we use the radio luminosity as a tracer of the central ionizing radiation field. This is based on the relation between radio power at 151 MHz and $L_{[OII]}$ suggested by Willott et al. (1999), $L_{[OII]} \propto L_{151}^{0.79}$, although with a large scatter. Because of this uncertainty, we modified Eq. 4.6 assuming that the ionizing luminosity scales as P^{δ}, where P is the radio power at 1.4 GHz and δ is a free parameter, i.e.:

$$\mathrm{f_{QSO}} = 1 - \left(1 + \left(\frac{P}{P_0}\right)^{\delta} \tan^2\theta_0\right)^{-0.5}. \qquad (4.7)$$

Different values for the parameter δ have been tested in order to reproduce the measured fraction of radio active quasars. As shown in Figure 4.6, a nearly linear dependence of the central ionizing luminosity on the radio power ($\delta \sim 1$) is able to reproduce the observed

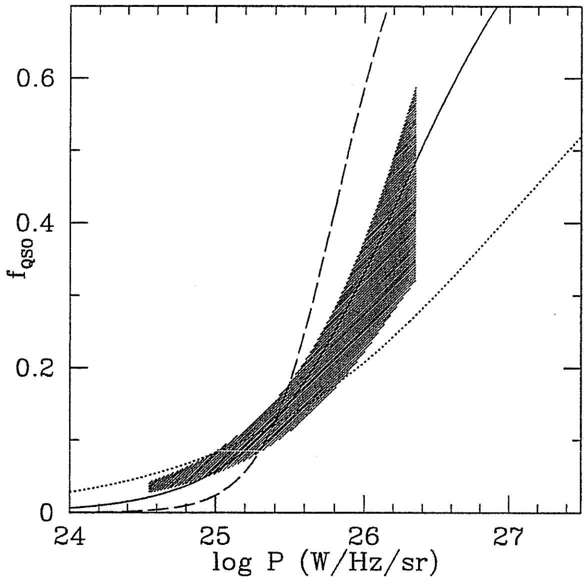

Figure 4.6: Fraction f_{QSO} of radio quasars from the FIRST-2dF sample with respect to the whole radio population (taken from Dunlop & Peacock 1990) as a function of radio power (shaded area). The solid line is the predicted fraction on the basis of equation 4.7 assuming $\delta = 1$, while the dotted and dashed lines respectively correspond to $\delta = 0.5$ and $\delta = 2$. The predicted fractions have been normalized at $\log_{10} P_{1.4GHz} = 25.5$ W Hz^{-1} sr^{-1}.

fraction, while $\delta \simeq 0.5$ is only marginally consistent with the observed trend. The extreme value ($\delta = 2$) is totally inconsistent with the observed behaviour. This finding is a posteriori broadly consistent with the relation $L_{[OII]}$ vs L_{151} found by Willott et al. (1999) and with the evidence found by Cirasuolo et al. (2003b) for a nearly linear dependence of the radio luminosity on the optical one.

The comparison between the radio quasar and the whole radio source population within the framework of the unification scenario – postulating that radio-loud quasars represent the beamed counterparts of powerful (FRII) radio sources – reveals a further aspect worth mentioning. Willott et al. (2001) proposed a dual population model for the RLF by separating the contribution from the high and low luminosity sources assumed to have a differential density evolutions. The latter population can be associated with weak emission lines radio galaxies – both FRI and FRII – while the high luminosity population can be representative of radio galaxies and quasars with strong emission lines and FRII radio properties. A comparison of our RLF with that of the high power population identified by

Willott et al. (2001) (transported at 1.4 GHz by assuming $\alpha_{\rm R} = 0.7$; thick long-dashed lines in Figure 4.3) shows that at $\log_{10}{\rm P}_{1.4{\rm GHz}} < 25$ (W Hz^{-1} sr^{-1}) the observed quasar number density largely exceeds that of the whole population. [1] as derived by Willott et al.

It is worth reminding here that all the sources in the FIRST-2dF sample are classified as quasars, based on both their broad emission lines and bright luminosity ($M_B \leq -23$). Furthermore, they are radio loud according both to their radio luminosity ($\log_{10}{\rm P}_{1.4{\rm GHz}} \geq 24$ W Hz^{-1} sr^{-1}; Miller et al. 1990) and radio-to-optical ratio ($R^*_{1.4GHz} \geq 30$; Kellermann et al. 1989). However, for the first time, the FIRST-2dF sample is able to explore the low optical and radio luminosity ranges. In particular, the radio powers sampled with this work approach the transition region between FRII and FRI sources, posing the problem of the nature of these objects.

A few possibilities are open. They could hint at a population of quasars with intermediate FRII-FRI radio properties, either intrinsic or due to an evolution between these two radio phases (such as those discussed by Blundell & Rawlings 2001). Alternatively, these objects might be bordering the intermediate radio quasar population (i.e. between loud and quiet radio quasars with no evidence for relativistic jets). Finally, they might simply represent a lower luminosity version of powerful radio quasars, which thus do not obviously fit into the 'classical' scheme for radio sources. This might correspond to the fading phase of luminous quasars. Interesting clues on this issue would come from the study of their radio morphology.

4.5 Discussion

The novelty of our work is that, by exploiting the faint observational limits of both radio and optical surveys such as the FIRST and the 2dF Quasar Redshift Survey, it was possible for the first time to explore the faint end of the LFs of radio (loud) quasars at both wavelengths. Furthermore, the larger number of radio-detected quasars collected by using these datasets allowed for a suitable determination of these LFs up to $z = 2.2$.

The most intriguing result we found is the indication ($\sim 3\sigma$) – both in radio and

---

[1] Formally, the low luminosity end of the distribution of the Willott et al. (2001) powerful population actually cuts even above the definition of FRII-like sources ($\log_{10}{\rm P}_{1.4{\rm GHz}} \sim 24.5$ W Hz^{-1} sr^{-1}at 1.4 GHz).

optical band – of a negative evolution for these faint sources at $z > 1.8$. This corresponds to a decrement in the space density of faint quasars of about a factor 2 at z=2.2. For brighter – either radio or optically selected – samples, the evolution of radio loud quasars shows a peak at $z \sim 1.7 - 2.0$, but no evidence for a decline at higher redshifts (Willott et al. 1998; La Franca et al. 1994; Goldschmidt et al. 1999). This result is thus consistent with the presence of a differential evolution for the population of radio-active quasars (Vigotti et al. 2003), where the weakest radio sources show a more pronounced decline in space density than the more powerful ones, suggesting the evolution to be a function of the intrinsic power (as in the luminosity/density evolution model of Dunlop & Peacock 1990).

The second interesting finding is the flattening of the faint end of the LFs of radio active quasars in both the radio and optical bands. The behaviour of the OLF at faint magnitudes we find is consistent with previous estimates performed at brighter magnitudes (La Franca et al. 1994; Goldschmidt et al. 1999), and the comparison with the OLF of the quasar population as a whole supports a dependence of the fraction of radio detected quasars on their optical luminosity. This flattening can simply result from a linear although broad intrinsic correlation between the radio and optical luminosities when combined with radio and optical limits of the various surveys (Cirasuolo et al. 2003b).

Finally, we find that a progressive decrement in the fraction of quasars in the whole radio source population can be consistently accounted for within the 'receding torus' scenario by assuming a quasi-linear dependence between optical and radio luminosities. At this stage, the nature of the lower radio luminosity sources in our sample appears unclear substantially due to the lack of information on the origin of the radio emission, which could be unveiled by higher resolution radio imaging.

Chapter 5

Radio properties of the highest redshift complete quasar sample

5.1 Introduction

A challenging extension of the work presented in previous Chapters will be to study the radio properties of quasars at even higher redshift. To this purpose, the Sloan Digital Sky Survey represents an unprecedented source of information. Radio data of a complete sample of sources, selected from this survey, will allow us to test whether the radio properties, observed in quasars at lower redshift ($z \lesssim 2$), are constant or change with time. Therefore, it will be possible to study whether physical conditions present in the early stages of quasar activity, can favor or prevent the formation of relativistic jets.

For this goals we proposed deep radio observations at 1.4 GHz with the Very Large Array (VLA) of a complete sub-sample of high-redshift quasars drawn from SDSS (Fan et al. 2001a). In this Chapter, we present very preliminary results, as the data reduction and analysis is still an ongoing work. For sake of comparison with previous works we will adopt the E.d.S. Cosmology (see Chapter 1).

5.2 SDSS sample

The optical quasar sample we deal with is drawn from the SDSS survey and has been used by Fan et al. (2001b) to compute the optical luminosity function at high redshift, as described in Chapter 1. The complete sample (Fan et al. 2001a) consists of 39 bright ($i^* \lesssim 20$) high-redshift ($3.5 \leq z \leq 5$) color-selected quasars in the Fall Equatorial Stripe at high Galactic latitude ($22^h20^m \lesssim RA(2000) \lesssim 4^h30^m$), covering an area of 182 sq. deg. Photometric observations have been obtained with the 2.5m SDSS telescope (York et al. 2000), located at Apache Point Observatory in southeastern New Mexico, in 5 broad filters (u^*, g^*, r^*, i^*, z^*) covering the entire optical band from the atmospheric cutoff in the blue to the silicon sensitivity cutoff in the red (Fukugita et al. 1996). The 5-σ limiting magnitudes are roughly 22.3, 22.6, 22.7, 22.4 and 20.5 in u^*, g^*, r^*, i^*, and z^*, respectively, for a single observation (Fan et al. 1999; Fan et al. 2001a).

High-redshift quasar candidates were selected using color cuts adopting the criteria: 1. *gri* candidates, selected principally from the $g^* - r^*, r^* - i^*$ diagram:

$$\begin{aligned}
&(a)\ i^* < 20.05\\
&(b)\ u^* - g^* > 2.00 \text{ or } u^* > 21.00\\
&(c)\ g^* - r^* > 1.00\\
&(d)\ r^* - i^* < 0.42(g^* - r^*) - 0.31 \text{ or } g^* - r^* > 2.30\\
&(e)\ i^* - z^* < 0.25
\end{aligned} \tag{5.1}$$

2. *riz* candidates, selected principally from the $r^* - i^*, i^* - z^*$ diagram:

$$\begin{aligned}
&(a)\ i^* < 20.20\\
&(b)\ u^* > 22.00\\
&(c)\ g^* > 22.60\\
&(d)\ r^* - i^* > 1.00\\
&(e)\ i^* - z^* < 0.47(r^* - i^*) - 0.48
\end{aligned} \tag{5.2}$$

The intersections of these color cuts with the $g^* - r^*, r^* - i^*$ and $r^* - i^*, i^* - z^*$ diagrams are illustrated in Figure 5.1. Quasar candidates, that meet these criteria, were

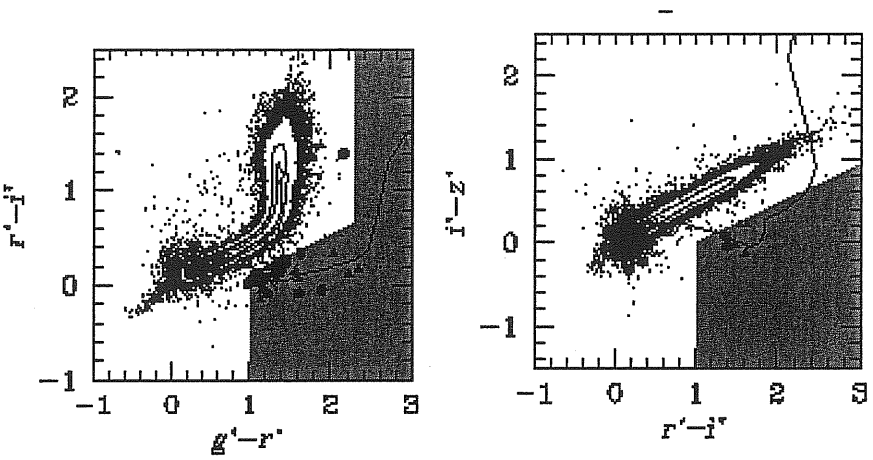

Figure 5.1: Color-color diagrams for all stellar objects with $i^* < 20.2$ from Fan et al. (2001a). The shaded areas on the $g^* - r^*$ vs. $r^* - i^*$ and the $r^* - i^*$ vs. $i^* - z^*$ diagrams represent the selection criteria used to select quasar candidates. The solid line is the median track of simulated quasar colors as a function of redshift (adapted from Fan 1999). Left and right panel also show the colors of 39 quasars at $z > 3.6$ in the complete sample, circles are quasars from Fan et al. (2001a) and triangles from Fan et al. (1999a) and Schneider et al. (2001).

observed using the Keck II telescope and the Hobby-Eberly Telescope (Fan et al. 1999; Fan et al. 2001a; Schneider et al. 2001), in order to obtain the spectra.

The quasar continuum is assumed to be a power law with a slope α_o: $f_\nu \propto \nu^{\alpha_o}$. The continuum magnitude, AB_{1450}, is defined as the AB magnitude at $\lambda = 1450$ Å in the rest frame corrected for Galactic extinction. AB magnitude can be converted to flux units as:

$$\mathrm{AB}_\nu = -2.5 \log f_\nu - 48.60, \tag{5.3}$$

where f_ν has units of erg s^{-1} cm^{-2} Hz^{-1}. For a power law continuum, AB_{1450} can be converted to the rest-frame Kron-Cousins B band magnitude:

$$\mathrm{B} = \mathrm{AB}_{1450} + 2.5\alpha_o \log(4400/1450) + 0.12. \tag{5.4}$$

The effective wavelength in the B band is 4400 Å, and the factor 0.12 is the zeropoint difference between the AB magnitude system and the Vega-based system in the B band (Schmidt et al. 1995).

5.3 VLA observations

Out of 39 sources, constituting the complete sample, 5 of them have a counterpart in the FIRST survey (described in Chapter 2), with radio fluxes, at 1.4 GHz, relatively high: $1.4 \lesssim S_{1.4\mathrm{GHz}}(\mathrm{mJy}) \lesssim 10$. Other 15 sources were observed by Carilli et al. (2001), under an extensive observational program of high redshift quasars at radio wavelengths. These sources were observed for $\sim$ 2 hours each, reaching a theoretical rms (σ_{rms}) of the order of $20 - 30$ μJy. Only 4 sources were detected at $> 3\sigma_{\mathrm{rms}}$ and other 3 sources at $2 \leq \sigma_{\mathrm{rms}} \leq 3$. Trusting in the careful analysis performed by these authors and considering the exact coincidence of the radio position with the quasar optical one, we will take as a true detections even these latter three sources at $> 2\sigma_{\mathrm{rms}}$ for this preliminary analysis.

In order to have radio observations of the whole optically selected sample, we proposed deep 1.4 GHz VLA observations of the remaining 19 sources. These radio observations were made in the BnA (mixed 30 km and 10 km) configuration on October 2003 and January 2004, using a total bandwidth of 100 MHz, with two orthogonal polarizations. Each source was observed for a total of about 2 hours, with short scans made over a large range in hour angle to improve Fourier spacing coverage. Standard phase and amplitude calibration were applied, as well as self-calibration using background sources in the telescope beam. The absolute flux density scale was set using observations of 3C 48. The final images were generated using the wide field imaging and deconvolution capabilities of AIPS. The Gaussian restoring CLEAN beams were of the order of $4''$ FWHM and the theoretical rms noise value is ~ 20 μJy beam^{-1}.

Four sources, shown in Figure 5.2, have been detected at $> 3\sigma_{\mathrm{rms}}$, with a measured noise values close to the theoretical one. One of these sources, J0244-0108, is relatively bright ($S_{1.4\mathrm{GHz}} = 599 \pm 32$ μJy), while the others have fluxes in the range $70 \lesssim S_{1.4\mathrm{GHz}}$ (μJy) $\lesssim 160$ (see Table 5.1). For some other sources, instead, the measured noise is significantly higher ($\sigma_{\mathrm{rms}} > 50$ μJy), with respect to the theoretical one, due to side-lobe confusion by bright sources in the field. In particular, 4 sources – listed in Table 5.1 and marked with an asterisk ($*$) – present side-lobes so bright that it is very difficult to measure their fluxes and, for the moment, they will be considered as upper limits. The

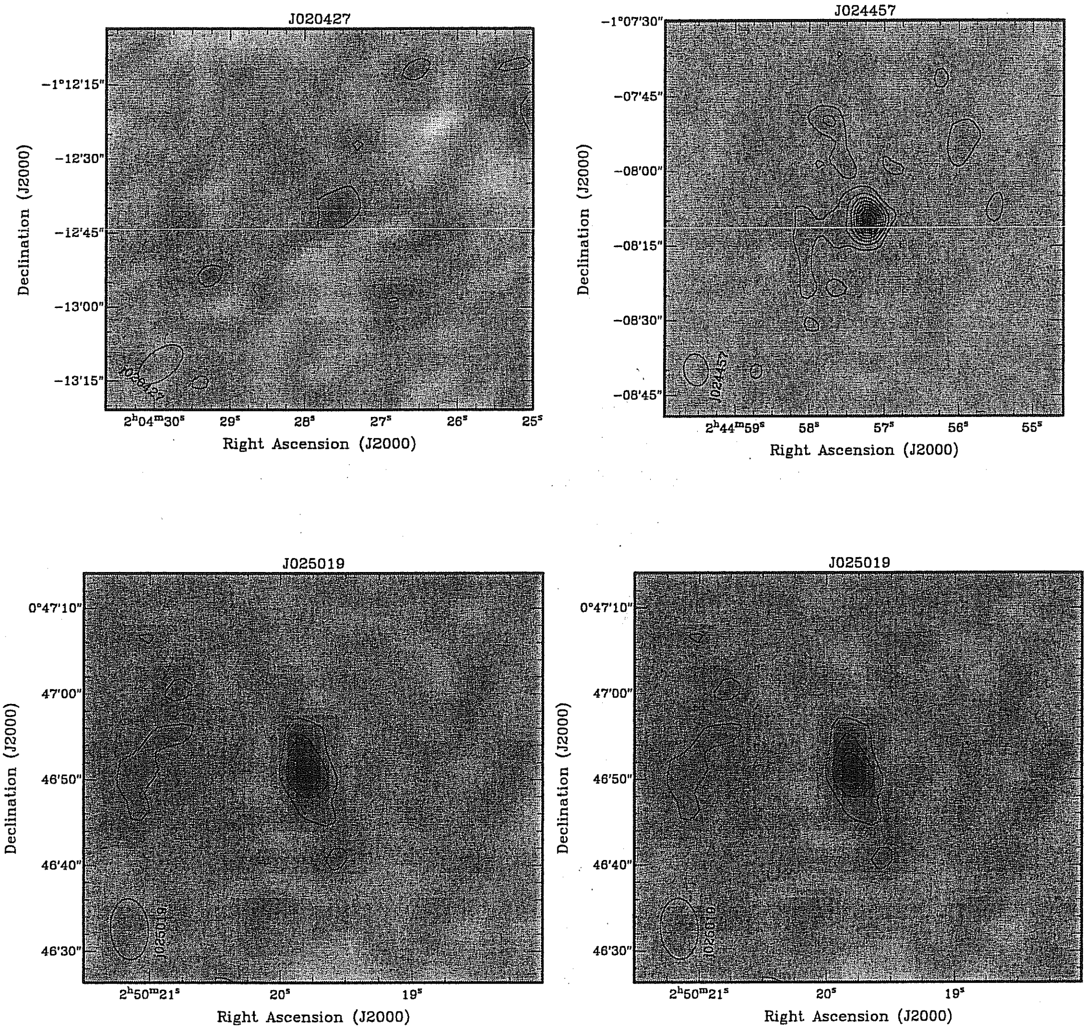

Figure 5.2: Images at 1.4 GHz of the 4 high redshift quasars detected at $> 3\sigma_{\rm rms}$. The FWHM of the Gaussian restoring beams are shown in the corners of all frames.

Source SDSS	z	AB_{1450}	M_{1450}	α_o	$S_{1.4\mathrm{GHz}}$ (μJy)
J001950.06-004040.9	4.32	19.62	-26.36	-0.02	155 ± 39
J005922.65+000301.4	4.16	19.30	-26.62	-1.09	<1000 ± 500 *
J010822.70+001147.9	3.71	19.62	-26.12	-0.19	<62 ± 31
J012019.99+000735.5	4.08	19.96	-25.93	-0.52	<84 ± 42
J012700.69-004559.1	4.06	18.28	-27.60	-0.66	<38 ± 19
J020427.81-011239.6	3.91	19.80	-26.02	-0.83	69 ± 19
J020731.68+010348.9	3.85	20.10	-25.70	-1.00	<48 ± 24
J023908.98-002121.5	3.74	19.60	-26.15	-0.78	<52 ± 26
J024457.19-010809.9	3.96	18.46	-27.38	-1.21	559 ± 32
J025019.78+004650.3	4.76	19.64	-26.49	-0.59	164 ± 19
J030707.46-001601.4	3.70	20.04	-25.69	-0.71	<58 ± 29
J031036.85+005521.7	3.77	19.25	-26.51	-0.64	<300 ± 150 *
J033910.53-003009.2	3.74	19.93	-25.82	-1.17	<58 ± 29
J035214.33-001941.1	4.18	19.51	-26.42	-0.16	<52 ± 26
J225452.88+004822.7	3.69	20.24	-25.49	-1.51	<72 ± 36
J225529.09-003433.4	4.08	20.26	-25.63	-1.15	<46 ± 23
J230323.77+001615.2	3.68	20.24	-25.48	-0.77	<76 ± 38
J230639.65+010855.2	3.64	19.14	-26.57	-1.38	<170 ± 85 *
J235053.55-004810.3	3.85	19.80	-26.00	-0.89	<100 ± 50 *

Table 5.1: Properties of the observed quasars. Redshift and optical data are from Fan et al. (2001a). Sources marked by an asterisk (*) have radio fluxes contaminated by side-lobes due to bright sources in the field.

remaining 11 sources still have $\sigma_{\rm rms} \sim 30 - 40$ μJy and are undetected at these flux levels. Radio fluxes for these sources will be treated as upper limits in the following. Therefore, more work is required to have a better cleaning of the images and a careful removal of all spurious signals, in order to reach the theoretical noise and improve detections.

5.4 Preliminary results

Even though data analysis is still incomplete, in this Section we try to outline some preliminary results. Quasars in the complete sample are optically bright (see Table 5.1), with absolute magnitudes $-25.5 \gtrsim M_B \gtrsim -29$. These blue magnitudes M_B have been computed from UV magnitudes (M_{1450}) using Eq. (5.4) and assuming, for each source, the optical spectral index α_o found by Fan et al. (2001a) and shown in Table 5.1.

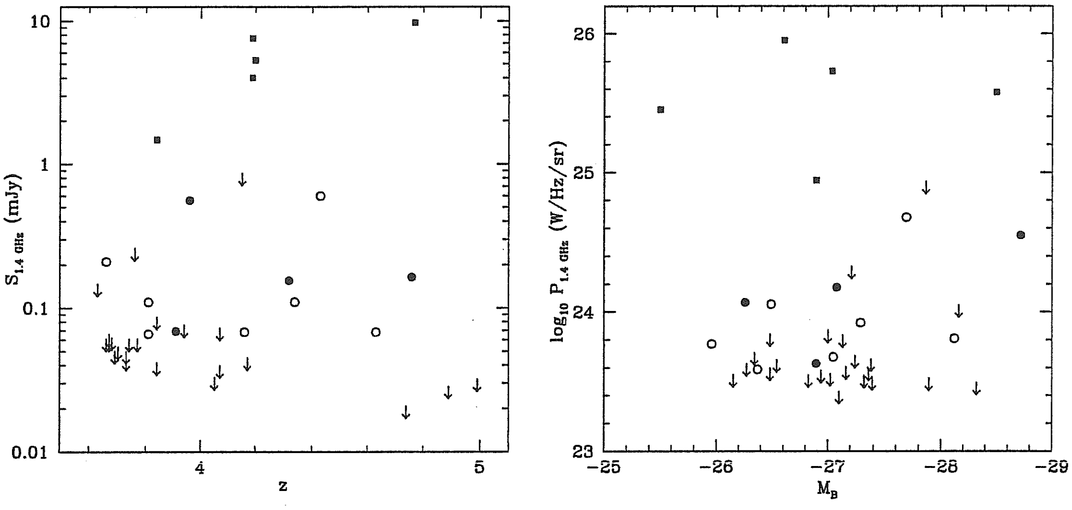

Figure 5.3: Radio flux versus redshift (left panel) and absolute magnitude versus radio power (right panel) for the 39 sources in the complete sample. Filled circles are the 4 detected sources from this work (see Table 5.1), open circles are sources detected at $> 2\sigma_{\rm rms}$ from Carilli et al. (2001) and squares are sources detected by FIRST survey (see text). Upper limits from both Carilli et al. and this work are drawn as arrows.

Radio detections of these high redshift quasars have been obtained down to $\sim$ 60 μJy, as shown in Figure 5.3. In fact, most of the undetected sources have upper limits lower than this value, except the four objects contaminated by side-lobes of bright sources in the field. Therefore, radio observations of such sample are roughly complete down to $S_{\rm 1.4GHz} \sim 60\,\mu$Jy. Radio powers of these sources – computed assuming radio spectral index $\alpha_R = 0.8$ – are in the range $23.5 \lesssim \log_{10}{\rm P}_{\rm 1.4GHz}\,({\rm W\,Hz^{-1}\,sr^{-1}}) \lesssim 26$, as shown in Figure 5.3.

In order to study radio loudness of these sources, in Figure 5.4, we show, as a solid histogram, the distribution of radio-to-optical ratios ($R^*_{1.4}$ defined in Chapter 2) for the 16 detected sources (5 from FIRST, 4 from our observations and 7 detected by Carilli et al. (2001) at $> 2\sigma_{\rm rms}$). In order to have an idea of the $R^*_{1.4}$ distribution of the whole sample, we plotted, as a dotted histogram, the distribution obtained from the undetected sources by using their upper limits. For comparison, it is also shown the distribution of radio-to-optical ratios obtained through our Monte Carlo analysis (Model A) of quasar samples at $z \lesssim 2$ and described in Chapter 3. This "theoretical" distribution has been normalized at

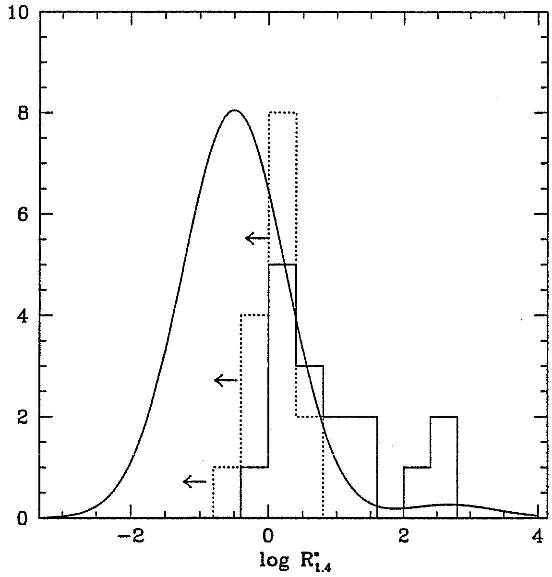

Figure 5.4: Distribution of radio-to-optical ratios for radio detected sources (solid histogram) and undetected ones (dotted histogram), for which upper limits in radio power have been used . The solid curve represent the $R^*_{1.4}$ distribution for Model A (see Table 3.3) obtained in Chapter 3 (see text for details).

the same number of sources in the observed sample.

Qualitatively, there is an overall good agreement between the data and the predicted $R^*_{1.4}$ distribution, at least for $R^*_{1.4} \lesssim 10$. In fact, data show a steep transition region between RL and RQ regime, as described in Chapter 3. In the radio loud regime, instead, there is some evidence for an excess of observed sources with respect to the model, even though the poor statistics does not allow us give a definitive answer. In fact, there are 5 sources with $S_{1.4\mathrm{GHz}} \gtrsim 1$ mJy, detected by FIRST, in this RL tail. Two of them have $R^*_{1.4} \sim 10$, close to the RL/RQ transition region and the other 3 have $R^*_{1.4} \gtrsim 100$. Therefore, due to the small number of sources, this result is still compatible – within statistical errors – with the theoretical distribution. Moreover, further uncertainties could arise from the choice of the radio spectral index. In fact, radio powers have been computed assuming for all sources $\alpha_R = 0.8$. Smaller values of the spectral index – as expected since at high redshift, observations at 1.4 GHz select the rest frame part of the spectrum at higher frequencies ($\sim$ 8 GHz), where the flat core-component dominates – will shift the observed

$R^*_{1.4}$ distribution towards lower values.

It is also worth noting that the comparison presented in Figure 5.4 does not take into account any selection effect, that can introduce severe uncertainties, as extensively described in Chapter 3. In order to improve these preliminary results, we are working to refine the analysis of the data, eventually applying an approach similar to the one presented in Chapter 3. In fact, Monte Carlo simulations will allow us to treat selection effects, related to observational limits, and have a better estimate of the uncertainties.

However, this preliminary analysis suggests for a possible increase of the fraction of radio loud quasars at high redshift, even though the overall radio properties of quasars do not show a strong cosmological evolution, from local Universe up to $z \sim 5$. This behaviour has also been inferred by observations at other wavelengths, more tightly related to accretion processes, such as optical and X-ray bands. In fact, it has been found that both high-energy properties of quasars and their optical to X-ray spectral indices do not show strong evolution with redshift, up to $z \sim 6$ (Brandt et al. 2003; Vignali et al. 2003). Therefore, physical conditions in the central regions – during the quasar shining phase – seem to be mainly related to intrinsic accretion processes ($M_{\rm BH}$, accretion rate, etc.), rather than cosmological effects.

5.5 A step forward ...

As a final remark, it is worth noting that multi-wavelength information are available for this high redshift sample. For all sources, SDSS provides optical photometry and spectroscopic data, while radio observations are available from our work and Carilli et al. (2001). Moreover, about half of the sources have also been observed at 250 GHz (Carilli et al. 2001), with HST and in near-IR within the 2 Micron All Sky Survey (2MASS). Finally, X-ray observations, with Chandra Observatory, are available for 7 of these sources (Vignali et al. 2003). In order to have information in mid (MIR) and far-Infra Red (FIR), we proposed, in collaboration with P. Andreani, observations with Spitzer Observatory of a sub-sample of 16 of such high redshift sources. These latter sources represent the high redshift tail of a sample of 67 AGN spanning the range $0.3 < z < 5$, proposed for Spitzer observations. Exploiting this wide redshift range, the aim is to study cosmological evolution of the dusty torus around quasars. In fact, this torus is able to absorb a fraction of the nuclear luminosity and thermally re-emit it in MIR/FIR. Moreover, multi-wavelength information will allow to build up the SED of quasars covering all the spectral regions relevant to the determination of the bolometric emission.

Chapter 6

A new Fundamental Plane for spheroidal galaxies

6.1 Introduction

Although the traditional approach to galaxy formation and evolution regards nuclear activity as an incidental diversion, it is becoming clear, beyond any reasonable doubt, that the formation of super-massive black holes powering nuclear activity is intimately linked to the formation of its host galaxy and plays a key role in shaping its evolution.

As discussed in Chapter 1, the presence of massive BH ($10^6 - 10^9 M_\odot$) in all local galaxies with a spheroidal component (Kormendy & Richstone 1995) and the tight correlations between the mass of these central objects and the large scale properties of spheroids – such as the velocity dispersion of stars (Magorrian et al. 1998), mass of the bulge (McLure & Dunlop 2002), mass of the dark matter halo (Ferrarese 2002) – support this connection.

Theoretical models proposed to explain these correlations are based on the idea that the accreting black hole grows in parallel with the bulge until some feedback – possibly quasar outflows – expels the gas and terminates the star formation (Silk & Rees 1998; Fabian 1999). This mutual feedback between galaxies and quasars during their early evolutionary stages may be the key to overcome some of the problems of the currently standard scenario for galaxy formation.

In the standard picture, most of the star formation occurs in relatively small galaxies that later merge to make bigger and bigger objects (White & Rees 1978; Kauffmann 1996). On the contrary, recent data indicate that galaxies detected by sub-mm surveys with SCUBA and MAMBO (Blain et al. 2002; Scott et al. 2002) are mostly very massive with very high star-formation rates ($\sim 10^3\ M_\odot\ yr^{-1}$) at relatively high redshift $z > 2$ (Dunlop 2001; Ivison et al. 2002; Chapman et al. 2003). The presence of such massive objects at high redshift has also been confirmed by recent K-band surveys (Cimatti et al. 2002; Kashikawa et al. 2003; Fontana et al. 2004).

Moreover, as already discussed in Chapter 1, other observational evidence – such as the color-magnitude relation (Ellis et al 1997; Bower et al. 1998; Kodama et al. 1998), the Fundamental Plane (Djorgovski & Davies 1987; Dressler et al. 1987; Treu et al. 2002), the α-enhancement (Trager et al. 2000a,b; Thomas et al. 2002) – suggest that the formation of spheroidal galaxies happened at high redshift in a substantial single burst and were followed by an essentially passive evolution phase.

However, this scheme is inadequate to the extent that it cannot be fitted in a consistent scenario for structure formation from primordial density fluctuations. In this Chapter we present a model for coevolution of galaxies and quasars able to reconcile theory and observations, accounting for most of the observed properties of spheroidal galaxies. In Section 2 we give a brief description of this model and its basic ingredients. Our predictions for the Fundamental Plane of spheroidal galaxies is presented in Section 3, while in Section 4 we explore the relations between the mass of the central BH and properties of its host galaxy. We discuss the results and introduce the concept of a "new Fundamental Plane" in Section 5.

Throughout this Chapter we will adopt a cold dark matter cosmology with cosmological constant, consistent with the Wilkinson Microwave Anisotropy Probe (WMAP) data (Bennett et al. 2003), as well as with information from large scale structure (Spergel et al. 2003): $\Omega_m = 0.29$, $\Omega_b = 0.047$, and $\Omega_\Lambda = 0.71$, $H_0 = 72$ km s^{-1}, $\sigma_8 = 0.8$, and an index $n = 1.0$ for the power spectrum of primordial density fluctuations.

6.2 A model for coevolution of spheroids and quasars

In this section we will introduce the basic ideas of a model for coevolution of spheroids and quasars. This model has been extensively described in Granato et al. (2004) and here we briefly recall its main properties and results.

Within dark matter (DM) halos, forming at a rate predicted by the canonical hierarchical clustering scenario, the diffuse gas falls into the potential well. Part of this gas can condensate forming stars, according to the local dynamical and cooling times. The radiation drag due to the star formation acts on the cold gas decreasing its angular momentum and causing an inflow into a reservoir around the central BH (Umemura 2001). This gas – through viscous processes – is accreted into the central BH, increasing its mass and powering the nuclear activity.

It is important to notice that the feedback – both from supernovae and active nuclei – plays a fundamental rule, heating the gas and possibly expelling it from the halo. The relative efficiency of feedbacks depends on the mass of the halo. In fact, in the shallower potential wells (corresponding to lower halo masses and, for a given mass, lower virialization redshifts), supernova heating is increasingly effective in slowing down the star formation and driving gas outflows. The more massive protogalaxies virializing at earlier times are thus the site of a fast star formation.

A higher star formation also implies a higher radiation drag, corresponding to a faster loss of angular momentum of the gas (Umemura 2001; Kawakatu & Umemura 2002) and, consequently, a larger accretion rate onto the central BH. In turn, the kinetic energy carried by outflows driven by active nuclei through line acceleration (Murray 1995) is sufficient to unbind the residual gas, thus halting both the star formation and the BH growth. The time required to sweep out the interstellar medium (ISM) is shorter for larger halos. For the most massive galaxies the gas unbinding time is short enough for the bulk of the star formation to be completed before Type Ia supernovae can substantially increase the iron abundance of the ISM, thus accounting for the α-enhancement seen in the largest galaxies. Furthermore, this model is also able to reproduce SCUBA number counts and their redshift distribution as well as the epoch-dependent K-band luminosity function of spheroidal galaxies (see Granato et al. 2004).

6.2.1 Dark matter halos

The following analysis has been performed in the framework of canonical hierarchical clustering scenario. Following Navarro et al. (1997) and Bullock et al. (2001) we identify as a virialized halo at redshift z a volume of the Universe of radius $R_{\rm vir}$ enclosing an overdensity $\Delta_{\rm vir}(z)$ which, for a flat cosmology, can be approximated by

$$\Delta_{\rm vir} \simeq \frac{(18\pi^2 + 82d - 39d^2)}{\Omega(z)}, \tag{6.1}$$

where $d = \Omega(z) - 1$ and $\Omega(z)$ is the ratio of the mean matter density to the critical density at redshift z (Bryan & Norman 1998). The halo mass is then given by

$$M_{\rm vir} = \frac{4\pi}{3}\Delta_{\rm vir}(z)\rho_u(z)R_{\rm vir}^3, \tag{6.2}$$

$\rho_u(z)$ being the mean universal matter density. It is also useful to define the rotational velocity of the DM halo at its virial radius as $V_{\rm vir}^2 = GM_{\rm vir}/R_{\rm vir}$. The virialized halos exhibit a universal density profile (Navarro et al. 1997; Bullock et al. 2001) well described by

$$\rho(r) = \frac{\rho_s}{c_{\rm vir}\, x(1 + c_{\rm vir}\, x)^2}, \tag{6.3}$$

hereafter called NFW, where $x = r/R_{\rm vir}$ and $c_{\rm vir}$ is the concentration parameter. Analyzing profiles of a large sample of virialized halos obtained through high-resolution N-body simulations, Bullock et al. (2001) found that, at any redshift, $c_{\rm vir}$ is a weak function of the mass ($c_{\rm vir} \propto M_{\rm vir}^{-0.13}$), while, at fixed mass, $c_{\rm vir} \propto (1+z)^{-1}$.

Numerical simulations and theoretical arguments show that the dark matter assembly in halos proceeds through a first phase of fast accretion, followed by a slow phase (Wechsler et al. 2002; van den Bosch 2002). Zhao et al. (2003) showed that the potential well of the halos is built up during the fast accretion. The subsequent slow accretion does not change the "identity" of the halo, though significantly increasing its mass. Guided by these results, in the following we will assume that, for the mass and redshift ranges we are interested in, the virialization epoch of DM halos coincides with the end of the fast accretion phase and with the beginning of the vigorous star formation of the proto-spheroidal galaxies, and that these galaxies keep their identity till the present time.

The formation rate of massive halos ($M_{\rm vir} \gtrsim 2.5 \times 10^{11}\, M_{\odot}$) at $z \gtrsim 1.5$ is approximated by the positive part of the time derivative of the halo mass function $n(M_{\rm vir}, z)$ (Haehnelt & Rees 1993; Sasaki 1994; Peacock 1999). The negative part is small for this mass and redshift range, consistent with our assumption that massive halos survive till the present time. Following Press & Schechter (1974) we write:

$$n(M_{\rm vir}, z) = \frac{\rho}{M_{\rm vir}^2} \nu f(\nu) \frac{d \ln \nu}{d \ln M_{\rm vir}} \tag{6.4}$$

where ρ is the average comoving density of the universe and $\nu = [\delta_c(z)/\sigma_\delta(M_{\rm vir})]^2$, σ_δ being the rms initial density fluctuations smoothed on a scale containing a mass $M_{\rm vir}$, and δ_c the critical over-density for spherical collapse. For the function $\nu f(\nu)$ we adopt the expression given by Sheth & Tormen (2002), which also takes into account the effect of ellipsoidal collapse:

$$\nu f(\nu) = A[1 + (a\nu)^{-p}](\frac{a\nu}{2})^{1/2} \frac{e^{-a\nu/2}}{\pi^{1/2}}, \tag{6.5}$$

where $A = 0.322$, $p = 0.3$ and $a = 0.707$.

6.2.2 Star-formation rate and Supernova feedback

As far as the effect of angular momentum can be neglected, as is probably the case for the formation of spheroidal galaxies, the collapse time of baryons within the host dark matter halo, $t_{\rm coll}$, is the maximum between the free-fall time,

$$t_{\rm dyn}(r) = [3\pi/32 G \rho(r)]^{1/2} \ , \tag{6.6}$$

and the cooling time

$$t_{\rm cool}(r) = \frac{3}{2} \frac{\rho_{\rm gas}(r)}{\mu m_p} \frac{kT}{C n_e^2(r) \Lambda(T)} \ , \tag{6.7}$$

both computed at the virial time $t_{\rm vir}$. In the above equations ρ is the total matter density, $\rho_{\rm gas}$ is the gas density, n_e is the electron density, $\Lambda(T)$ is the cooling function and $C = \langle n_e^2(r)\rangle / \langle n_e(r)\rangle^2$ is the clumping factor, assumed constant. In the following we adopt the cooling function given by Sutherland & Dopita (1993), which includes the dependence on metal abundance.

We consider a single-zone galaxy with three gas phases: diffuse gas in the outer regions, with mass $M_{\rm inf}(t)$, infalling on a dynamical timescale, cool gas with mass $M_{\rm cold}(t)$, available to form stars, and hot gas with mass $M_{\rm hot}(t)$, eventually outflowing. At the virialization we assume that $M_{\rm inf}(t_{\rm vir}) = f_b M_{\rm vir}$, with $f_b = 0.16$, the universal ratio of baryons to DM (Bennett et al. 2003; Spergel et al. 2003). The infalling gas, initially at the equilibrium temperature in the DM potential well, is transferred to the cool star-forming phase at a rate:

$$\dot{M}_{\rm cold}(t) = M_{\rm inf}(t)/max[t_{\rm cool}(R_{\rm vir}), t_{\rm dyn}(R_{\rm vir})]. \tag{6.8}$$

The star formation rate (SFR) is given by:

$$\psi(t) = \int_0^{R_{\rm vir}} \frac{1}{max[t_{\rm cool}(r), t_{\rm dyn}(r)]} \frac{{\rm d}M_{\rm cold}(r,t)}{{\rm d}r} {\rm d}r, \tag{6.9}$$

where we assume that the cold gas distribution still follows the DM distribution. This assumption is admittedly quite unrealistic since cold cloudlets should rather fall towards the center. However, a realistic modeling of the cold gas distribution would be too ambitious at the present stage.

Although the Initial Mass Function (IMF) may depend on the physical properties of the gas, such as density and metallicity (see Eisenhauer 2001 and references therein), it is often assumed to be independent of time and galaxy mass. We will consider in the following the IMF preferred by Romano et al (2002) on the basis of chemical abundances in local ellipticals, i.e. $\Phi(M) \propto M^{-0.4}$ for $M \leq 1\ M_\odot$ and $\Phi(M) \propto M^{-1.25}$ for $1\,M_\odot < M \leq 100\,M_\odot$.

The feedback due to supernova (SN) explosions moves the gas from the cold to the hot phase at a rate:

$$\dot{M}^{\rm SN}_{\rm cold} = -\frac{2}{3}\psi(t)\, \epsilon_{\rm SN}\, \frac{\eta_{\rm SN} E_{\rm SN}}{\sigma^2}, \tag{6.10}$$

where $\eta_{\rm SN}$ is the number of Type II SNe expected per solar mass of formed stars (determined by the IMF, adopting a minimum progenitor mass of $8\,M_\odot$), $E_{\rm SN}$ is the kinetic energy of the ejecta from each supernova (10^{51} erg; e.g. Woosley & Weaver 1986), and $\epsilon_{\rm SN}$ is the fraction of this energy which is used to reheat the cold gas. Analysis show that about 90% of the SN kinetic energy may be lost by radiative cooling (Thornton et al. 1998; Heckman et al. 2000); we adopt $\epsilon_{\rm SN} = 0.05$ as our reference value, consistent with the results by Mac Low & Ferrara (1999) and Wada & Venkatesan (2003).

6.2.3 Black-hole growth and Quasar feedback

As discussed by Haiman et al. (2004), the available information on the evolution of both the global star formation rate and the quasar emissivity is broadly consistent with the hypothesis that star formation in spheroids and black-hole (BH) fueling are proportional to one another.

One mechanism yielding such proportionality has been discussed by Umemura (2001), Kawakatu & Umemura (2002) and Kawakatu et al. (2003). In the central regions of proto-galaxies the drag due to stellar radiation may result in a loss of angular momentum of the gas at a rate that in a clumpy medium is well approximated by

$$\frac{d ln J}{dt} \simeq \frac{L_{\rm sph}}{c^2 M_{\rm gas}}(1 - e^{-\tau}) \ , \tag{6.11}$$

where $L_{\rm sph}$ is the global stellar luminosity and τ is the effective optical depth of the spheroid, parameterized as:

$$\tau = \tau_0 \left(\frac{Z}{Z_\odot}\right) \left(\frac{M_{\rm gas}}{10^{12} M_\odot}\right)^{\frac{1}{3}} , \tag{6.12}$$

where Z is the mean metallicity at a given time. For τ_0 it has been explored the range from 1 to 10, adopting 4 as a reference value.

The gas can then flow towards the center, feeding a mass reservoir around the BH at a rate (Kawakatu et al. 2003)

$$\dot{M}_{\rm inflow} \simeq -M_{\rm gas}\frac{d ln J}{dt} \simeq \left(\frac{L_{\rm sph}}{c^2}\right)(1 - e^{-\tau}) \ . \tag{6.13}$$

During the early evolutionary stages the luminosity is dominated by massive main sequence stars, $M \geq 5 M_\odot$, and is thus proportional to the star formation rate $\psi(t)$.

Therefore, material, infalling at the rate given by Eq. (6.13), accumulates in a circum-nuclear mass reservoir, and then flows toward the black hole – assumed to grow from a seed of $10^3 M_\odot$ – on a time scale depending on the viscous drag $\tau_{\rm visc}$. Following Duschl et al. (2000) and Burkert & Silk (2001) we adopt a viscosity $\nu = \mathcal{R}_{\rm crit}^{-1} v_w$, where $\mathcal{R}_{\rm crit} = 100$–$1000$ is the critical Reynolds number for the onset of turbulence. With these assumptions the viscous time can be expressed as $\tau_{\rm visc} = \tau_{\rm dyn} \mathcal{R}_{\rm crit}$. The dynamical time $\tau_{\rm dyn} = (3\pi/32 G \rho_{\rm res})^{1/2}$ is referred to the system 'black hole plus reservoir'.

The accretion radius of the BH is given by $r_a = GM_{\rm BH}/V_{\rm vir}^2$. Defining the reservoir dimension $R_{\rm res} = \alpha_{\rm res} r_a$, we estimate $\rho_{\rm res}$ as the mean density within a sphere of radius $R_{\rm res}$ with mass $M_{\rm BH} + M_{\rm res}$, to get:

$$\tau_{\rm dyn} = \pi \left(\frac{\alpha_{\rm res}}{2}\right)^{3/2} \frac{G}{V_{\rm vir}^3} \frac{M_{\rm BH}^{3/2}}{(M_{\rm BH} + M_{\rm res})^{1/2}}. \tag{6.14}$$

The viscous accretion rate onto the BH can be defined as

$$\dot{M}_{\rm BH}^{\rm visc} = \frac{M_{\rm res}}{\tau_{\rm visc}} = k_{\rm accr} \frac{\sigma^3}{G} \left(\frac{M_{\rm res}}{M_{\rm BH}}\right)^{3/2} \left(1 + \frac{M_{\rm BH}}{M_{\rm res}}\right)^{1/2}. \tag{6.15}$$

The constant $k_{\rm accr} = [\pi(\alpha_{\rm res}/2)^{3/2}(V_{\rm vir}/\sigma)^3 \mathcal{R}_{\rm crit}]^{-1}$ has a rather wide range of possible values. For $\mathcal{R}_{\rm crit} = 100$ and $\alpha_{\rm res} = 10$ we have $k_{\rm accr} \sim 10^{-4}$ that we adopt as the reference value in the following. The maximum allowed accretion rate has been limited to be at most mildly super-Eddington, i.e. $3 \times \dot{\rm M}_{\rm Edd}$.

When the mass of the central BH is grown enough, the QSO activity affects the surrounding intergalactic medium through both the radiative output and the injection of kinetic energy producing powerful gas outflows, as discussed in Chapter 1.

Following Silk & Rees (1998), the kinetic power in the outflow is $L_K = 1/2\dot{M}_w v_\infty^2$ (see Section 1.8.2), where v_∞ (Eq. 1.6) is the asymptotic wind speed from Murray et al. (1995). If f_c is the covering factor of the outflow and using $\dot{M}_w = 4\pi r^2 \rho(r) v_w \sim 4\pi r f_c m_H N_H v_\infty$, we get

$$\dot{M}_w \simeq 2.6 f_c N_{22} \left(\frac{L_{\rm Edd}}{10^{46}\ {\rm erg\ s^{-1}}}\right)^{1/2} \left(\frac{r_f}{10^{16}\ {\rm cm}}\right)^{1/2} \quad M_\odot\, {\rm yr}^{-1} \tag{6.16}$$

where $N_{22} = N_H/10^{22}\,{\rm cm}^{-2}$. The asymptotic speed is reached at $r \gtrsim 40 r_f$, where r_f is the radius at which the wind is launched. Adopting $r_f = 1.5 \times 10^{16}$ cm as a reference value, as discussed in Section 1.4.1, the kinetic power in the outflow is

$$L_K = \frac{1}{2}\dot{M}_w v_\infty^2 \simeq 3.6 \times 10^{44} f_c N_{22} \left(\frac{L_{\rm Edd}}{10^{46}\ {\rm erg\ s^{-1}}}\right)^{3/2} \quad {\rm erg\ s^{-1}}, \tag{6.17}$$

that may thus amount to several percent of the accretion luminosity for highly luminous QSOs. Estimating the fraction of this kinetic luminosity transferred to the interstellar medium is a rather complex problem. However, both simulations (Brüggen et al. 2002) and observations (Enßlin & Kaiser 2000; Inoue & Sasaki 2001; Bicknell et al. 1997; Nath

& Roychowdhury 2002) suggest this fraction (f_h) to be of the order of 40-50%. We assume that the QSO feedback heats up the interstellar medium and removes it from the cold phase at a rate:

$$\dot{M}_{\rm cold}^{\rm QSO} = -\frac{2}{3}\frac{f_h L_K}{\sigma^2}\frac{M_{\rm cold}}{M_{\rm gas}} , \tag{6.18}$$

where $M_{\rm gas} = M_{\rm cold} + M_{\rm inf}$ is the mass of the gas in the cold phase plus that of the gas which has not yet fallen in the star forming region. Setting $\epsilon_{\rm QSO} = (f_h/0.5)(f_c/0.1)(N_{22}/10)$, we get

$$\dot{M}_{\rm cold}^{\rm QSO} \simeq -2\times 10^3 \frac{\epsilon_{\rm QSO} L_{\rm Edd,46}^{3/2}}{(\sigma/300\,{\rm km\,s^{-1}})^2}\frac{M_{\rm cold}}{M_{\rm gas}}\ M_\odot\,{\rm yr}^{-1} , \tag{6.19}$$

We have explored the range $1 \leq \epsilon_{\rm QSO} \leq 10$, adopting $\epsilon_{\rm QSO} = 6$ as our reference value.

6.3 Properties of early type galaxies

In the framework of the model described in the previous Section, we aim at exploring the main properties of spheroidal galaxies and their central massive BH, not discussed in Granato et al. (2004). Many of the observational properties of elliptical galaxies are related to three observational quantities: luminosity L, velocity dispersion σ and effective radius R_e, which determine the so called "Fundamental Plane" (Djorgovski & Davies 1987; Dressler et al. 1987). Both the effective radius and velocity dispersion are related to dynamical properties of the system. In fact, R_e is defined as the radius containing half of the light and it is clearly related to collapse processes settling on the baryonic component at the center of the dark matter potential. Also the line-of-sight velocity dispersion σ – through out this work measured at $R_e/8$ – is a measure of the potential well in the inner regions. The Fundamental Plane relates these dynamical quantities to photometric ones – such as the luminosity or surface brightness – constituting one of the main tools to study the properties of spheroidal galaxies.

In the following Sections we will investigate the relations between these various observables in order to test all the components of the Fundamental Plane.

6.3.1 The Faber - Jackson relation

The first relation we want to explore is the one between the luminosity and the central velocity dispersion, the so called Faber-Jackson relation (Faber & Jackson 1976). In fact, since the first measurements of velocity dispersion were made, it was recognized that in early type galaxies these two quantities are correlated (Poveda 1961; Minkowski 1962; Faber & Jackson 1976). In particular, for this work we will refer to the recent determination by Bernardi et al. (2003), obtained by using a sample of $\sim$ 9000 early type galaxies drawn from the Sloan Digital Sky Survey (SDSS) in the redshift range $0.01 \leq z \leq 0.3$. Their observed relation for absolute magnitudes in r^* band is shown in Figure 6.1. The scaling they found is: $L \propto \sigma^{3.92}$ in the r^* band, consistent with previous studies (Forbes & Ponman 1999; Pahre et al. 1998). This relation is roughly independent of wavelength and the distributions around the mean, at a fixed luminosity, are approximately Gaussian in shape (Bernardi et al. 2003).

From a theoretical point of view, in order to reproduce this relation both luminosities and velocity dispersions must be determined by the model. For a given halo mass $M_{\rm vir}$ virializing at redshift $z_{\rm vir}$ we are able to follow the time evolution of the baryonic component both in the gas and stellar phase, as described in Granato et al. (2004). Then, the luminosity in a given band can be computed as a function of cosmic time by using the spectrophotometric code GRASIL (Silva et al. 1998).

The second step is to compute the velocity dispersion. However, the model we are dealing with is a single zone model and cannot give us any information about the dynamics of the system. A way to overcome this problem is to relate σ to the virial velocity of the DM halo ($V_{\rm vir}$) computed at the virialization epoch (Bullock et al. 2001):

$$V_{\rm vir} = 75\,(1 + \rm z_{vir})^{1/2} \left(\frac{\rm M_{vir}}{10^{11} h^{-1} M_{\odot}}\right)^{1/3} \ \rm km\,s^{-1} \tag{6.20}$$

Some hints toward this direction come from observations. A slightly non linear relation between the circular velocity V_c and the central velocity dispersion in spheroidal systems has been found by Ferrarese (2002):

$$\log(\rm V_c) = (0.84 \pm 0.09)\,\log(\sigma) + (0.55 \pm 0.19). \tag{6.21}$$

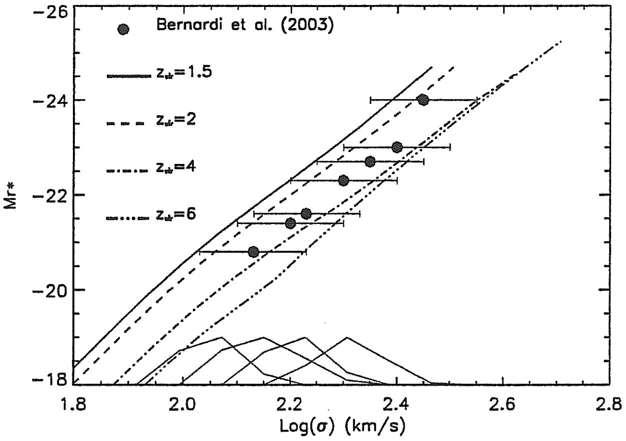

Figure 6.1: Observed Faber-Jackson relation (filled dots) from Bernardi et al. (2003), compared with our predictions for different virialization redshifts $z_{\rm vir}$. The curves at the bottom of the figure represent the predicted distribution of σ at a fixed luminosity with an arbitrary scale (see text for details).

This relation has been obtained by using a sample of 16 spirals and 20 elliptical galaxies. Velocity profiles for these elliptical galaxies have been estimated by Kronawitter et al. (2000) and Gerhard et al. (2001). The flat regime of the rotation curve for several of these sources has been reached in the range $0.5 \lesssim R/R_e \lesssim 2.6$ allowing for a reasonable measurement of the circular velocity, even though with a large scatter of the order of 15-20 per cent. However, it is worth noting that the uncertain contribution of baryonic matter within R_e, with respect to the DM, could also affect this measure. As already said, the scaling relation in Eq. (6.21) has been obtained by combining both spiral and elliptical galaxies, while, by considering only the latter population, the relation is even more linear (Ferrarese 2002) and well approximated by forcing a linear fit with:

$$\sigma = (0.65 \pm 0.02) V_c. \tag{6.22}$$

The observed Faber-Jackson relation can be well reproduced by our model by using $0.50 \lesssim \sigma/{\rm V_{vir}} \lesssim 0.65$. In Figure 6.1 it is shown, for different virialization redshifts, the predicted Faber-Jackson relation by assuming: $\sigma/{\rm V_{vir}}$ =0.55. The uncertainties in the value of $\sigma/{\rm V_{vir}}$ are mainly related to the large scatter in the data. However, it is interesting to notice that this scatter in the observed relation can be interpreted as an intrinsic property of elliptical galaxies. In fact, it can be simply accounted by different virialization epochs.

Sources with the same spheroidal luminosity, but virializing at lower redshifts, show lower velocity dispersions (see Figure 6.1). The curves at the bottom of this Figure represent the scatter in σ at a fixed luminosity as obtained from our model in arbitrary units. For a given luminosity we computed velocity dispersions for all the $M_{\rm vir}$ and $z_{\rm vir}$ contributing to that luminosity, each one weighted in number according to the halo formation rate. The distributions in velocity dispersion obtained for four different luminosities – showed in Figure – are roughly Guassians, with the peak close to the σ expected from the best fit relation and in agreement with the observed distribution obtained by Bernardi et al. (2003).

6.3.2 Local Luminosity Function

In order to double check the reliability of our predictions, and in particular the determination of the luminosities used to build up the Faber-Jackson relation, we used luminosities, as obtained from our model, to compute the local Luminosity Function (LF) of spheroids. The predicted LF at $z = 0$ in the r^* band is shown in Figure 6.2 and compared with the recent determination obtained by Bernardi et al. (2003) exploiting the same SDSS data used to derive the Faber-Jackson relation. The agreement is remarkably good in the bright luminosity regime ($M_{r^*} \lesssim -20.5$) sampled by the data. This observed LF has been computed by using only early type galaxies, while in our model we also include the contribution from bulges of late type galaxies. In fact, as shown by Nakamura et al. (2002) the contribution of spiral galaxies to the LF starts dominating for $M_{r^*} \gtrsim -21$. However, it is not obvious how to separate the contribution from bulges and disks in late type spirals. In order to have a rough comparison, in Figure 6.2 we show the total LF (early + late) derived by Nakamura et al. (2002) to have at least an upper limit to the spheroidal LF. It is clear from the Figure that our predictions in the faint luminosity regime are fully consistent with the observed data. The agreement is even better if we correct the LF of late type spirals by considering only the bulge luminosity, assuming, for example, that this latter is ~ 30 per cent of the total luminosity, as suggested by Fukugita et al. (1998).

Before moving on, it is important to make some comments on the assumptions introduced to relate the central velocity dispersion σ to the virial velocity $V_{\rm vir}$. The first

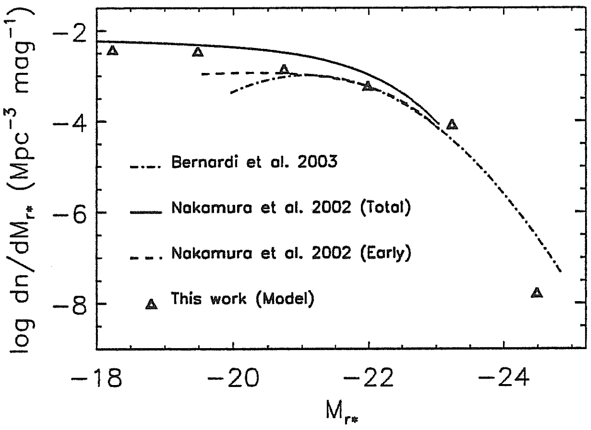

Figure 6.2: Predicted LF of local spheroidal galaxies (open triangles) compared with the one derived by Bernardi et al. (2003) for early type galaxies selected from SDSS (dot-dashed line). It has also been plotted the local LF derived by Nakamura et al. (2002) for early type galaxies (dashed line) and for the total (early + late) population (solid line).

point worth stressing is that $V_{\rm vir}$ is computed at the virializing redshift $z_{\rm vir}$, while the velocity dispersion is a quantity determined locally, at $z \sim 0$. The collapse of baryons through the DM potential could alter the virial velocity making: $V_{\rm vir}\,(z=0) \neq V_{\rm vir}\,(z_{\rm vir}\,)$. However as already said, numerical simulations show that the DM assembly in halos proceeds through a first phase of fast accretion, followed by a slow phase that does not change the main properties of the halo (Wechsler et al. 2002; van deb Bosch 2002; Zhao et al. 2003). The importance of the baryonic component in affecting the halo profile was also pointed out by El-Zant et al. (2001). These authors considered the possibility that the interaction between gas clouds and DM can erase the central cusp in the halo, however, even this process does not affect the circular velocity in the external regions.

Another important issue is that observations allow to measure the circular velocity V_c, at the maximum of the rotation curve (Kronawitter et al. 2000), and not the virial velocity. However, it is possible to relate these two quantities by assuming a shape for the density profile of DM. By using the Navarro, Frank & White (1997) profile and typical values for the concentration parameter ($c_{\rm vir}$ in the range 5-10) the scaling relation is $1 \lesssim V_c/V_{\rm vir} \lesssim 1.2$ (Bullock et al. 2001). Therefore, the choice of a direct relation between σ and $V_{\rm vir}$ seems to be reasonable and not affected by severe uncertainties.

6.3.3 Velocity dispersion function

Exploiting the success of our model in reproducing both the Faber-Jackson relation and the local luminosity function of spheroidal galaxies, we made a step forward looking at the local galaxy velocity dispersion function (VDF). In fact, the usual method to estimate this function is to transform a luminosity distribution ($\phi(L)$) into a velocity function simply as $\phi(V_c) = \phi(L)|dL/dV_c|$, following a Tully & Fischer (1977) correlation between luminosity L in a given band and circular velocity V_c for spiral galaxies, and a Faber & Jackson (1976) correlation between luminosity and velocity dispersion σ for early type galaxies (Shimasaku 1993; Gonzalez et al. 2000; see also Kochanek 2001 for a comprehensive review).

Such a procedure however ignores the scatter of the relation between the luminosity and the dynamical variables, which has the cumulative effect of underestimating objects with large velocities. Sheth et al. (2003), exploiting the data from the Sloan survey, derived the local ($z < 0.3$) early type galaxy velocity dispersion function (see Figure 6.3), taking into account the spread of the Faber-Jackson relation around the best fit relationship.

More recently Shankar et al. (2004), exploitating SDSS data by Bernardi et al. (2003), have used them to derive a bivariate distribution. The resulting VDF is shown in Figure 6.3 as a shaded area. The uncertainties are bigger toward the two extremes, where the number of sampled objects decreases. However, the VDF derived by Shankar et al. (2004) and Sheth et al. (2003) agree remarkably well, except for the low velocity dispersion regime. The more rapid decline found by Sheth et al. (2003) is due to selection criteria adopted by Bernardi et al. (2003) in computing the LF in the low luminosity regime (see Figure 6.2) with respect to the LF derived by Nakamura et al. (2002) and used by Shankar et al. (2004) to derive the VDF.

From the theoretical point of view, the VDF can be reproduced without the combination of the LF and Faber-Jackson relation. In fact, for each halo with $M_{\rm vir}$ and $z_{\rm vir}$ the velocity dispersion is derived from $V_{\rm vir}$ (by applying the linear scaling relation $\sigma/V_{\rm vir}$) and the number density is obtained from the time derivative of the Press-Schecter, which determines the formation rates of DM halos as a function of mass and redshift.

The comparison between the observed and predicted VDF puts more cogent con-

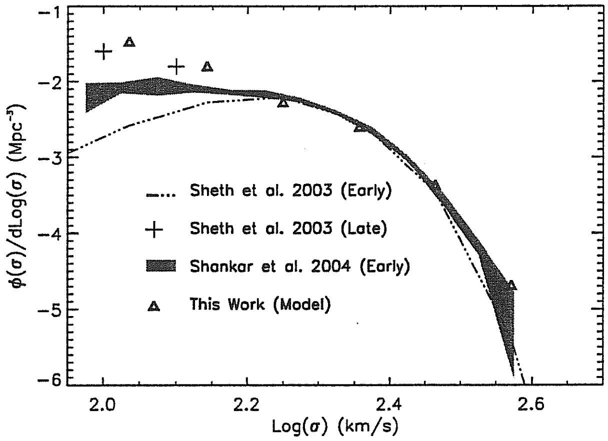

Figure 6.3: The observed velocity dispersion function for early type galaxies from Shankar et al. (2004) (shaded area) and Sheth et al. (2003) (triple-dot dashed line) compared with our predictions (open triangles). Crosses show the contribution of late type galaxy bulges as determined by Sheth et al. (2003).

straints on the assumed relation between $V_{\rm vir}$ and σ. It is clear from the Figure 6.3 that the spread in the VDF is much less than in the Faber-Jackson relation, in particular around the knee of the function ($2.2 \lesssim \log_{10}(\sigma) \lesssim 2.5$), allowing for a more precise determination of the scaling relation. As discussed in the previous section, the Faber-Jackson relation is well reproduced by assuming $0.5 \lesssim \sigma/{\rm V_{vir}} \lesssim 0.65$. The VDF, and in particular its tail at high dispersion velocities, is indeed more sensitive to the value of this ratio. We find that the VDF can be fitted by a narrower range of the scaling relation: $0.55 \lesssim \sigma/{\rm V_{vir}} \lesssim 0.6$. These values are lower than the one (0.65 ± 0.02) found by Ferrarese (2000). However as already said, the uncertainties related to both observational and theoretical approaches are large, and the discrepancy between these determinations is only of the order of 10 per cent. Finally, it is worth to notice that Di Matteo et al. (2003) by using cosmological hydrodynamic simulations found an even lower value – of the order of 0.5 – for this scaling relation.

It is worth noting that Figure 6.3 also shows that our predictions exceed, for $\log_{10}(\sigma) \lesssim 2.2$, the observed VDF, as derived by Shankar et al. (2004) and Sheth et al. (2003). In order to compute VDF, these authors only considered the contribution coming from early type galaxies, while our model also contains spiral bulges. As already discussed for the LF, the contribution of spirals starts dominating at low luminosities and therefore at low σ, according to the Faber-Jackson relation. In Figure 6.3 we plot as crosses an estimate of the VDF for late type galaxy bulges, derived by Sheth et al. (2003). It is clear that these bulge components dominate the VDF in the low σ regime, in agreement with our predictions.

As a final remark we want to stress that results presented in previous sections refer to DM halos with mass in the range $2.5 \times 10^{11} M_{\odot} \lesssim M_{\rm vir} \lesssim 1.6 \times 10^{13} M_{\odot}$ formed at $z_{\rm vir} \gtrsim 1.5$. As discussed in Granato et al. (2004), this lower limit to the virialization redshift is a way to crudely cut out halos hosting disks and irregular galaxies. Late-virialized objects, in our view, had more time to acquire a substantial angular momentum ending up with a disk structure and are less likely to take on an early type morphology. Limits on virial masses are free parameters, even though physically reasonable. However, we can put tight constraints on them. In particular, the bright end, of both LF and VDF, is very sensible to the choice of the upper bound. By considering virial masses $M_{\rm vir} \gtrsim 1.6 \times 10^{13} M_{\odot}$ the predicted LF and VDF exceed, in the bright end, the observed determinations by more than a factor 10. However, we are still testing the effects of other cosmological parameters, such as the value of σ_8 or the minimum $z_{\rm vir}$, etc.

6.3.4 Completing the Fundamental Plane

An additional check of the global physical processes involving baryons can be derived from the observed $L - R_e$ relation (see e.g. Bernardi et al 2003). The effective radius, as the velocity dispersion, is related to the collapse and settling of the baryonic component inside the DM potential well. On the other hand the model we are using does not give us dynamical information, as mentioned above. However, on one side the model yields the total mass in stars and dark remnants, while observations ensure that the stellar light distribution is rather standard in spheroids. In fact the surface brightness distribution is well represented by $\log I(r) \propto r^{1/n}$ (Sersic 1969); the classical de Vaucouleurs profile has n=1/4 (de Vaucouleurs 1948). In the case of de Vaucouleurs profile, Borriello et al (2003) have carefully computed the expected central velocity dispersion properly taking into account the light distribution, the traced by light mass and the dark matter. As a result it is possible to compute the effective radius as

$$R_e = (k_\sigma + \alpha_{\rm DM}) \frac{GM_{\rm sph}}{\sigma^2}, \tag{6.23}$$

where $M_{\rm sph}$ is the total mass in the galaxy traced by the light, k_σ is a constant depending on light distribution (k_σ=0.174 for the $r^{1/4}$ law) and $\alpha_{\rm DM}$ is a function of the DM mass inside R_e and of its density distribution (see Eqs 13 and 14 in Borriello et al. 2003). As found by Gebhardt et al (2001) for a sample of about 20 elliptical galaxies and generalized by Borriello et al (2003) on the basis of the narrowness of the Fundamental Plane, the DM inside the effective radius amounts to only 10-50% of the total mass. Such an amount and its distribution make $\alpha_{\rm DM}$ almost negligible in the above equation, that can be rearranged as follows, by using the definition of $V_{\rm vir}$ (Eq. ??):

$$\frac{R_e}{R_{\rm vir}} = (k_\sigma + \alpha_{\rm DM}) \frac{M_{\rm sph}/M_{\rm vir}}{(\sigma/V_{\rm vir})^2}, \tag{6.24}$$

The AHBC model yields the $M_{\rm sph}/M_{\rm vir}$ ratio and the ensuing $M_{\rm sph}/L$, which significantly depends on the adopted IMF. With the reference Salpeter's law $\frac{M_{\rm sph}}{L_r} \simeq 5$ with very little dependence on the luminosity in the reference r^* band. On the other hand the dependence of M/L ratio on luminosity is a well defined property of spheroidal galaxies, though the origin is still debated (see e.g. Ciotti et al. 1996). Bernardi et al (2003), exploiting the large sample of early-type galaxies in the SDSS, defined an effective mass $M_0 \equiv 4R_e\sigma^2/G$, and found $M_0/L_r = 3.5(\frac{L_r}{L_r^*})^{0.15}$ with $L_r^* = 2. \times 10^{10}$. On the other hand following Eq. 6.23 the total mass traced by light is given by

$$M_{\rm sph} = \frac{1}{(k_\sigma + \alpha_{\rm DM})} \frac{R_e\sigma^2}{G}, \tag{6.25}$$

Analyzing the SDSS data with the above equation with k_σ=0.174 appropriate for $r^{1/4}$ law and assuming negligible contribution from DM, i.e.$\alpha_{\rm DM} \ll k$, the M/L ratio becomes

$$\frac{M}{L_r} = 5.1 * (\frac{L_r}{L_r^*})^{0.14}. \tag{6.26}$$

This result is in very close agreement with the findings of Borriello et al (2003) on a much smaller sample with more detailed observations. It is plausible that a major part of the increase of the M/L ratio with luminosity has to be attributed to deviation from homology,

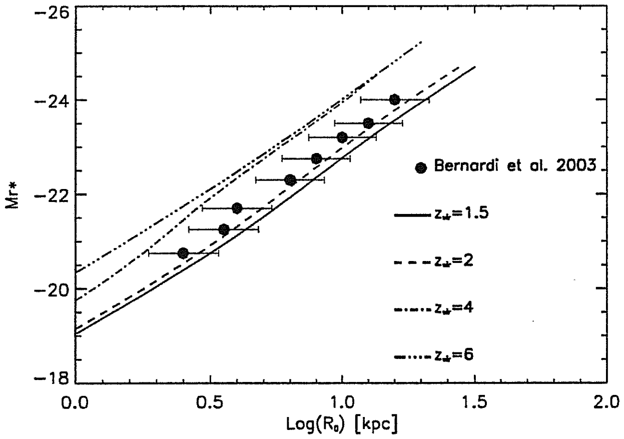

Figure 6.4: Observed R_e versus absolute magnitude in r^* band (filled dots) from Bernardi et al. (2003) compared with our model predictions for different virialization redshifts.

i.e. $k_\sigma = f(M_{\rm sph})$, as suggested by the correlation of n parameter of the Sersic law with luminosity (Ciotti et al 1996; Graham et al. 2001; Trujillo et al. 2004). If so, we can insert the dependence found from the observations in the 'structure' parameter k_σ obtaining from eq6.24 and eq6.26

$$\frac{R_e}{R_{\rm vir}} \simeq 0.87\,(\frac{L_r}{L_r^*})^{0.14}\,\frac{L_r/M_{\rm vir}}{(\sigma/V_{\rm vir})^2}. \tag{6.27}$$

In Figure 6.4 we show the above relationship with $L_r/M_{\rm vir}$ taken from the AHBC model (Salpeter IMF) and $\sigma/V_{\rm vir} = 0.56$ as derived from the VDF. The presence of an average ~30% of DM inside R_e would imply $\alpha_{\rm DM} \leq 0.02$ (see Borriello et al 2003) and would not modify the fit to the data. The agreement with data suggests that the model determines the proper $L_r/M_{\rm vir}$ ratio. However the adoption of Salpeter IMF is just a reference. It is very likely that in order to reproduce not only the M/L ratio, but also the observed color-magnitude relation and the relations among the spectral indices, a more sophisticated treatment of the IMF is required, with a possible dependence on evolving parameters, such as chemical abundances.

6.4 The central BH

In previous sections it has been shown that the model we have presented can reasonably account for the Fundamental Plane of spheroidal galaxies. Now, we aim at

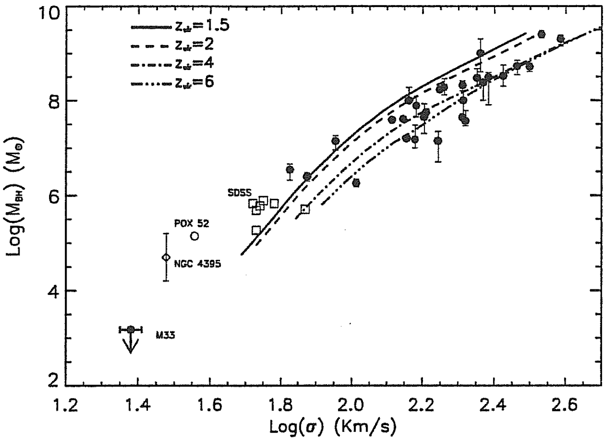

Figure 6.5: The $M_{\rm BH} - \sigma$ relation from our model for different virialization redshifts compared with observational data. Filled circles represents nearby galaxies with dynamical measurements of the BH mass (Tremaine et al. 2002) as well as the upper limits to M33 (Gebhardt et al. 2001). With open symbols are shown sources with BH masses estimated by using the line width-luminosity-mass scaling relation as NGC 4395 (open diamond; Filippenko & Ho 2003), POX 52 (open circle; Barth et al. 2004) and a sample of 7 sources drawn from SDSS (open squares) presented as a preliminary result by Greene et al. (2004).

exploring the tight correlations between the properties of spheroidal galaxies and the mass of their central BH. As discussed in Chapter 1, tight relations have been discovered between the $M_{\rm BH}$ and the velocity dispersion of stars (Magorrian et al 1998; Ferrarese & Merritt 2000; Gebhardt et al. 2000; Tremaine et al. 2002), the mass of the spheroidal component (McLure & Dunlop 2002; Dunlop et al. 2003; Marconi & Hunt 2003), and the mass of the dark halo (Ferrarese 2002).

In this section, we will focus on the $M_{\rm BH} - \sigma$, and compare observational data with predictions from our model. For a given $M_{\rm vir}$ and $z_{\rm vir}$ we are able to follow the growth of the central BH and estimate its final mass. As in the cases of the DVF and Faber-Jackson relation, we exploit the relation $0.55 \lesssim \sigma/{\rm V_{vir}} \lesssim 0.6$, in order to obtain the central velocity dispersion. In Figure 6.5 it has been plotted the $M_{\rm BH} - \sigma$ relation derived from our model for different virialization redshifts. For comparison, we also show the observed relation for objects with dynamical measurements of the BH mass (filled symbols), from Tremaine et al. (2002). The spread in the observed relation is, in our view, not only due to observational uncertainties, but comes as an effect of different virialization epochs. It is

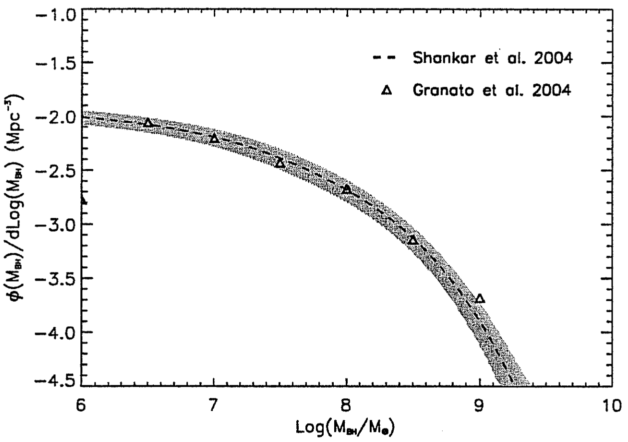

Figure 6.6: Predicted local BH mass function (empty triangles) compared with the recent determination (shaded area) by Shankar et al. (2004).

interesting to notice that the model also predicts a steepening of the relation at lower values of σ. This is due to the combined effect of SN feedback – which is increasingly efficient with decreasing halo mass in slowing down the gas infall onto the central BH – and of the decreased radiation drag (due to a decrease of the optical depth). This steepening of the lower part of the $M_{\rm BH}$–σ relationship can also be translated into a not constant ratio between $M_{\rm BH}$ and the mass in stars. In fact, this ratio is of the order of $\sim 10^{-2.5}$ at the higher virial masses and drops to $\sim 10^{-3.5}$ at $M_{\rm vir} \sim 10^{11} M_{\odot}$, decreasing even more for low virialization redshifts. As extensively discussed in the next Section, this behaviour of the $M_{\rm BH}$–σ relationship also implies a flattening of the lower part of the $M_{\rm vir}$–$M_{\rm BH}$ correlation, in agreement with the results reported in Fig. 5 of Ferrarese (2002).

From the observational point of view the behaviour of the $M_{\rm BH}$–σ relation in the low BH mass and low velocity dispersion regime is still unclear, due to the paucity of the data and the uncertainties related to the $M_{\rm BH}$ estimates. In order to shed light on this issue in Figure 6.5 we plot – as open symbols – sources found in literature having $M_{\rm BH} \lesssim 10^6 M_{\odot}$. For these sources dynamical measurements are not available and the BH masses have been estimated by using the line width-luminosity-mass scaling relation (Kaspi et al. 2000), except for M33. The case of this latter source – a bulge less late type spiral galaxy – is very interesting. The upper limit to its BH mass is $M_{\rm BH} \lesssim 3000 M_{\odot}$ (Merritt et al. 2001) or

$M_{\rm BH} \lesssim 1500 M_\odot$, as suggested by Gebhardt et al. (2001). In both cases, it falls well below the linear extrapolation of the $M_{\rm BH}$–σ relation derived at higher σ (Ferrarese & Merritt 2000; Gebhardt et al. 2000; Tremaine et al. 2002), while it is fully consistent with the predictions of our model. On the other hand BH mass estimates of type 1 Seyfert galaxies as NGC 4395 (Filippenko & Ho 2003), POX 52 (Barth et al. 2004) and a sample of 7 sources drawn from SDSS (Greene et al. 2004) are only marginally consistent with the steepening predicted by our model, while they are consistent with the linear extrapolation of the $M_{\rm BH}$–σ relation. In order to fully constrain the very low σ (< 50 km s^{-1}) end of the $M_{\rm BH}$–σ relation more efforts are required to detect the so called intermediate mass BHs ($10^3 M_\odot \lesssim M_{\rm BH} \lesssim 10^6 M_\odot$) in the galactic centers (see van der Marel 2003 for a comprehensive review).

Another interesting point related to the growth of the central BH and its influence on the galaxy formation is the presence of such dark massive objects in the center of all local galaxies with a spheroidal component (Kormendy & Richstone 1995). Recently, it has been possible to estimate the local BH mass function (Marconi et al. 2004; Shankar et al. 2004), by exploiting the $M_{\rm BH} - \sigma$ relation as well as the relation of the $M_{\rm BH}$ with the bulge luminosity. Figure 6.6 shows the determination of the local BH mass function derived by Shankar et al. (2004), as a shaded area. It is also plotted the predicted mass function obtained from our model, which is found to be in very good agreement with the observed one.

6.5 Discussion

The first point worth stressing is the amazing connection between the central BH and the formation of its host galaxy. In fact, the relative feedback between star formation and AGN activity, is able to reconcile a monolithic scenario for the formation of spheroidal galaxies – as suggested by observations – with the hierarchical CDM framework. Due to these feedbacks and halo properties, the formation of stars and of the central BH took place on shorter timescales within more massive DM halos. As described in Granato et al. (2004), this scenario is able to reproduce the population of high redshift massive galaxies detected by sub-mm and K-band surveys as well as the observed α-enhancement in massive ellipticals.

In this work it has been shown that this reversed behaviour of baryons (*Anti-hierarchical Baryon Collapse*) with respect to DM, is also able to account for both photometric and dynamical properties of local spheroidal galaxies. Under the simple assumption of a linear scaling relation between the central velocity dispersion and the virial velocity ($0.55 \lesssim \sigma/\mathrm{V}_{\mathrm{vir}} \lesssim 0.6$), the model is able to reproduce the Faber-Jackson relation and the velocity dispersion function of local spheroidal galaxies. The model has been tested against the local luminosity function, showing a good agreement with the data. A reasonable fit has also been obtained for the relation between luminosity and effective radius, achieving in this way all the properties of the Fundamental Plane.

The feedback from supernovae and nuclear activity also determines the observed relationships between the black-hole mass and the large scale properties of the host galaxy. Model predictions are in excellent agreement with the observed $M_{\mathrm{BH}} - \sigma$ relation, as well as the local black-hole mass function.

It is worth noting that the observable quantities related into this Fundamental Plane are ultimately linked to the mass of the spheroidal component and in the end to the potential well, inside the effective radius. In fact, luminosity traces the mass in stars, while R_e and σ are related to the central potential, since the quantity $R_e\sigma^2$ represents an estimate of the mass inside the light radius.

Therefore, let us consider these three fundamental masses involved in galaxy formation: the mass of dark matter halos (M_{vir}), the mass in stars (M_{sph}) and the mass of the central BH (M_{BH}). We will show that there are tight correlations between these quantities, forming a three-dimensional surface, a sort of "new Fundamental Plane" for spheroidal galaxies. Even though these masses cover a huge dynamical range – from few light-days around the hole up to Mpc scales – they are linked together via reciprocal feedbacks acting on the baryonic component. In Figure 6.7 the orthogonal projections of this 3D surface are presented.

The first relation we want to consider is the one between M_{vir} and M_{sph}. In the case in which only stellar feedback is considered, the expected relation scales as $M_{\mathrm{vir}} \propto M_{\mathrm{sph}}^{2/3}$, as suggested by Romano et al. (2002). The introduction of the quasar feedback produces a steepening of the relation, as shown in Figure 6.7. For $M_{\rm vir} \gtrsim 10^{12}\ M_\odot$ (or equivalently $M_{\rm sph} \gtrsim 3 \times 10^{10}\ M_\odot$) this effect is clear and larger at lower virialization redshifts. In fact, since $V^2_{\rm vir} \propto (1 + z_{\rm vir})$, lower $z_{\rm vir}$ implies lower potential well, at a given $M_{\rm vir}$. Therefore, feedbacks are more efficient in sweeping the gas, reducing the mass that can be converted into stars.

Feedbacks and halo properties also control the growth of the central BH. As shown in the upper-right panel of Figure 6.7, there is a tight relation between $M_{\rm vir}$ and $M_{\rm BH}$, that reflects the $M_{\rm BH} - \sigma$ relation. Also in this case, the scatter in the relation is intrinsic and due to different virialization redshifts. However, the scatter in the $M_{\rm vir}$-$M_{\rm BH}$ relation is reduced by a factor ~ 2 with respect to the $M_{\rm BH} - \sigma$ relation, as also pointed out by Ferrarese (2002). The analysis of a sample of local elliptical galaxies presented by Ferrarese (2002) also shows that $M_{\rm BH} \propto M_{\rm vir}^{1.65-1.82}$ which is consistent – at least for $M_{\rm vir} \gtrsim 10^{12}\ M_\odot$ – with our findings. At lower $M_{\rm vir}$ we predict, as in the case of the $M_{\rm BH} - \sigma$ relation, a steepening due to the increasingly efficiency of stellar feedback with respect to quasar one.

It is interesting to notice that the scatter due to different virialization epochs disappears when the relation between $M_{\rm BH}$ and $M_{\rm sph}$ is considered. In fact, as shown in the upper-left panel of Figure 6.7, we predict a very tight relation between these quantities with a scatter $\lesssim 0.1$ dex. Feedbacks, both stellar and nuclear, act in the same way on $M_{\rm sph}$ and $M_{\rm BH}$, independently on the epoch of virialization. It is worth stressing that there are two main effects governing the growth processes and ultimately this “new Fundamental Plane”. The first one is that in large DM potentials star formation is high and fast, favouring the growth of the stellar component, and therefore higher $M_{\rm sph}$. At the same time high star formation rates also imply high radiation drag, with a consequent larger growth of the central BH.

However, this process also represents the “beginning of the end”, because quasar feedback, produced by the activity of such larger BHs, is able – even in these large objects – to unbind the gas, halting both star formation and BH growth. This feedback freezes the $M_{\rm BH}$ and $M_{\rm sph}$ – except for a passive stellar evolution for this latter component – and creates the tight relation between these masses. However, uncertainties related to the choice of the initial mass function (IMF) and in particular its dependence on redshift and mass of

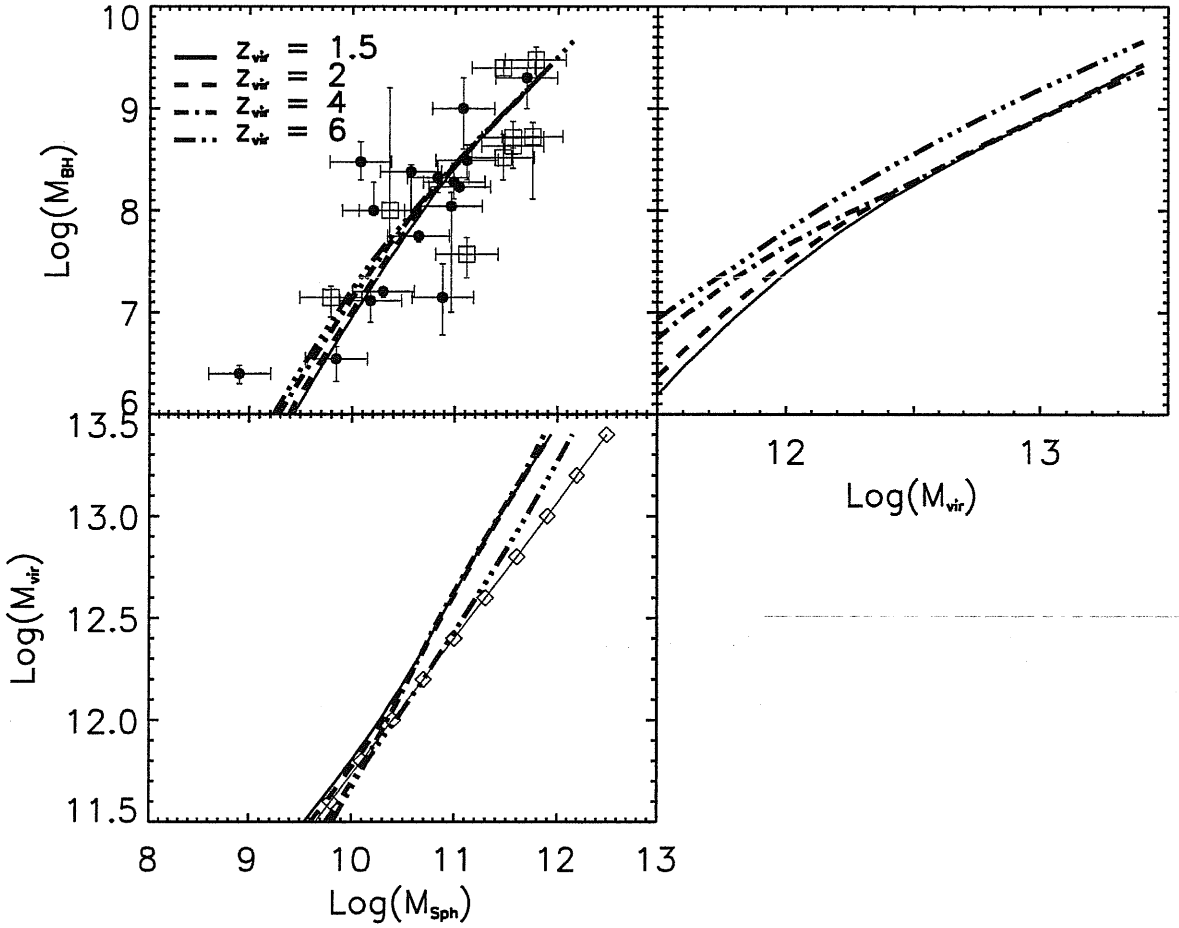

Figure 6.7: Orthogonal projections of the "new Fundamental Plane". In the upper-left panel the predicted $M_{\rm BH}$ -$M_{\rm sph}$ relation for different virialization redshifts is presented and compared with observational data from Häring & Rix (2004). Open squares are sources from their Group 1 and solid circles from their Group 2. The upper-right and lower left panels show the $M_{\rm vir}$-$M_{\rm BH}$ and $M_{\rm vir}$-$M_{\rm sph}$ relations, respectively. Open diamonds connected with a thin solid line represent the scaling relation $M_{\rm vir} \propto M_{\rm sph}^{2/3}$ as suggested by Romano et al. (2002).

virialization could introduce some spread in this relation.

Finally, we want to remark that, even from the observational point of view, there is evidence for a tighter linear correlation between $M_{\rm BH}$ and $M_{\rm sph}$. In fact, Marconi & Hunt (2003) have recently found that the scatter in this relation is reduced to ~ 0.25 dex, when $M_{\rm sph}$ is estimated as a virial mass ($\sim R_e\sigma^2$). In the upper-left panel of Figure 6.7 we plotted for comparison the $M_{\rm BH}$ -$M_{\rm sph}$ relation for objects with reliable bulge mass determination from Häring & Rix (2004). The agreement between the data – that show $M_{\rm BH} \propto M_{\rm sph}^{1.12}$ – with our predictions is remarkably good, even though the scatter in the data is large. However, as suggested by Häring & Rix (2004) this scatter is $\lesssim 0.3$ dex, and a considerable fraction of this spread can be attributed to measurement errors.

Chapter 7

Conclusions

One of the major challenges for modern astrophysics is to trace the evolution of the Universe from the formation of the first stars, in the so called "dark age", to the present epoch, explaining a variety of structures, from galaxies to clusters. The key question is to understand how and when the luminous matter collapsed assembling galaxies inside the framework of cold dark matter (CDM) hierarchical scenario. In recent years, it is also becoming clear that the nuclear activity – even though neglected for long time – could play a key role in these formation processes, as suggested by several observational evidence and discussed in Chapter 1.

One of the most spectacular signs of the AGN activity are, without a doubt, relativistic jets. In the first part of this thesis, we tackled this issue by studying the cosmological evolution of AGN – from local Universe up to $z \sim 5$ – as traced by radio properties of jets. In the second part, we directly dealt with the question of galaxy formation. We presented a model for the coevolution of quasars and spheroidal galaxies, in which AGN feedback – namely quasar winds – is a fundamental ingredient in shaping galaxy formation and evolution.

The first issue we tackled was the long debated question of radio loudness, trying to answer the question: is there a dichotomy in the radio properties of quasars? And, if this is the case, what is its origin? We started from an observational approach presenting, in Chapter 2, a detailed analysis of a new sample of radio-detected quasars, obtained by matching together objects from the FIRST and 2dF Quasar Redshift Surveys. The novelty of this dataset is that it allowed to explore radio properties of faint quasars – both in the radio and optical bands – due to the faint observational limits of both surveys. We found these objects to exhibit properties, such as redshift and colour distribution, in full agreement with those derived for the whole quasar population, suggestive of an independence of the mechanism(s) controlling the birth and life-time of quasars of their level of radio emission.

The analysis of this sample, coupled with an homogeneous one drawn from the Large Bright Quasar Survey, allowed to rule out the classical radio loud/radio quiet dichotomy, in which the distribution of radio-to-optical ratios and/or radio luminosities shows a lack of sources for $R^*_{1.4} \sim 30$. We also found a large spread between optical and radio luminosities for sources in the considered samples, result that tends to exclude the mass of the quasar black hole as the main physical quantity associated to the level of radio emission.

However, selection effects – i.e. limiting optical magnitudes and radio fluxes or coupling different samples – could introduce severe uncertainties in previous results. Therefore, awaiting for a wide-area surveys able to probe the whole radio/optical regime, we adopted a new approach to tackle the issue of radio loudness in quasars, presented in Chapter 3. We constrained a (simple) prescription for the intrinsic distribution of radio-to-optical ratios by comparing properties of Monte Carlo simulated samples with those of observed optically selected quasars, chosen to cover the widest range in radio loudness.

This analysis allowed us to determine an intrinsic distribution of radio properties of quasars, able to satisfy all the observational constraints. This distribution in the radio-to-optical ratios shows a peak at $R^*_{1.4} \sim 0.3$, with only $\lesssim 5$ per cent of objects being included in a high $R^*_{1.4}$ tail which identifies the radio loud regime. No lack or deficit of sources – but only a steep transition region – is present between the radio loud and radio quiet populations at any $R^*_{1.4}$.

A recent re-analysis of a sample of $\sim 10,000$ radio quasars obtained from the joined use of FIRST and SDSS (Ivezic et al. 2003), supports our result. In fact, the $R^*_{1.4}$ distribution found by these authors is in good agreement with the intrinsic distribution we obtained.

Another point worth stressing is that in order to reproduce the data, a dependence of the radio luminosity on the optical one is needed, even though with a large scatter. This dependence and the particular shape of the $R^*_{1.4}$ distribution also explain the observed dependence of the fraction of radio loud quasars on apparent and absolute optical magnitudes, simply as a selection effect related to the radio and optical limits of current surveys.

Exploiting the large dataset of quasars, $\sim$ 350 sources, drawn from the final releases of both FIRST and 2dF QSO Redshift Survey, in Chapter 4 we also studied the cosmological evolution of radio quasars. In particular, the faint radio and optical observational limits of the sample allowed us to explore for the first time the faint end of the radio and optical luminosity functions up to $z = 2.2$. We found indications ($\sim 3\sigma$) of a negative evolution for these faint sources at $z > 1.8$, both in the radio and optical bands. This corresponds to a decrement in the space density of faint quasars of about a factor 2 at z=2.2 and confirms the presence of a differential evolution for the population of radio-active quasars. We also explored the connection between quasars and radio galaxies within the unification scheme for AGN. The progressive decrease in the fraction of quasars in the whole radio source population can be consistently accounted for within the 'receding torus' scenario. The population of low luminosity quasars, which this new sample started picking up, approaches the transition region between FRII and FRI sources, and appears to depart from the 'classical' scheme for radio-loud quasars. In this light, we are investigating evolutionary properties of jets, studying in particular the role of different ignition and duration times of the mechanisms responsible for optical and radio emission, in shaping radio loudness in quasars.

We also extended our studies of radio loudness up to higher redshift, presenting in Chapter 5 preliminary results obtained from deep VLA observations of a complete sample of quasar drawn from SDSS. The analysis of these high redshift quasars – even though very preliminary – suggests that radio properties of quasars do not show strong cosmological evolution. In fact, the distribution of radio-to-optical ratios derived for this complete sample resembles the one obtained at $z \lesssim 2$, even though a more refined analysis is needed.

Exploiting these deep radio observations our aim is also to derive, for the first time, the high redshift QSO Radio Luminosity Function (at least in its bright end) and thus constrain the cosmological evolution of radio properties up to $z \sim 5$. Moreover, it will be interesting to gather a more general view of the evolution of accretion process by investigating statistical properties at different wavelengths (radio, optical/UV, X-ray). In fact, in the near future well defined LFs – over all the electromagnetic spectrum – will be available up to the highest redshifts.

Indeed recent discoveries at high redshift motivated the last part of this thesis. In fact, the model for coevolution of quasars and massive spheroids, described in Chapter 6, aims at explaining the discovery of a large population of massive galaxies at $z \sim 2$, detected by sub-mm and K-band surveys, and the findings of tight connections between the central BH and its host galaxy. These observations suggest that the formation of stars and of the central black hole took place on shorter timescales within more massive dark matter halos. In other words, the canonical hierarchical CDM scheme - small clumps collapse first - is reversed for baryon collapse and the formation of luminous objects (*Anti-hierarchical Baryon Collapse* scenario). This behavior, can be attributed to the feedback from supernova explosions and, for the most massive galaxies, from nuclear activity, and it is able to account simultaneously for evolutionary properties of quasars and of massive spheroidal galaxies.

In this work it has been shown that this reversed behaviour of baryons, with respect to DM, is also able to account for both photometric and dynamical properties of local spheroidal galaxies. Under the simple assumption of a linear scaling relation between the central velocity dispersion and the virial velocity ($0.55 \lesssim \sigma/\mathrm{V_{vir}} \lesssim 0.6$), the model is able to reproduce the Faber-Jackson relation and the velocity dispersion function of local spheroidal galaxies. The model has been tested against the local luminosity function, showing a good agreement with the data. A reasonable fit has also been obtained for the relation between luminosity and effective radius, accounting in this way for all the properties of the Fundamental Plane.

The feedback from supernovae and nuclear activity also determines the observed relationships between the black-hole mass and the large scale properties of the host galaxy. Model predictions are in excellent agreement with the observed $M_{\rm BH} - \sigma$ relation, as well as with the local black-hole mass function.

Therefore, we also introduced the idea of a sort of "new Fundamental Plane" for spheroidal galaxies, relating three fundamental masses involved in galaxy formation: the mass of dark matter halos ($M_{\rm vir}$), the mass in stars ($M_{\rm sph}$) and the mass of the central BH ($M_{\rm BH}$). Even though these masses cover a huge dynamical range – from few light-days around the central black hole up to Mpc scales – they are linked together via reciprocal feedbacks acting on the baryonic component.

Another key prediction of the model is a time delay between the major event of star formation (SCUBA phase) and the subsequent quasar shining phase. This latter process halts both star formation and BH growth, leaving stars to an essentially passive evolution phase (ERO phase). Some hints towards this direction come from X-ray observations. In fact, *Chandra* showed that only a very small fraction ($\sim$ 5%) of SCUBA galaxies have quasar luminosities, even though a larger fraction ($\gtrsim$ 40%) hosts low luminosity AGNs (Alexander et al. 2003), as expected if the central BH is still growing. In order to shed light on this evolutionary sequence, it will be interesting to study nuclear activity in sources in a later stage of evolution with respect to SCUBA galaxies, with reduced star formation, but with the nucleus still obscured at optical wavelengths (i.e. Mignoli et al. 2004). Therefore, we proposed *Chandra* observations of a sample of bright near-infrared ($K \leq 15.5$) and heavily reddened ($B - K \geq 6.5$) sources, in order to trace an evolutionary path from the dust-enshrouded to the dust-free phase.

Bibliography

[1] Abramowicz M.A., Czerny B., Lasota J. P., Szuszkiewicz, E., 1988, ApJ, 332, 646

[2] Abramowicz M.A., Chen X., Kato S., Lasota J., Regev O., 1995, ApJ, 438, L37

[3] Abramowicz M.A., Lasota J., Igumenshchev I.V., 2000, MNRAS, 314, 775

[4] Agol E. & Krolik J.H., 2000, ApJ, 528, 161

[5] Arav N., Li Z., Begelman, M.C., 1994, ApJ, 432, 62

[6] Aretxaga, I., Hughes, D.H., Chapin, E.L., Gaztanaga, E., Dunlop J.S., Ivison, R. 2003, MNRAS, 342, 759

[7] Balbus S.A. & Hawley J.F., 1991, ApJ, 376, 214

[8] Balbus S.A. & Hawley J.F., 1998, Rev. Mod. Phys., 70, 1

[9] Barth A.J., Ho L.C., Rutledge R.E., Sargent W.L.W., 2004, ApJ, 607, 90

[10] Baugh C.M., Cole S., Frenk C.S., 1996, MNRAS, 283, 1361

[11] Baugh C.M., Cole S., Frenk C.S., Lacey C.G., 1998, ApJ, 498, 504

[12] Becker R.H., White R.L., Helfand D.J., 1995, ApJ, 450, 559

[13] Begelman M.C. & Meier D.L., 1982, ApJ, 253, 873

[14] Begelman, M.C. 2003, in Carnegie Observatories Astrophysics Series, Vol. 1: Coevolution of Black Holes and Galaxies, ed. L.C. Ho (Cambridge: Cambridge Univ. Press), in press, astro-ph/0303040

[15] Beloborodov A.M., 1998, MNRAS, 297, 739

[16] Bennett C.L., et al. 2003, ApJ, 583, 1

[17] Bernardi M., Sheth R.K., Annis J., Burles S., Eisenstein D.J., et al., 2003, AJ, 125, 1849

[18] Bicknell G.V., Dopita M.A., O'Dea C.P.O., 1997, ApJ, 485, 112

[19] Blaes O.M., 2002, in Les Houches Lect. Notes 78, in press, astro-ph/0211368

[20] Blain, A.W., Smail, I., Ivison, R.J., Kneib, J.-P., Frayer, D.T., 2002, PhR, 369, 111

[21] Blandford R.D. & Znajek R.L. 1977, MNRAS, 179, 433

[22] Blandford R.D. & Payne D.G., 1982, MNRAS, 199, 883

[23] Blandford R.D.& Begelman M.C., 1999, MNRAS, 303, L1

[24] Blandford R.D., 2000, PTRSA, astro-ph/0001499

[25] Blumenthal G. R., Faber S. M., Primack J. R., Rees, M. J., 1984, Nature, 311, 517

[26] Blundell K.M. & Beasley A.J., 1998, MNRAS, 299, 165

[27] Blundell K.M. & Rawlings S., 2001, ApJ, 562, 5

[28] Borriello A., Salucci P., Danese L., 2003, MNRAS, 341, 1109

[29] Bower R. G., Lucey J. R., Ellis R. S. 1992, MNRAS, 254, 601

[30] Bower R.G., Kodama T., Terlevich, A., 1998, MNRAS, 299, 1193

[31] Boyle B.J., Shanks T., Peterson B.A., 1988, MNRAS, 235, 935

[32] Boyle B.J., Shanks T., Croom S.M., Smith R.J., Miller L., Loaring N., Heymans C., 2000, MNRAS, 317, 1014

[33] Brandt W.N., & Gallagher S.C. 2000, NewAR, 44, 461

[34] Brandt, W.N., Gallagher, S.C., & Kaspi, S. 2001, in New Century of X-ray Astronomy, ed. H. Inoue & H. Kunieda (ASP Conf. Ser. 251; S. Francisco: ASP), 128

[35] Brandt, W.N., Vignali C., Schneider D.P., Alexander D.M., Anderson S.F., et al. 2003, in New X-ray Results from Clusters of Galaxies and Black Holes, eds. C. Done, E.M. Puchnarewicz, M.J. Ward, astro-ph/0212082

[36] Brotherton M.S., Tran H.D., Becker R.H., Gregg M.D., Laurent-Muehleisen S.A., White R.L., 2001, ApJ, 546, 775

[37] Brüggen M., Kaiser C.R., Churazov E., Enßlin, T.A., 2002, MNRAS, 331, 545

[38] Bryan G.L., & Norman M.L., 1998, ApJ, 495, 80

[39] Bullock, J.S., Kolatt, T.S., Sigad, Y., Somerville, R.S., Kravtsov, A.V., Klypin, A.A., Primack, J.R., Dekel, A. 2001, MNRAS, 321, 559

[40] Burkert A. & Silk J., 2001, ApJ, 554, L151

[41] Carilli C.L., Bertoldi F., Rupen M.P., Fan X., Strauss M.A., et al., 2001, ApJ, 555, 625

[42] Celotti A. & Fabian A. C., 1993, MNRAS, 264, 228

[43] Celotti A., Padovani P., Ghisellini G. 1997, MNRAS, 286, 415

[44] Chapman, S.C., Scott, D., Borys, C., Fahlman, G.G. 2002, MNRAS, 330, 92

[45] Chartas G., Brandt W.N., Gallagher S.C., 2003, ApJ, 595, 85

[46] Chartas G., Brandt W.N., Gallagher S.C., Garmire G.P. 2002, ApJ, 579, 169

[47] Cimatti A., et al. 2002, A&A, 391, L1

[48] Cirasuolo M., Magliocchetti M., Celotti A., Danese L., 2003a, MNRAS, 341, 993

[49] Cirasuolo M., Celotti A., Magliocchetti M., Danese L., 2003b, MNRAS, 346, 447

[50] Cole S., Aragón-Salamanca A., Frenk C.S., Navarro J.F., Zepf S.E., 1994, MNRAS, 271, 781

[51] Cole S., Lacey C.G., Baugh C.M., Frenk C.S., 2000, MNRAS, 319, 168

[52] Condon J.J., O'Dell S.L., Puschell J.J., & Stein W.A. 1981, ApJ, 246, 624

[53] Condon J.J., Cotton W.D., Greisen E. W., Yin Q.F., Perley R.A., Taylor G.B., Broderick J.J., 1998, AJ, 115, 1693

[54] Crawford C.S., Gandhi P., Fabian A.C., Wilman R.J., Johnstone R.M., Barger A.J., Cowie L.L., 2002, MNRAS, 333, 809

[55] Cristiani S., Alexander D.M., Bauer F., Brandt W.N., Chatzichristou E.T., et al., 2004, ApJ, 600, 119

[56] Croom S.M., Smith R.J., Boyle B.J., Shanks T., Loaring N.S., Miller L., Lewis I.J., 2001, MNRAS, 322, L29

[57] Croom S.M., Schade D., Boyle B.J., Shanks T., Miller L., Smith R.J., 2004, ApJ, 606, 126

[58] D'Odorico V., Cristiani S., Romano D., Granato G.L., Danese L., 2004, MNRAS, 351, 976

[59] Dekel A. & Silk J., 1986, ApJ, 303, 39

[60] Di Matteo T., Croft R.A.C., Springel V., Hernquist L., 2003, ApJ, 593, 56

[61] Djorgovski, S. G., & Davis, M. 1987, ApJ, 313, 59

[62] Dressler, A., Lynden-Bell, D., Burstein, D., Davies, R. L., Faber, S. M., Terlevich, R, Wegner G. 1987, ApJ, 313, 42

[63] Dunlop J.S. & Peacock J.A., 1990, MNRAS, 247, 19

[64] Dunlop J.S. 2001, NewAR, 45, 609

[65] Dunlop J.S., 1998, in Bremer M.N., et al., eds., Observational Cosmology with the New Radio Surveys. Kluwer

[66] Dunlop J.S., McLure R.J., Kukula M.J., Baum S.A., O'Dea C.P., Hughes D.H., 2003, MNRAS, 340, 1095

[67] Duschl W.J., Strittmatter P.A., Biermann P.L., 2000, A&A, 357, 1123

[68] Egami E., Neugebauer G., Soifer B.T., Matthews K., Ressler M., Becklin E.E., Murphy T.W. Jr., Dale D.A. 2000, ApJ, 535, 561

[69] Eggen O.J., Lynden-Bell D., & Sandage A. 1962, ApJ, 136, 748

[70] Eisenhauer F., 2001, in Science with the Large Binocular Telescope, ed. T. Herbst, (Neumann Druck), 89

[71] Ellingson E., Yee H.K.C., Green R.F., 1991, ApJ, 371, 49

[72] Ellis R. S., Smail I., Dressler A., Couch W. J., Oemler A., Butcher H., & Sharples R. M., 1997, ApJ, 483, 582

[73] Elvis M., Wilkes B.J., McDowell J.C., Green R.F., Bechtold J., Willner S.P., Oey M.S., Polomski E., Cutri R., 1994, ApJS, 95, 1

[74] Elvis M., 2000, ApJ, 545, 63

[75] El-Zant A., Shlosman I., Hoffman Y., 2001, ApJ, 560, 636

[76] Enßlin T.A. & Kaiser C.R., 2000, A&A, 360, 417

[77] Faber S. M.& Jackson, R. E, 1976, ApJ, 204, 668

[78] Fabian A.C. 1999, MNRAS, 308, L39

[79] Fabian A.C., Iwasawa K., Reynolds C.S., Young A.J., 2000, PASP, 112, 1145

[80] Fan X., Strauss M.A., Schneider D.P., Gunn J.E., Lupton R.H., 1999, AJ, 118, 1

[81] Fan X., White, R.L., Davis M., Becker R.H., Strauss M.A., et al. 2000, AJ, 120, 1167

[82] Fan X., Strauss M.A., Richards G.T., et al. 2001a, AJ, 121, 31

[83] Fan X., Strauss M.A., Schneider D.P., et al. 2001b, AJ, 121, 54

[84] Fan X., Strauss M.A., Schneider D.P., et al., 2003, AJ, 125, 1649

[85] Fan X., Hennawi J.F., Richards G.T., et al., 2004, AJ, 128, 515

[86] Fanaroff B.L., Riley J.M., 1974, MNRAS, 167, 31

[87] Ferrarese L. & Merritt D., 2000, ApJ, 539, L9

[88] Ferrarese L., 2002, ApJ, 578, 90

[89] Filippenko A.V. & Ho L.C., 2003, ApJL, 588, L13

[90] Finn R.A., Impey C.D., Hooper E.J., 2001, ApJ, 557, 578

[91] Fontana A., Pozzetti L., Donnarumma I., Renzini A., Cimatti A., Zamorani G., et al., 2004, A&A, in press, astro-ph/0405055

[92] Forbes D.A. & Ponman T.J. 1999, MNRAS, 309, 623

[93] Frank J., King A., Raine D., 2002, Accretion power in Astrophysics. 3rd ed., Cambridge University Press.

[94] Freudling W., Corbin M.R., Korista K.T., 2003, ApJ, 587, L67

[95] Friaça A.C.S. & Terlevich R.J., 1998, MNRAS, 298, 399

[96] Fukugita M., Ichikawa T., Gunn J.E., Doi M., Shimasaku K., Schneider, D.P., 1996, AJ, 111, 1748

[97] Fukugita M., Hogan C.J., Peebles P.J.E., 1998, ApJ, 503, 518

[98] Gebhardt K., et al. 2000, ApJ, 539, L13

[99] Gebhardt K., Lauer T.R., Kormendy J., et al., 2001, AJ, 122, 2469

[100] George I.M.& Fabian A.C., 1991, MNRAS, 249, 352

[101] Gerhard O., Kronawitter A., Saglia R.P., Bender Ralf., 2001, AJ, 121, 1936

[102] Ghosh P. & Abramowicz M.A., 1997, MNRAS, 292, 887

[103] Giacconi R., Zirm A., Wang J., Rosati P., Nonino M., Tozzi P., et al., 2002, ApJS, 139, 369

[104] Goldschmidt P., Miller L., La Franca F., Cristiani S., 1992, MNRAS, 256, 65p

[105] Goldschmidt P., Kukula M.J., Miller L., Dunlop J.S., 1999, ApJ, 511, 612

[106] Gonzalez A. H. et al., 2000, ApJ, 528, 145

[107] Granato G.L., De Zotti G., Silva L., Bressan A., Danese L., 2004, ApJ, 600, 580

[108] Grazian A., Cristiani S., D'Odorico V., Omizzolo A., Pizzella A., 2000, AJ, 119, 2540

[109] Grazian A., Omizzolo A., Corbally C., Cristiani S., Haehnelt M.G., Vanzella E., 2002, AJ, 124, 2955

[110] Greene J.E., Ho L.C., Barth A.J., 2004, in IAU Symp. 222, /0406047

[111] Gregg M.D., Lacy M., White R.L., Glikman E., Helfand D.J., Becker R.H., Brotherton M.S., 2002, ApJ, 564, 133

[112] Griffith M.R., Wright A.E., Burke B., Ekers R.D., 1995, ApJS, 97, 347

[113] Haehnelt M.G. & Rees M.J., 1993, MNRAS, 263, 168

[114] Haehnelt M.G. & Kauffmann G., 2000, MNRAS, 318, L35

[115] Haiman Z., Ciotti L., Ostriker J.P., 2004, ApJ, 606, 763

[116] Hamann F. & Ferland G., 1999, ARA&A, 37, 487

[117] Häring N. & Rix H.-W., 2004, ApJ, 604, 89

[118] Hasinger G. Altieri B., Arnaud M., Barcons X., Bergeron J., Brunner H., et al., 2001, A&A, 365, 45

[119] Heckman T.M., Lehnert M.D., Strickland D.K., Armus L. 2000, ApJS, 129, 493

[120] Hewett P.C., Foltz C.B., Craig B., Chaffee F.H., 1995, AJ, 109, 1498

[121] Hewett P.C., Foltz C.B., Chaffee F.H., 2001, AJ, 122, 518

[122] Hook I.M., Shaver P. & McMahon R.G., 1998, in The Young Universe: Galaxy Formation and Evolution at Intermediate and High Redshift, ed. S. D'Odorico, A. Fontana, & E. Giallongo (San Francisco: ASP), 17

[123] Hooper E.J., Impey C.D., Foltz C.B., Hewett P.C., 1995, ApJ, 445, 62

[124] Hubeny I., Agol E., Blaes O., Krolik J.H., 2000, ApJ, 533, 710

[125] Hubeny I., Blaes O., Krolik, J.H., Agol, E., 2001, ApJ, 559, 680

[126] Hunt M.P., Steidel C.C., Adelberger K.L., Shapley A.E., 2004, ApJ, 605, 625

[127] Hujeirat A. & Blandford R.D., 2003, in press, astro-ph/0307317

[128] Ichimaru S., 1977, ApJ, 214, 840

[129] Igumenshchev I.V., Abramowicz M.A., Narayan R., 2000, ApJ, 537, L27

[130] Inoue S. & Sasaki S., 2001, ApJ, 562, 618

[131] Irwin M.J., McMahon R.G., Maddox S.J., 1994, Spectrum, 2, 14

[132] Ivezic Z., Menou K., Strauss M., Knapp G.R., Lupton H.R., vanden Berk D.E., Richards G.T., Tremonti C., Weinstein M.A., Anderson S., et al., 2002, AJ, 124, 2364

[133] Ivezic Z., Richards G.T., Hall P.B., Lupton R.H., et al. 2003, published in the Proceedings of "AGN Physics with the SDSS", astro-ph/0310569

[134] Ivison R.J., et al. 2002, MNRAS, 337, 1

[135] Jackson C.A. & Wall J.V., 1999, MNRAS, 304, 160

[136] Jarvis M.J., Rawlings S., 2000, MNRAS, 319, 121

[137] Jarvis M.J., Rawlings S., Willott C.J., Blundell K.M., Eales S., Lacy M., 2001, MNRAS, 327, 907

[138] Jørgensen, I., Franx, M., & Kjærgaard, P. 1996, MNRAS, 280, 167

[139] Junor W., Biretta J.A., Livio M., 1999, Nature, 401, 891

[140] Kashikawa N., et al. 2003, AJ, 125, 53

[141] Kaspi S., Smith P.S., Maoz D., Netzer H., Jannuzi B.T., 1996, ApJ, 471, 75

[142] Kaspi S., Smith P.S., Netzer H., Maoz D., Jannuzi B.T., Giveon U., 2000, ApJ, 533, 631

[143] Katz J.I., 1977, ApJ, 215, 265

[144] Kauffmann G., White S.D.M., Guiderdoni B., 1993, MNRAS 264, 201

[145] Kauffmann G., Guiderdoni B., White S.D.M., 1994, MNRAS, 267, 981

[146] Kauffmann G. 1996, MNRAS, 281, 487

[147] Kauffmann G., Nusser A., Steinmetz M., 1997, MNRAS, 286, 795

[148] Kauffmann G. & Haehnelt M., 2000, MNRAS, 311, 576

[149] Kawakatu N. & Umemura M. 2002, MNRAS, 329, 572

[150] Kawakatu N. Umemura M., Mori M., 2003, ApJ, 583, 85

[151] Kedziora-Chudczer L., Jauncey D. L., Wieringa M. H., Walker M. A., Nicolson G. D., Reynolds J. E., Tzioumis A. K., 1997, ApJ, 490, 9

[152] Kellermann K.I., Sramek R., Schmidt M., Shaffer D.B., Green R, 1989, AJ, 98, 1195

[153] Kennefick J.D. Djorgovski S.G. & de Carvalho, R.R. 1995, AJ, 110, 2553

[154] Kochanek C.S., 2001, in Proceedings of The Dark Universe Meeting at STScI, M. Livio, ed., Cambridge University Press, astroph/0108160

[155] Kodama T., Arimoto N., Barger A. J., Arag'on-Salamanca, A., 1998, AA, 334, 99

[156] Koide S., Shibata K., Kudoh T., 1999, ApJ, 522, 727

[157] Königl A. 1989, ApJ, 342, 208

[158] Kormendy J. & Richstone D., 1995, ARA&A, 33, 581

[159] Kormendy J. & Gebhardt K., 2001, in 20th Texas Symposium on relativistic astrophysics, ed. J.C. Wheeler, & H. Martel (AIP Conf. Proc. 586; Melville: AIP), 363

[160] Kronawitter A., Saglia R.P., Gerhard O., Bender R., 2000, A&AS, 144, 53

[161] Lacy M., Laurent-Muehleisen S.A., Ridgway S.E., Becker R.H., White R.L., 2001, ApJL, 551, L17

[162] La Franca F., Gregorini L., Cristiani S., De Ruiter H., Owen F., 1994, AJ, 108, 1548

[163] Laing R.A., Riley J.M., Longair M.S., 1983, MNRAS, 204, 151

[164] Laor A. & Nezter H., 1989, MNRAS 238, 897

[165] Laor A., 2000, ApJ, 543, L111

[166] Lawrence A., 1987, PASP, 99, 309

[167] Lawrence A., 1991, MNRAS, 252, 586

[168] Lightman A.P. & White T.R., 1988, ApJ, 335, 57

[169] Lipunova G.V., 1999, Astronomy Letters, 25, 508

[170] Livio M., Ogilvie G.I., Pringle J.E., 1999, ApJ, 512, 100

[171] Longair M.S., 1966, MNRAS, 133, 421

[172] Maddox S.J., Efstathiou G., Sutherland W.J., Loveday J., 1990, MNRAS, 243, 692

[173] Magliocchetti M., Maddox S.J., Lahav O., Wall J.V., 1998, MNRAS, 300, 257

[174] Magliocchetti M., Maddox S.J., 2002, MNRAS, 330, 241

[175] Magliocchetti M., Maddox S.J., Jackson C.A., Bland-Hawthorn J., Bridges T., et al., 2002, MNRAS, 333, 100

[176] Magorrian J., Tremaine S., Richstone D., Bender R., Bower G., Dressler A., Faber S. M., Gebhardt K., Green R. Grillmair C., et al. 1998, AJ, 115, 2285

[177] Malkan M.A., 1984, ApJ, 287, 555

[178] Maraschi L. & Rovetti F., 1994, ApJ, 436, 79

[179] Marconi A. & Hunt L. 2003, ApJL, 589, L21

[180] Marconi A., Risaliti G., Gilli R., Hunt L.K., Maiolino R., Salvati M., 2004, MNRAS, 351, 169

[181] Marshall H.L., Tananbaum H., Avni Y., Zamorani G., 1983, ApJ, 269, 35

[182] Marshall H.L., 1987, ApJ, 316, 84

[183] Mcdonald D. & Thorne K.S., 1982, MNRAS, 198, 345

[184] McGilchrist M.M., Baldwin J.E., Riley J.M., Titterington D.J., Waldram E.M., Warner P.J., 1990, MNRAS, 249, 110

[185] Mac Low M. & Ferrara A., 1999, ApJ, 513, 142

[186] McLure R.J. & Dunlop J.S., 2002, NMRAS, 331,795

[187] McMahon R.G., White R.L., Helfand D.J., Becker R.H., 2002, ApJS, 143, 1

[188] Meier D.L., 1982, ApJ, 256, 681

[189] Meier D.L., 1999, ApJ, 522, 753

[190] Menci N., Cavaliere A., Fontana A., Giallongo E., Poli F., 2002, ApJ, 575, 18

[191] Menci N., Cavaliere A., Fontana A., Giallongo E., Poli F., Vittorini V., 2004, ApJ, 604, 12

[192] Merritt D., Ferrarese L., Joseph C.L., 2001, Science, 293, 1116

[193] Mignoli M., Pozzetti L., Comastri A., Brusa M., Ciliegi P., et al., 2004, A&A, 418, 827

[194] Miller L., Peacock J.A., Mead A.R.G., 1990, MNRAS, 244, 207

[195] Miller P., Rawlings S., Saunders R., 1993, MNRAS, 263, 425

[196] Minkowski R., 1962, in IAU Symposium 15, Problems of Extra-Galactic Research, . Ed. G.C. McVittie, 112

[197] Miyaji T., Hasinger G., Schmidt M., 2000, A&A 353, 25

[198] Mo H.J., Mao S., White S.D.M., 1998, MNRAS, 297, 71

[199] Mo H.J., Mao S., White S.D.M., 1999, MNRAS, 304, 175

[200] Mori M., Ferrara A., Madau P., 2002, ApJ, 571, 40

[201] Murray N., Chiang J., Grossman S.A., Voit G.M., 1995, ApJ, 451, 498

[202] Nagamine K., Fukugita M., Cen R., Ostriker J.P., 2001, ApJ, 558, 497

[203] Nagamine K., Cen R., Hernquist L., Ostriker J.P., Springel V., 2004, ApJ, 610, 45

[204] Nakamura O., Fukugita M., Yasuda N., Loveday J., Brinkmann J., et al., 2003, AJ, 125, 1682

[205] Narayan R. & Yi I., 1994, ApJ, 428, L13

[206] Narayan R. & Yi I., 1995, ApJ, 444, 231

[207] Narayan R., Mahadevan R., Quataert E., 1999, In Theory of Black Hole Accretion Disks, page 148

[208] Narayan R., Igumenshchev I.V., Abramowicz M.A., 2000, ApJ, 539, 798

[209] Nath B.B. & Roychowdhury S., 2002, MNRAS, 333, 145

[210] Navarro J.F., Frenk C.S., & White S.D.M. 1997, ApJ, 490, 493

[211] Norman C., Hasinger G., Giacconi R., Gilli R. Kewley L., Nonino M., Rosati P., Szokoly G., Tozzi P. Wang J., et al., 2002, ApJ, 571, 218

[212] Novikov I.D. & Thorne K.S., 1973, InC.de Witt and B.S. de Witt, editors, Black Holes - Les Astres Occlus, page 343. Gordon & Breach, New York

[213] Padovani P. & Urry C.M., 1992, 387, 449

[214] Padovani P., 1993, MNRAS, 263, 461

[215] Pahre M. A., Djorgovski S. G., de Carvalho R. R. 1998, AJ, 116, 1591

[216] Papaloizou J.C.B. & Lin D.N.C., 1995, ARA&A, 33, 505

[217] Peacock J.A., 1985, MNRAS, 217, 601

[218] Peacock J.A. 1999, Cosmological Physics (Cambridge University Press)

[219] Peterson B.M., 1993, PASP, 105, 1084

[220] Poveda A., 1961, ApJ, 134, 910

[221] Press W.H. & Schechter P. 1974, ApJ, 187, 425

[222] Press W.H., Teukolsky S.A., Vetterling W.T., Flannery B.P., 1992, Numerical Recipes, Cambridge Univ. Press, Cambridge

[223] Pringle J.E., 1981, ARA&A, 19, 137

[224] Proga D., Stone J.M., Kallman T.R., 2000, ApJ, 543, 686

[225] Rawlings S. & Saunders R., 1991, Nature, 349, 138

[226] Rees M.J., Phinney E.S., Begelman M.C., Blandford R.D., 1982, Nature, 295, 17

[227] Romano D., Silva L., Matteucci F., Danese L., 2002, MNRAS, 334, 444

[228] Ross R.R., Fabian A.C., Mineshige S., 1992, MNRAS 258, 189

[229] Salpeter E.E., 1964, ApJ, 140, 796

[230] Salucci P., Szuszkiewicz E., Monaco P., Danese L., 1999, MNRAS, 307, 637

[231] Sasaki S. 1994, PASJ, 46, 427

[232] Sandage A., 1965, ApJ, 141, 1560

[233] Sandage A., & Visvanathan N., 1978, ApJ, 225, 742

[234] Schmidt M., 1963, Nature, 197, 1040

[235] Schmidt M., 1968, ApJ, 151, 393

[236] Schmidt M., 1970, ApJ, 162, 371

[237] Schmidt M. & Green R., 1983, ApJ, 269, 352

[238] Schmidt M., Schneider D.P. & Gunn, J.E. 1986, ApJ, 306, 411

[239] Schmidt M., van Gorkom J.H., Schneider D.P., Gunn J.E., 1995, AJ, 109. 473

[240] Schneider D.P., Fan X., Strauss M.A., Gunn J.E., Richards G.T., et al., 2001, AJ, 121, 1232

[241] Scott S.E., Fox, M.J., Dunlop, J.S., et al. 2002, MNRAS, 331, 817

[242] Shakura N.I. & Sunyaev R.A., 1976, MNRAS, 175, 613

[243] Shankar F., Salucci P., Granato G.L., De Zotti G., Danese L., 2004, MNRAS in press, astro-ph/0405585

[244] Shapiro S.L., Lightman A.P., Eardley D.M., 1976, ApJ, 204, 187

[245] Shaver P.A., Wall J.V., Kellermann K.I., Jackson C.A., Hawkins M.R.S., 1996, Nature, 384, 439

[246] Shaver P.A., Windhorst R.A., Madau P., de Bruyn A.G., 1999, A&A, 345, 380

[247] Sheth R.K. & Tormen G., 2002, MNRAS, 329, 61

[248] Sheth R.K. et al., 2003, ApJ, 594, 225

[249] Shimasaku K., 1993, ApJ, 413, 59

[250] Sikora M. & Madejski G., 2000, ApJ, 534, 109

[251] Silk J. & Rees M.J., 1998, A&A, 331, L1

[252] Silva L., Granato G.L., Bressan A., Danese, L. 1998, ApJ, 509, 103

[253] Simpson C., 1998, MNRAS, 297, L39

[254] Sincell M., & Krolik J. H., 1998, ApJ, 496, 737

[255] Smith E.P., Heckman T.M., Bothun G.D., Romanishin W., Balick B., 1986, ApJ, 306, 64

[256] Somerville R.S., Primack J.R., 1999, MNRAS, 310, 1087

[257] Somerville R.S., Lemson G., Sigad Y., Dekel, A., Kauffmann G., White S.D.M., 2001, MNRAS, 320, 289

[258] Somerville R.S., 2004, in Multiwavelength Mapping of Galaxy Formation and Evolution, eds. R. Bender and A. Renzini, astro-ph/0401570

[259] Spergel, D.N., Verde, L., Peiris H.V., Komatsu E., et al., 2003, ApJS, 148, 175

[260] Sramek R.A., & Weedman D.W., 1980, ApJ, 238, 435

[261] Stanford, S.A., Eisenhardt, P. R., & Dickinson, M. 1995, ApJ, 450, 512

[262] Stanford, S.A., Eisenhardt, P. R., & Dickinson, M. 1998, ApJ, 492, 461

[263] Stickel M., Meisenheimer K., Kühr H., 1994, A&AS, 105, 211

[264] Stocke J.T., Morris S.L., Weymann R.J., Foltz C.B., 1992, ApJ, 396, 487

[265] Stone J.M., Pringle J.E., Begelman M.C., 1999, MNRAS, 310, 1002

[266] Sun W.-H., & Malkan M. A., 1989, ApJ 346, 68

[267] Sunyaev R.A. & Titarchuk L.G., 1980, A&A, 86, 121

[268] Sutherland R.S. & Dopita M.A., 1993, ApJS, 88, 253

[269] Szuszkiewicz E., Malkan M.A., Abramowicz M.A., 1996, ApJ, 458, 474

[270] Tavecchio F., et al. 2000, ApJ, 543, 535

[271] Tecza M., Baker A.J., Davies R.I., Genzel R., Lehnert M.D., Eisenhauer F., et al., 2004, ApJ, 605, 109

[272] Terlevich R., Tenorio-Tagle G., Franco J., Melnick J., 1992, MNRAS, 255, 713

[273] Thomas D., Maraston, C., Bender, R. 2002, Ap&SS, 281, 371

[274] Thornton K., Gaudlitz M., Janka H.-T., Steinmetz M., 1998, ApJ, 500, 95

[275] Toomre A., & Toomre J. 1972, ApJ, 178, 623

[276] Tout C.A. & Pringle J.E., 1996, MNRAS, 281, 219

[277] Trager S.C., Faber S.M., Worthey G., González, J.J., 2000a, AJ, 119, 1645

[278] Trager S.C., Faber S.M., Worthey G., González, J.J. 2000b, AJ, 120, 165

[279] Tremaine S., et al. 2002, ApJ, 574, 740

[280] Treu, T., Stiavelli, M., Bertin G., Casertano, C., & Møller, P., 2001, MNRAS, 326, 237

[281] Treu, T., Stiavelli, M., Bertin G., Casertano, C., & Møller, P., 2002, ApJ, 564, L13

[282] Treu T. & Koopmans L. V. E., 2004, ApJ, 611, 739

[283] Tully R.B., & Fisher J.R., 1977, A&A, 54, 661

[284] Ueda Y., Akiyama M., Ohta K., Miyaji T., 2003, ApJ, 598, 886

[285] Umemura M. 2001, ApJ, 560, L29

[286] Urry C.M. & Padovani P., 1995, PASP, 107, 803

[287] van den Bosch F.C., 2002, MNRAS, 331, 98

[288] van der Marel R. P., 2003, in Carnegie Observatories Astrophysics Series, Vol. 1: Coevolution of Black Holes and Galaxies, ed. L.C. Ho (Cambridge Univ. Press), in press, astroph/0302101

[289] van Kampen E. Jimenez J., Peacock J.A., 1999, MNRAS, 310, 43

[290] Vigotti M., Carballo R., Benn C.R., De Zotti G., Fanti R., Gonzalez Serrano J.I., Mack K-H, Holt J., 2003, ApJ, 591, 43

[291] Vignali C., Brandt W.N., Schneider D.P., Anderson S.F., et al., 2003, AJ, 125, 2876

[292] Voges W., Aschenbach B., Boller T., Bräuninger H., Briel U., et al., 1999, AA, 349, 389

[293] Voges W., Henry J.P., Briel U., Bräuninger H., Mullis C.R., Gioia I.M., Huchra J.P., 2001, ApJ, 553, 119

[294] Voit G.M., Weymann R.J., & Korista K.T., 1993, ApJ, 413, 95

[295] Volonteri M., Haardt F., & Madau P. 2002, Ap&SS, 281, 501

[296] Volonteri M., Haardt F., & Madau P. 2003, ApJ, 582, 559

[297] Wada K. & Venkatesan A., 2003, ApJ, 591, 38

[298] Wall J.V. & Peacock J.A., 1985, MNRAS, 216, 173

[299] Wandel A., 1997, ApJ, 490, 131

[300] Wang J.-M., Szuszkiewicz E., Lu F.-J., Zhou Y.-Y., 1999, ApJ, 522, 839

[301] Wardle J.F.C., Homan D.C., Ojha R. Roberts D.H., 1998, Nature, 395, 457

[302] Wardle J.F.C., Homan D.C., In Particles and Fields in Radio Galaxies Conference, ASP Conference Proceedings Vol. 250. Edited by Robert A. Laing and Katherine M. Blundell.

[303] Warren S.J. Hewett P.C. & Osmer P.S., 1991, ApJS, 76, 1

[304] Warren S.J. Hewett P.C. & Osmer P.S., 1994, ApJ, 421, 412

[305] Webster R.L., Francis P.J., Peterson B.A., Drinkwater M.J., Masci F.J., 1995, Nature, 375, 469

[306] Wechsler R.H., Bullock J.S., Primack J.R., Kravtsov A.V., Dekel, A., 2002, ApJ, 568, 52

[307] White S. D. M. & Rees M. J., 1978, MNRAS, 183, 341

[308] White R.L., Becker R.H., Helfand D.J., Gregg M.D., 1997, ApJ, 475, 479

[309] White R.L., Becker R.H., Gregg M.D., Laurent-Muehleisen S.A., Brotherton M.S., et al., 2000, ApJS, 126, 133

[310] Whiting M. T., Webster R. L., Francis, P. J. 2001, MNRAS, 323, 718

[311] Willott C.J., Rawlings S., Blundell K.M., Lacy M., 1998, MNRAS, 300, 625

[312] Willott C.J., Rawlings S., Blundell K.M., Lacy M., 1999, MNRAS, 309, 1017

[313] Willott C.J., Rawlings S., Blundell K.M., Lacy M., 2000, MNRAS, 316, 449

[314] Willott C.J., Rawlings S., Blundell K.M., Lacy M., Eales S.A., 2001, MNRAS, 322, 536

[315] Wilson A.S., Young A.J., Shopbell P.L., 2000, ApJ, 544, L27

[316] Wolf C., Wisotzki L., Borch A., Dye S., Kleinheinrich M., Meisenheimer, K., 2003, A&A, 408, 499

[317] Woo J-H & Urry C.M., 2002, ApJ, 581, L5

[318] Woosley S.E. & Weaver T.A., 1986, ARA&A, 24, 205

[319] Yee H.K.C. & Green R.F., 1987, ApJ, 319, 28

[320] York D., et al. 2000, AJ, 120, 1579

[321] Zhao D.H., Mo H.J., Jing Y.P., Börner G. 2003, MNRAS, 339, 12

[322] Zeldovich Y.B. & Novikov I.D., 1964, Sov. Phys. Dokl., 158, 811

Appendix A

Tables

Table A.1: Optical and radio properties of the FIRST-2dF quasar sample (see Chapter 2)

Name (1)	RA(J2000) (2)	Dec(J2000) (3)	b_J (4)	$u - b_J$ (5)	$b_J - r$ (6)	$S_{1.4}$(mJy) (7)	z (8)	Morf (9)	α_R (10)
J095245.4+000014	09 52 45.4	+00 00 14	19.85	-1.90	0.44	644.02	1.065	d	0.81
J095306.1+012240	09 53 06.1	+01 22 40	19.56	-1.46	0.58	22.98	1.411		
J095427.2-025218	09 54 27.2	-02 52 18	20.11	-0.47	0.15	4.89	1.748		
J095508.3-022021	09 55 08.3	-02 20 21	20.01	-0.68	0.51	137.95	1.356		0.31
J095540.1+004841	09 55 40.1	+00 48 41	19.54	-1.35	0.82	5.95	2.016		
J095546.6+004042	09 55 46.6	+00 40 42	19.26	-0.66	0.31	4.14	1.416		
J095626.8-024317	09 56 26.8	-02 43 17	19.54	-1.39	0.34	21.68	1.977	d	
J095831.9+001231	09 58 31.9	+00 12 31	19.52	-0.58	0.13	1.27	2.313		
J100409.1+005929	10 04 09.1	+00 59 29	20.57	-0.60	-0.09	21.28	1.869		
J100445.4-011918	10 04 45.4	-01 19 18	19.26	-1.61	0.50	50.00	1.344	t	
J101056.1+013518	10 10 56.1	+01 35 18	20.02	-1.22	0.35	12.00	1.038	d	
J101159.1+000043	10 11 59.1	+00 00 43	20.53	-0.86	0.43	6.07	1.675		
J101216.7+005745	10 12 16.7	+00 57 45	19.63	-0.71	0.46	12.90	2.459		
J101722.9+001138	10 17 22.9	+00 11 38	20.41	-0.31	0.25	26.57	2.294		
J101742.3+013216	10 17 42.3	+01 32 16	18.35	-0.82	0.64	6.33	1.457		
J102321.7+015212	10 23 21.7	+01 52 12	20.42	-0.81	0.54	12.98	1.071		
J103348.1-023806	10 33 48.1	-02 38 06	20.42	-0.44	0.50	4.28	1.784		
J103415.1-015340	10 34 15.1	-01 53 40	20.21	-1.11	0.51	7.27	1.855		
J104120.0-023442	10 41 20.0	-02 34 42	20.43	-0.26	-0.05	2.27	2.636		
J105234.2-001501	10 52 34.2	-00 15 01	18.72	-0.47	0.90	1.40	1.162		
J105332.2-002321	10 53 32.2	-00 23 21	20.32	-1.16	1.01	3.21	0.980		
J105336.0+000735	10 53 36.0	+00 07 35	19.45	-0.82	0.56	25.31	2.597		
J105457.0-004554	10 54 57.0	-00 45 54	18.38	-1.25	0.23	613.25	0.916	t	0.96
J105642.7-004256	10 56 42.7	-00 42 56	20.07	-0.50	0.47	6.78	0.759		
J105858.1-014610	10 58 58.1	-01 46 10	19.24	-0.79	0.13	11.06	2.062	d	
J110549.6-014525	11 05 49.6	-01 45 25	19.14	-0.99	1.04	1.03	0.452		
J110811.3+001429	11 08 11.3	+00 14 29	20.04	-0.33	0.40	12.26	1.721		
J111344.7-004412	11 13 44.7	-00 44 12	19.33	-1.12	1.08	8.21	1.487		
J112005.1-015023	11 20 05.1	-01 50 23	20.16	0.30	-0.98	22.02	0.557		
J112635.8-021538	11 26 35.8	-02 15 38	20.35	-0.82	-0.58	166.10	2.133		
J112912.7-010001	11 29 12.7	-01 00 01	20.70	-0.95	0.72	17.63	1.710		
J112917.2-001151	11 29 17.2	-00 11 51	19.93	-0.58	0.79	1.44	1.382		
J112918.9-024123	11 29 18.9	-02 41 23	19.95	-0.55	0.79	24.87	1.008		
J112946.0-012141	11 29 46.0	-01 21 41	18.29	-1.01	0.53	261.75	0.726	t	
J113057.7-015539	11 30 57.7	-01 55 39	19.55	-1.42	0.69	11.77	1.368		
J113144.8-001648	11 31 44.8	-00 16 48	19.01	-0.31	-0.48	21.18	1.759		
J113235.8-012849	11 32 35.8	-01 28 49	18.94	-0.90	0.11	151.63	0.441	t	0.6
J113303.0+001548	11 33 03.0	+00 15 48	18.78	-1.23	0.56	224.21	1.171		0.28
J113331.9-003939	11 33 31.9	-00 39 39	20.78	-0.71	0.28	5.81	0.723		
J113418.3-012254	11 34 18.3	-01 22 54	20.19	-0.83	0.90	1.91	0.745		
J113629.2-015249	11 36 29.2	-01 52 49	19.39	-1.00	0.45	3.80	1.537		
J113714.2-015335	11 37 14.2	-01 53 35	20.21	-0.68	0.07	31.00	1.293	t	
J114111.5-014307	11 41 11.5	-01 43 07	18.56	-0.73	0.82	239.87	1.266	d	1.0
J114120.2+002256	11 41 20.2	+00 22 56	20.29	-0.35	0.15	88.46	2.196		
J114218.7+004403	11 42 18.7	+00 44 03	20.46	-0.80	0.26	65.83	1.672		
J115148.9-014824	11 51 48.9	-01 48 24	20.46	-1.08	-0.37	5.67	1.757		
J115404.1+001418	11 54 04.1	+00 14 18	18.45	-0.40	0.70	1.67	1.574		
J120501.7-003215	12 05 01.7	-00 32 15	19.08	-0.55	0.53	35.17	1.153		
J120506.4+004720	12 05 06.4	+00 47 20	20.49	-0.75	0.79	1.48	0.685		
J120741.6-010637	12 07 41.6	-01 06 37	19.25	-1.21	0.40	112.32	1.006		0.1
J120836.2-020727	12 08 36.2	-02 07 27	18.42	-0.17	-0.04	4.40	1.081		
J120857.1+002259	12 08 57.1	+00 22 59	20.10	-0.93	1.11	12.26	1.726		
J121407.6-014921	12 14 07.6	-01 49 21	19.73	-0.60	0.13	18.20	1.006		
J121444.8-011625	12 14 44.8	-01 16 25	20.06	-0.91	10.83	10.00	1.705	d ?	
J121729.8-004717	12 17 29.8	-00 47 17	20.13	-0.32	0.52	19.47	1.316		
J121928.6-015522	12 19 28.6	-01 55 22	20.01	-1.30	0.77	4.38	1.298		

Table A.1: - *continued*

Name (1)	RA(J2000) (2)	Dec(J2000) (3)	b_J (4)	$u - b_J$ (5)	$b_J - r$ (6)	$S_{1.4}$(mJy) (7)	z (8)	Morf (9)	α_R (10)
J121957.7-012615	12 19 57.7	-01 26 15	19.30	-0.47	0.64	1.70	2.636		
J122045.9-012117	12 20 45.9	-01 21 17	18.99	-0.87	0.60	84.52	1.426	t	
J122130.3-024134	12 21 30.3	-02 41 34	20.07	-0.53	0.35	47.58	1.289	d ?	
J122137.2-002925	12 21 37.2	-00 29 25	20.34	-0.54	-0.11	1.01	1.846		
J122159.6-013349	12 21 59.6	-01 33 49	20.62	-0.40	1.06	2.48	0.716		
J122326.9-003214	12 23 26.9	-00 32 14	19.76	0.17	-0.16	2.41	0.808		
J122523.2-015035	12 25 23.2	-01 50 35	19.37	-1.20	1.16	4.87	2.024		
J122915.9-012616	12 29 15.9	-01 26 16	19.56	-1.24	0.76	63.80	1.573		
J123723.8-004211	12 37 23.8	-00 42 11	19.90	-0.72	0.67	1.04	1.818		
J123753.8+001637	12 37 53.8	+00 16 37	20.47	-0.95	-0.17	41.61	0.861	t	
J123856.1-005932	12 38 56.1	-00 59 32	18.57	-1.01	0.53	14.04	1.849		
J124217.9-023357	12 42 17.9	-02 33 57	20.01	-0.23	0.21	2.10	2.387		
J125243.8+005319	12 52 43.8	+00 53 19	19.22	-1.00	0.49	10.27	1.694		
J125258.7-004236	12 52 58.7	-00 42 36	19.44	-0.85	0.69	1.38	1.373		
J125356.4+002334	12 53 56.4	+00 23 34	20.77	-1.59	2.35	41.03	0.379		
J125756.5-004612	12 57 56.5	-00 46 12	19.07	-0.58	0.37	32.73	1.633		
J130402.1-003929	13 04 02.1	-00 39 29	20.22	-0.93	0.65	25.82	1.878		
J131055.8+000814	13 10 55.8	+00 08 14	19.50	-0.88	0.25	2.24	0.933		
J131930.7+010404	13 19 30.7	+01 04 04	20.52	-0.33	0.16	5.97	2.083		
J132509.7+004934	13 25 09.7	+00 49 34	19.46	-0.31	0.09	26.42	0.829	d	
J132750.4+001157	13 27 50.4	+00 11 57	18.87	-0.41	0.72	24.99	2.500		
J132913.0-003353	13 29 13.0	-00 33 53	19.44	-1.07	0.23	4.21	1.492		
J133031.9-004758	13 30 31.9	-00 47 58	19.88	-0.79	0.70	9.26	0.985		
J133121.8+000249	13 31 21.8	+00 02 49	20.17	1.05	-0.12	93.96	0.866		
J133150.5+004520	13 31 50.5	+00 45 20	19.65	-0.88	0.65	2.84	1.889		
J133636.2-020417	13 36 36.2	-02 04 17	19.28	-0.44	0.34	5.11	2.229		
J133727.1-022346	13 37 27.1	-02 23 46	20.15	-0.64	0.34	23.42	1.529		
J133731.8-011544	13 37 31.8	-01 15 44	19.86	-0.55	0.26	243.45	0.829	d	
J134004.6-013747	13 40 04.6	-01 37 47	19.19	-0.73	12.32	165.56	1.620		-0.6
J134126.5-012228	13 41 26.5	-01 22 28	20.69	-1.00	0.83	18.22	0.326	d	
J134629.2-013921	13 46 29.2	-01 39 21	20.39	-0.28	0.47	10.70	0.572		
J134949.2-011344	13 49 49.2	-01 13 44	19.19	-1.03	0.70	17.13	1.252		
J135053.1-012839	13 50 53.1	-01 28 39	19.45	-0.61	0.34	140.47	1.479		0.56
J135203.5-011713	13 52 03.5	-01 17 13	19.80	-0.28	0.12	7.81	0.839		
J135457.2-003406	13 54 57.2	-00 34 06	18.41	-0.93	0.21	10.79	0.932		
J135931.6+005459	13 59 31.6	+00 54 59	18.78	-1.07	0.37	2.83	0.493		
J135954.6-001752	13 59 54.6	-00 17 52	20.56	-0.19	0.08	1.32	2.518		
J135959.0-014455	13 59 59.0	-01 44 55	20.68	-0.80	-0.72	15.50	2.086	t	
J140010.0+010216	14 00 10.0	+01 02 16	20.64	-1.00	-0.23	7.00	1.672	t	
J140209.0-001522	14 02 09.0	-00 15 22	20.82	-1.28	0.83	1.31	1.883		
J140224.1+003001	14 02 24.1	+00 30 01	19.25	-0.38	1.05	3.00	2.411		
J140412.0-001325	14 04 12.0	-00 13 25	19.05	-0.86	0.40	525.06	1.218		0.1
J140614.8-012938	14 06 14.8	-01 29 38	19.12	-1.37	0.33	1.45	0.551		
J140832.6+003137	14 08 32.6	+00 31 37	19.85	-0.37	-0.09	54.62	1.672	t	
J141041.5-002059	14 10 41.5	-00 20 59	19.99	-1.19	0.67	2.08	1.550		
J141519.8+002329	14 15 19.8	+00 23 29	19.29	-1.13	1.01	2.86	1.266		
J141711.4-023146	14 17 11.4	-02 31 46	20.69	-0.67	0.42	15.76	1.583		
J141942.3-020916	14 19 42.3	-02 09 16	19.88	-0.43	0.69	3.57	0.914		
J142401.5-023505	14 24 01.5	-02 35 05	19.74	-0.15	0.03	9.54	0.842		
J142432.3-014612	14 24 32.3	-01 46 12	19.70	-0.82	0.73	1.35	1.479		
J142509.1-022717	14 25 09.1	-02 27 17	19.19	-1.07	-0.01	49.16	1.680		
J143305.4-013305	14 33 05.4	-01 33 05	20.53	-0.70	10.17	10.06	1.851		
J143410.7-012342	14 34 10.7	-01 23 42	19.07	-0.69	0.48	111.04	1.018	t	
J143945.8-014742	14 39 45.8	-01 47 42	18.94	-0.64	0.09	1.45	0.721		
J144205.8-024803	14 42 05.8	-02 48 03	19.91	-0.53	0.33	2.45	0.320		
J144536.3-011034	14 45 36.3	-01 10 34	19.12	-0.29	0.14	71.15	1.593		
J144538.8-023056	14 45 38.8	-02 30 56	20.76	-0.95	0.60	59.06	1.492	d	

Table A.2: Optical and radio properties of the new FIRST-2dF quasar sample (see Chapter4)

Name (1)	RA(J2000) (2)	Dec(J2000) (3)	b_J (4)	$u - b_J$ (5)	$b_J - r$ (6)	$S_{1.4}$(mJy) (7)	z (8)	Morf (9)	α_R (10)
J100704.3-020711	10 07 04.34	-02 07 10.9	19.728	-1.586	0.518	464.74	1.215		-0.261
J100810.2+015641	10 08 10.22	+01 56 42.3	20.142	-1.417	0.373	46.01	1.597		
J100813.1-021020	10 08 13.12	-02 10 19.8	18.673	-1.359	0.561	117.33	1.180	t	0.416
J101018.2+000350	10 10 18.20	+00 03 51.3	18.456	-0.443	0.600	4.65	1.400		
J101051.6-020020	10 10 51.65	-02 00 19.7	19.277	-0.776	0.609	707.47	0.890	d	-0.125
J101102.8-021619	10 11 02.88	-02 16 19.3	19.254	-0.451	0.715	17.88	1.620	d	
J101358.7+011927	10 13 58.72	+01 19 28.3	19.282	-0.786	0.321	12.55	1.990		
J101629.1-013515	10 16 29.16	-01 35 14.6	20.216	-0.629	0.569	10.24	2.601		
J101651.7-003347	10 16 51.75	-00 33 47.3	18.960	-0.838	0.195	137.60	1.820	t	0.616
J101709.2-011824	10 17 09.25	-01 18 23.7	19.458	-0.447	-0.161	18.41	2.200	t	
J101925.4-000148	10 19 25.48	-00 01 47.6	19.257	-1.277	0.215	4.65	0.840		
J101936.1-004640	10 19 36.17	-00 46 39.0	20.684	-0.710	0.561	6.21	1.448		
J102002.9-024718	10 20 03.02	-02 47 17.0	20.000	-1.534	0.623	6.65	1.447		-1.483
J102023.1-020252	10 20 23.19	-02 02 51.4	19.366	-0.996	0.196	5.26	1.110		
J102135.8-010707	10 21 35.86	-01 07 06.9	19.358	-0.801	0.455	5.85	1.490		
J102150.2-003853	10 21 50.29	-00 38 51.9	19.588	-1.032	0.624	6.76	1.000		
J102224.8+000642	10 22 24.84	+00 06 42.7	19.723	-0.097	-0.072	3.75	0.619		
J102238.5+015443	10 22 38.52	+01 54 43.9	19.983	-0.254	0.420	1.55	2.582		
J102429.5-005256	10 24 29.59	-00 52 55.5	18.724	-0.600	0.255	1032.78	2.560		0.108
J102442.1-021825	10 24 42.13	-02 18 24.0	20.652	-1.012	0.457	13.32	1.759		
J102500.8-004044	10 25 00.82	-00 40 44.2	19.336	-0.520	0.933	4.13	0.634		
J102644.8+004458	10 26 44.80	+00 44 58.7	20.829	-0.170	0.054	1.52	1.882		
J102750.9+002832	10 27 50.97	+00 28 32.9	18.751	-0.341	0.392	8.63	1.140		
J102837.0-010028	10 28 37.02	-01 00 27.4	18.401	-0.979	0.155	156.41	1.530		0.313
J103245.3+014923	10 32 45.36	+01 49 24.4	18.958	-0.410	0.493	16.63	2.410		
J103727.4+003634	10 37 27.45	+00 36 35.4	19.659	-0.400	0.461	27.94	1.500		
J103932.9-012037	10 39 32.97	-01 20 36.0	19.791	-1.168	0.234	7.92	1.880		
J104112.5+004548	10 41 12.53	+00 45 49.3	19.834	-1.148	0.602	309.30	1.220	d	0.789
J104127.1+012656	10 41 27.18	+01 26 57.1	20.405	-1.116	-0.097	2.56	1.620		
J104305.9+001005	10 43 06.00	+00 10 06.5	18.992	-1.013	0.874	1.31	0.934		
J104312.8-001349	10 43 12.84	-00 13 49.1	20.785	-0.792	0.776	186.39	0.817	d	0.823
J104534.9-005530	10 45 34.98	-00 55 29.5	20.621	-0.697	0.954	16.02	0.936	t	
J104726.6+011147	10 47 26.65	+01 11 47.5	20.733	-1.177	1.108	91.90	1.349	d	
J104834.5-013117	10 48 34.54	-01 31 16.1	19.308	-0.587	0.879	1.49	1.693		
J104837.3+011056	10 48 37.32	+01 10 57.5	19.272	-0.508	0.342	2.55	2.318		
J104901.7+005533	10 49 01.71	+00 55 33.8	18.383	-0.825	0.404	5.78	1.164		
J105135.3+005133	10 51 35.33	+00 51 33.5	20.280	-1.146	-0.018	20.63	2.007	t	
J105233.1+013558	10 52 33.16	+01 35 58.9	19.425	-0.340	0.195	191.09	1.910		0.497
J105342.1-001420	10 53 42.23	-00 14 20.3	18.927	-0.399	0.598	44.99	0.676		-0.018
J105352.8-005853	10 53 52.89	-00 58 52.8	18.716	-0.444	0.874	27.36	1.550	t	
J105829.6+013358	10 58 29.62	+01 33 58.7	18.557	-0.552	1.060	3451.81	0.890	t	0.045
J110048.8+015223	11 00 48.82	+01 52 24.1	20.642	-0.737	0.759	1.73	2.091		
J110208.7+014111	11 02 08.73	+01 41 12.1	18.544	-0.723	0.648	10.42	0.397		
J110243.4-002321	11 02 43.40	-00 23 21.0	20.079	-0.839	0.684	49.28	2.491		-0.439
J110440.8-000442	11 04 40.82	-00 04 42.0	19.552	-0.557	0.763	32.70	1.350		
J110514.2+010907	11 05 14.27	+01 09 08.2	19.443	-1.488	0.775	82.31	1.450	t	0.215
J110755.6-024338	11 07 55.68	-02 43 37.3	19.919	0.746	-0.700	26.79	1.700		-0.435
J110836.5+015521	11 08 36.56	+01 55 21.7	19.880	-1.049	0.325	2.48	1.822		
J110903.2-002545	11 09 03.23	-00 25 44.9	19.237	-1.192	0.496	3.19	1.330		
J111114.1+012034	11 11 14.11	+01 20 34.4	18.428	-0.629	0.469	23.07	2.150		
J111138.5+004656	11 11 38.50	+00 46 56.7	19.804	-0.145	0.315	105.27	2.500		0.252
J111214.4+012047	11 12 14.45	+01 20 48.1	19.276	-1.366	0.768	76.60	1.304	t	
J111221.7+003028	11 12 21.80	+00 30 28.6	18.785	-0.902	0.393	9.18	0.523		
J111300.4+013551	11 13 00.50	+01 35 51.8	20.301	-1.409	1.010	23.33	1.475		
J111335.6-020250	11 13 35.66	-02 02 49.5	20.746	-0.502	0.397	62.56	1.450		0.213
J111439.6-024732	11 14 39.66	-02 47 31.8	19.463	-0.805	0.897	194.71	1.040		0.128
J111615.3+011551	11 16 15.43	+01 15 51.7	19.674	-0.107	0.108	3.85	2.290		
J111708.8+004309	11 17 08.86	+00 43 10.6	19.820	-0.552	0.190	82.82	1.120	d	
J111902.0-014529	11 19 02.02	-01 45 28.6	19.849	-1.165	0.603	15.96	1.300		
J112324.7+004531	11 23 24.71	+00 45 31.6	20.286	-0.499	0.419	6.06	1.338		

Table A.2: - *continued*

Name (1)	RA(J2000) (2)	Dec(J2000) (3)	b_J (4)	$u - b_J$ (5)	$b_J - r$ (6)	$S_{1.4}$(mJy) (7)	z (8)	Morf (9)	α_R (10)
J112336.5+012201	11 23 36.57	+01 22 01.5	19.032	-0.915	0.960	2.70	0.938		
J112405.4-003500	11 24 05.46	-00 35 00.1	19.713	-0.983	0.395	113.08	1.950		
J112428.0+011233	11 24 28.08	+01 12 33.8	20.485	-0.847	0.444	11.77	2.016		
J112458.2-022304	11 24 58.22	-02 23 03.4	20.834	-0.223	10.675	15.03	1.512		
J112506.9-001648	11 25 06.95	-00 16 47.9	19.521	-0.170	0.017	65.47	1.750		
J112519.2-010215	11 25 19.21	-01 02 14.9	19.504	-0.905	0.555	3.66	1.110		
J112721.3-021326	11 27 21.36	-02 13 25.3	20.116	-1.135	0.459	171.28	0.944		0.944
J113044.3+013724	11 30 44.30	+01 37 24.6	20.399	-1.771	1.158	26.82	0.888	t	
J113209.6+013212	11 32 09.69	+01 32 13.2	20.511	-1.368	10.525	104.14	1.065		0.750
J113250.8-002001	11 32 50.85	-00 20 00.8	20.431	-0.882	0.779	14.70	2.428		
J113320.0+004052	11 33 20.04	+00 40 52.9	19.980	-1.040	-0.005	322.30	1.640		-0.122
J113349.9-005053	11 33 49.99	-00 50 52.9	20.822	-0.849	10.213	1.00	1.946		
J113437.0+013333	11 34 37.12	+01 33 34.0	19.942	-0.399	0.522	66.61	1.340		
J113513.9-015605	11 35 14.02	-01 56 04.3	20.281	-0.455	0.416	1.30	2.064		
J113550.2-024456	11 35 50.26	-02 44 55.1	20.849	-0.826	1.234	23.77	1.584		
J113559.5+011321	11 35 59.57	+01 13 22.0	20.723	-0.382	0.628	7.06	2.573		
J113703.0+014005	11 37 03.09	+01 40 06.1	20.417	-0.685	-0.257	10.00	1.697	t	
J113723.4-021509	11 37 23.46	-02 15 08.2	20.688	-0.977	0.078	19.98	1.918		
J113746.2-022638	11 37 46.27	-02 26 37.6	19.738	-1.273	0.303	5.19	1.915		
J113929.1+013018	11 39 29.18	+01 30 18.6	19.813	-0.827	0.554	5.98	1.430		
J114001.4+010341	11 40 01.51	+01 03 41.6	19.359	-1.099	0.054	29.13	1.030	d	
J114004.3-010528	11 40 04.36	-01 05 27.6	18.877	-0.539	1.539	9.73	0.343		
J114106.5-014108	11 41 06.59	-01 41 07.5	19.837	-1.066	0.389	3.81	1.270		-2.331
J114201.2-004443	11 42 01.23	-00 44 42.1	19.583	-0.443	0.081	28.52	1.710		
J114510.3+011055	11 45 10.37	+01 10 56.1	19.893	-0.302	-0.028	29.33	0.627	m	
J114534.4-004339	11 45 34.51	-00 43 38.8	19.257	-0.683	0.119	7.43	1.740		
J114554.0-003644	11 45 54.05	-00 36 43.1	20.820	-0.685	1.890	5.52	0.281	d	
J114646.6+015603	11 46 46.72	+01 56 04.1	18.859	-0.672	1.059	16.77	2.640		
J114652.9-012447	11 46 52.96	-01 24 46.3	20.519	-0.310	-0.007	46.15	1.977		
J114818.6-021327	11 48 18.71	-02 13 26.6	18.843	-0.574	0.333	11.89	0.783		
J115045.0-022000	11 50 45.06	-02 20 00.1	19.814	-0.703	0.619	4.62	1.410	d	
J115210.2+002705	11 52 10.25	+00 27 05.5	20.236	-0.809	0.710	1.53	1.304		
J115334.1+014357	11 53 34.12	+01 43 58.7	20.640	-0.552	2.208	2.20	0.734		-2.429
J115449.4+013442	11 54 49.43	+01 34 43.6	18.641	-0.970	0.454	1.25	0.469		
J115851.1-015443	11 58 51.18	-01 54 42.8	19.015	-0.941	0.888	1.08	1.893		
J115923.6+015223	11 59 23.69	+01 52 24.2	19.773	-0.188	11.438	34.53	2.440	d	
J115927.0-021637	11 59 27.02	-02 16 36.7	20.446	-1.012	0.853	26.94	0.943		
J115940.9-012709	11 59 40.97	-01 27 08.3	18.938	-1.234	0.550	73.84	1.210	t	0.237
J120054.2+002234	12 00 54.24	+00 22 34.5	19.767	-0.995	0.956	16.70	1.140		
J120123.2+002827	12 01 23.25	+00 28 28.0	18.764	-1.079	0.724	365.41	1.370		
J120331.0-014112	12 03 31.10	-01 41 11.9	19.035	-1.376	0.910	12.64	1.830		
J120548.4+005343	12 05 48.48	+00 53 43.7	18.959	-0.691	0.351	107.57	0.930		0.269
J121048.2+010957	12 10 48.27	+01 09 57.5	20.727	-1.290	0.549	25.72	1.249		
J121106.0+002510	12 11 06.08	+00 25 10.8	20.128	-1.073	0.246	8.19	1.654		
J121248.7-001659	12 12 48.84	-00 16 58.5	19.163	0.307	-0.714	8.07	1.470	d	
J121459.8-022458	12 14 59.87	-02 24 56.5	19.451	-0.781	0.139	88.30	1.680		
J121557.5-000720	12 15 57.60	-00 07 19.8	19.547	-0.758	0.547	108.89	0.990	d	
J121717.2+004202	12 17 17.29	+00 42 03.6	18.365	-1.504	1.090	9.43	1.067		
J121858.7+015237	12 18 58.76	+01 52 37.9	19.932	0.210	-0.427	13.75	1.590	m	
J121914.9-000521	12 19 14.97	-00 05 20.6	20.162	-0.345	-0.099	2.48	1.625		
J121932.0+005602	12 19 32.11	+00 56 03.1	20.035	-0.688	0.722	46.54	0.833		
J121945.5+004817	12 19 45.60	+00 48 18.3	20.272	0.605	-0.447	1.11	2.333		
J122002.3+013006	12 20 02.33	+01 30 06.8	18.857	-0.516	0.352	3.17	0.554		
J122039.4-025327	12 20 39.50	-02 53 25.4	18.501	-0.458	-0.048	1.01	1.085		
J122400.7+005919	12 24 00.78	+00 59 20.0	19.547	-0.791	0.810	5.67	1.492		
J122523.8+002334	12 25 23.88	+00 23 34.7	19.604	-0.336	0.023	10.40	0.977		
J122735.3+000952	12 27 35.35	+00 09 52.8	18.817	-0.761	0.348	27.41	1.958		
J122757.4-023701	12 27 57.45	-02 36 59.9	19.671	-1.029	0.948	656.56	1.080		0.683
J123055.3-010851	12 30 55.29	-01 08 50.1	18.974	-0.490	0.084	92.13	1.080		-0.408
J123133.6+002914	12 31 33.68	+00 29 14.3	19.310	-0.291	0.305	2.24	2.292		

Table A.2: - *continued*

Name (1)	RA(J2000) (2)	Dec(J2000) (3)	b_J (4)	$u-b_J$ (5)	b_J-r (6)	$S_{1.4}$(mJy) (7)	z (8)	Morf (9)	α_R (10)
J123139.1+010229	12 31 39.11	+01 02 29.6	19.041	-0.383	0.929	8.34	2.880		
J123258.3-023741	12 32 58.36	-02 37 40.4	20.312	-1.054	0.204	5.82	2.173		
J123500.7+012040	12 35 00.76	+01 20 41.7	19.470	-1.248	0.738	6.79	1.960		
J123524.6-022555	12 35 24.62	-02 25 54.2	19.968	-1.075	0.207	1.63	2.003		
J123608.3-023838	12 36 08.38	-02 38 37.3	20.262	-2.078	1.425	34.12	1.412		
J123630.6+000707	12 36 30.68	+00 07 08.6	19.734	-0.404	0.376	3.98	2.304		
J124029.6-001048	12 40 29.67	-00 10 47.5	19.763	-0.628	0.663	13.16	2.030		
J124216.3+004743	12 42 16.38	+00 47 43.7	19.379	-0.771	0.737	45.83	1.230	t	
J124516.0-001900	12 45 16.04	-00 18 59.5	20.555	-1.016	0.866	5.18	1.595		
J124602.5+011318	12 46 02.52	+01 13 18.7	20.180	-0.915	1.182	79.43	0.384		0.357
J125006.8+015803	12 50 06.84	+01 58 04.0	18.560	-1.138	0.509	155.93	0.938		0.087
J125111.0-002704	12 51 11.01	-00 27 03.8	20.617	-0.633	0.613	181.24	0.865		0.325
J125209.6-001554	12 52 09.65	-00 15 53.3	19.264	-0.439	0.714	140.83	0.813	t	0.325
J125309.5+012830	12 53 09.57	+01 28 30.5	19.161	-1.133	0.777	391.56	1.030		0.800
J125311.2+012026	12 53 11.26	+01 20 27.3	20.068	-0.472	1.095	3.72	1.273		
J125345.9-021035	12 53 45.97	-02 10 34.4	20.342	-0.529	1.339	1.66	0.363		
J125353.5+014134	12 53 53.61	+01 41 34.4	19.139	-0.376	0.823	1.09	1.095		
J125402.1-004931	12 54 02.16	-00 49 31.0	19.864	-0.749	1.134	56.58	1.380	d	
J125417.8-014848	12 54 17.92	-01 48 47.2	19.355	-0.249	0.273	99.00	2.440		0.503
J125528.2-005442	12 55 28.30	-00 54 41.8	19.045	-0.783	0.377	143.12	1.010	d	0.520
J125547.1-020813	12 55 47.22	-02 08 12.0	20.618	-0.837	0.693	9.63	1.288		
J125607.8+000207	12 56 07.87	+00 02 07.7	18.389	-0.664	0.298	1.54	0.650		
J125724.5-021249	12 57 24.57	-02 12 48.7	20.784	-0.979	0.132	1.85	1.415		
J125729.7-013240	12 57 29.80	-01 32 39.6	18.536	-0.923	0.600	119.81	1.451	t	0.433
J125737.0-003220	12 57 37.09	-00 32 20.2	19.458	-0.371	0.352	60.76	1.020	t	
J125805.1+014339	12 58 05.26	+01 43 39.3	20.049	-0.850	0.523	3.59	1.042		
J125834.8+003831	12 58 34.92	+00 38 31.9	19.375	-0.577	0.369	67.67	0.730		-0.772
J125901.4-004317	12 59 01.53	-00 43 16.6	19.437	-0.742	0.456	75.36	1.250		0.263
J125907.6-025734	12 59 07.70	-02 57 33.0	20.202	-0.838	0.475	7.54	1.157		
J125915.3+011808	12 59 15.43	+01 18 08.6	19.753	-0.805	0.421	18.25	0.780		
J130028.4-015141	13 00 28.50	-01 51 40.5	20.279	-0.712	0.371	17.47	1.492		
J130059.7+004442	13 00 59.78	+00 44 42.9	18.653	-0.655	0.426	13.61	1.631		
J130106.1-021913	13 01 06.17	-02 19 12.1	20.826	-0.614	0.051	1.29	2.316		
J130148.5-004115	13 01 48.55	-00 41 14.4	19.476	-0.715	11.772	84.62	1.032		0.188
J130208.2-003732	13 02 08.27	-00 37 31.6	18.583	-0.604	0.813	11.93	1.677		
J130210.9-011004	13 02 11.01	-01 10 03.9	19.201	-1.154	0.625	3.11	1.071		
J130328.5-024632	13 03 28.53	-02 46 31.2	19.664	-0.998	0.279	6.51	2.030		
J130332.0+014407	13 03 32.04	+01 44 07.6	19.679	-0.536	0.609	38.13	2.116		
J130443.9+013230	13 04 44.00	+01 32 30.6	20.340	-0.565	0.310	55.40	2.285		
J130609.6-025927	13 06 09.66	-02 59 26.8	19.806	-0.389	0.177	3.86	2.598		
J130822.5+011535	13 08 22.56	+01 15 35.9	19.484	-0.716	1.243	45.47	0.510		
J130835.0-013836	13 08 35.06	-01 38 35.0	19.629	-0.690	1.193	5.79	0.489		
J130840.6+005227	13 08 40.63	+00 52 27.7	19.409	-0.332	0.408	3.40	0.653		
J130942.1-022652	13 09 42.14	-02 26 51.9	19.422	-0.323	0.319	37.10	2.579	d	
J130952.1-013218	13 09 52.10	-01 32 16.8	19.897	-0.909	0.623	1.10	1.849		
J131015.0-010028	13 10 15.03	-01 00 27.4	20.163	-1.331	0.984	82.87	1.286		
J131028.5+004408	13 10 28.50	+00 44 09.1	19.934	-0.804	0.810	218.68	1.597	t	
J131055.5-012725	13 10 55.59	-01 27 24.3	18.683	-0.768	0.598	4.56	0.998		
J131234.5+011409	13 12 34.57	+01 14 09.9	20.398	-0.996	1.239	5.50	2.066		
J131538.7-015846	13 15 38.71	-01 58 46.0	19.264	-1.212	0.692	268.55	1.505	d	
J131600.8-021820	13 16 00.79	-02 18 19.6	20.432	-2.146	1.364	92.14	1.269		0.293
J131648.6+005858	13 16 48.70	+00 58 58.3	20.107	-1.029	0.718	18.82	1.267		
J131730.8-011403	13 17 30.80	-01 14 03.0	18.885	-1.052	0.952	1.77	1.317		
J131758.6-014440	13 17 58.64	-01 44 39.7	20.720	-1.430	0.503	1.62	1.108		
J131905.8-015209	13 19 05.86	-01 52 08.9	19.237	-0.652	0.598	10.18	1.531		
J131938.7-004940	13 19 38.76	-00 49 40.1	18.327	-0.816	1.154	1536.50	0.891		
J132434.4-010437	13 24 34.39	-01 04 37.1	19.467	-0.299	0.367	1.64	2.427		
J132724.8+015514	13 27 24.85	+01 55 13.6	20.848	-1.059	0.775	3.25	1.503		
J132903.4-025421	13 29 03.41	-02 54 22.3	20.528	-0.766	0.315	4.97	2.535		
J133000.0-021203	13 30 00.02	-02 12 03.7	20.552	-0.749	0.512	2.51	2.059		

Table A.2: - *continued*

Name (1)	RA(J2000) (2)	Dec(J2000) (3)	b_J (4)	$u - b_J$ (5)	$b_J - r$ (6)	$S_{1.4}$(mJy) (7)	z (8)	Morf (9)	α_R (10)
J133237.6-021517	13 32 37.69	-02 15 16.9	18.953	-1.007	1.357	1.38	1.343		
J133351.5-001821	13 33 51.62	-00 18 20.8	20.705	-0.563	0.061	13.74	0.726		
J133406.5+003124	13 34 06.56	+00 31 25.1	19.700	-0.733	-1.722	8.02	1.544		
J133409.5-025031	13 34 09.58	-02 50 30.3	18.944	-0.693	0.549	36.00	1.700		
J133411.1-012053	13 34 11.15	-01 20 52.8	19.685	-0.503	0.086	2.74	1.626		
J133553.8-022636	13 35 53.88	-02 26 36.1	19.753	-1.020	0.388	1.67	0.451		
J133651.4+014459	13 36 51.47	+01 44 59.6	19.695	-0.148	-0.438	11.86	1.541		
J133745.8+012357	13 37 45.89	+01 23 58.2	20.169	-0.556	-0.198	9.03	1.783		
J133847.1+015019	13 38 47.18	+01 50 19.7	20.685	-0.887	0.491	2.58	1.557		
J133933.9-001612	13 39 33.92	-00 16 12.3	20.340	-0.992	0.405	143.85	1.818	m	
J134031.3+001507	13 40 31.36	+00 15 07.8	18.509	-0.797	0.118	46.43	1.906		
J134042.9+020306	13 40 42.89	+02 03 07.5	18.530	-0.915	0.613	14.51	1.008	t	
J134340.0+015248	13 43 39.98	+01 52 49.1	19.132	-0.573	0.560	13.12	1.191		
J134636.5+011154	13 46 36.52	+01 11 55.3	20.438	-1.156	1.295	7.91	1.673		
J134637.6-002016	13 46 37.65	-00 20 16.1	19.500	-0.937	0.219	1.12	2.044		
J135351.5+015153	13 53 51.57	+01 51 54.0	18.412	-0.572	-0.283	315.85	1.605		
J135406.7+015444	13 54 06.86	+01 54 44.6	20.576	-1.056	0.291	50.88	1.272		
J135409.9-014151	13 54 09.95	-01 41 50.7	20.662	-1.132	1.186	39.23	0.978	t	
J135415.7-003150	13 54 15.79	-00 31 49.5	18.944	-1.485	0.704	2.70	1.226		
J135527.9+015527	13 55 27.98	+01 55 27.5	19.237	-0.774	0.459	11.43	1.729		
J135541.4+015553	13 55 41.45	+01 55 53.2	20.179	-1.299	0.819	66.24	1.279	d	
J140000.7+015827	14 00 00.84	+01 58 27.7	19.113	-1.115	0.862	9.75	0.863		
J140159.8-024540	14 01 59.87	-02 45 39.7	20.593	-0.256	0.200	6.79	2.203		
J140445.8-013022	14 04 45.88	-01 30 21.8	18.269	-0.386	0.367	478.34	2.514		
J140710.5-004915	14 07 10.57	-00 49 15.1	19.252	-1.208	0.642	14.12	1.508		
J140818.4+001308	14 08 18.41	+00 13 09.1	20.581	-0.733	0.234	118.37	1.238		
J141114.3-013153	14 11 14.32	-01 31 52.3	19.961	-0.255	0.427	18.48	0.978		
J141121.3-025542	14 11 21.40	-02 55 41.6	20.068	0.816	-0.036	29.56	0.780		
J141151.8-010037	14 11 51.82	-01 00 36.8	20.769	-0.529	0.727	6.81	1.574		
J141219.9-013408	14 12 19.97	-01 34 08.4	19.168	-0.844	0.860	24.45	0.991		
J141805.8+010750	14 18 05.89	+01 07 50.6	20.311	-0.810	0.256	6.49	1.700		
J141816.4-002521	14 18 16.41	-00 25 20.9	20.449	-0.329	0.501	3.56	1.806		
J141932.5+003120	14 19 32.59	+00 31 20.3	19.185	-0.736	0.336	60.47	0.735	d	
J141956.9+010652	14 19 56.96	+01 06 52.4	19.403	-0.702	0.647	13.51	1.579		
J142033.2-003234	14 20 33.25	-00 32 33.7	19.206	-0.435	0.607	77.56	2.693	t	
J142055.6-000940	14 20 55.62	-00 09 40.3	19.313	-0.854	-0.027	48.67	2.189		
J142545.9+002242	14 25 45.90	+00 22 42.4	18.630	-0.677	0.410	66.53	0.326		
J142607.3-012355	14 26 07.30	-01 23 55.1	19.762	-1.085	0.804	36.10	1.351		
J142608.3+004044	14 26 08.38	+00 40 44.9	20.290	-0.523	0.400	1.86	1.801		
J142649.6-004718	14 26 49.57	-00 47 18.0	19.929	-1.188	0.092	96.42	1.826		
J142655.1-024920	14 26 55.11	-02 49 20.3	20.288	-0.801	0.720	58.45	2.233		
J142746.8+002844	14 27 46.77	+00 28 44.4	20.000	-1.129	1.159	82.74	1.256	d	
J142758.9-012131	14 27 58.87	-01 21 30.8	19.304	-0.858	0.129	32.68	2.277		
J142816.7-003049	14 28 16.69	-00 30 48.7	19.328	-0.476	0.498	27.10	0.853	d	
J142925.9-015034	14 29 25.89	-01 50 33.8	20.838	-1.026	-9.950	35.47	1.058		
J142948.6-011252	14 29 48.65	-01 12 52.1	20.064	-0.512	1.193	715.54	1.498		
J143009.2-005319	14 30 09.17	-00 53 19.3	18.682	-1.752	0.896	3.45	0.813		
J143113.1-005238	14 31 13.12	-00 52 38.5	19.172	-0.523	0.021	86.71	1.634		
J143625.3-020854	14 36 25.33	-02 08 54.2	20.115	-1.084	0.555	1.38	1.760		
J143806.2-003534	14 38 06.25	-00 35 34.8	19.869	-0.501	0.048	21.15	2.281	d	
J143820.8-023954	14 38 20.92	-02 39 53.1	19.411	-0.299	0.036	322.03	1.546	d	
J144434.7+003305	14 44 34.79	+00 33 05.1	20.095	-1.114	0.961	13.19	2.034		
J144447.5-005036	14 44 47.55	-00 50 35.7	19.105	-0.783	0.365	1.95	1.045		
J144559.5-011318	14 45 59.52	-01 13 17.5	18.327	-0.960	0.497	2.79	1.801		
J144636.9+004657	14 46 36.91	+00 46 56.9	19.670	-0.301	-0.136	78.89	0.729	m	0.434
J144937.6-004123	14 49 37.61	-00 41 23.2	20.006	-1.101	0.622	26.25	1.005		
J145002.4+001629	14 50 02.45	+00 16 29.4	18.740	-1.299	1.243	13.84	0.952		-1.257
J145049.9+000143	14 50 49.91	+00 01 44.0	19.371	-0.974	0.032	10.80	1.968	d	

(1) 2dF name; (2) Right Ascension, RA(J2000) and (3) Declination, Dec(J2000); (4) b_J magnitudes; (5) $(u - b_J)$ and (6) $(b_J - r)$ colours; (7) Radio-flux density (in mJy) at 1.4 GHz; (8) Redshift; (9) Notes on the radio morphological appearance: *d* stands for double source (i.e. presenting the two characteristic lobes); *t* indicates a core+lobes structure and *m* for the cases in which the source is decomposed in more than three sub-structures. This information has been obtained by visual inspection of the images of each radio object from the FIRST atlas; (10) Radio spectral index α_R, whenever available.